Advances in the Understanding of Variably Saturated Fracture Flow

Report to the
Water Research Commission

by

Brendon R. Jones, J. Louis Van Rooy, Matthys A. Dippenaar, Luke B. Brouwers, Jacobus I. Roux, André Joubert and Katlego P. Segole

Engineering and Environmental Geology, Department of Geology, Faculty of Natural and Agricultural Sciences, University of Pretoria

June 2016

Obtainable from
Water Research Commission
Private Bag X03
GEZINA, 0031

orders@wrc.org.za or download from www.wrc.org.za

EXECUTIVE SUMMARY

Background

The intermediate vadose zone is often composed of fractured rock. Unsaturated flow through fractured rock cannot be quantified through commonly applied saturated estimate approaches and needs to be addressed for varying saturation and flow path characteristics.

A number of critical parameters influence flow through rock fractures (e.g. Mehreust & Schmittbuhl, 2001; Berkowitz 2002) with fracture characteristics being the most important variables in the system. The following specific fracture characteristics are listed as critical: orientation, aperture, roughness, infill, connectivity (continuity) and spacing. All these parameters are included in the standard joint line survey data collection process during geotechnical site investigations. The data are applied in rock engineering to model the rock mass with regards to rock mass classification, tunnelling support, dam foundations, rock slope stability analysis, and so forth.

Partially saturated fracture flow and the influence of fracture or discontinuity geometry have subsequently been identified as key research questions by, for instance, Berkowitz (2002) and Neumann (2005). As bulk flow generalizes fluxes on a more regional scale, the research presented here focuses almost exclusively on discrete fractures with the purpose of contributing to the questions as to which geometrical properties govern flow. The cubic law is mostly employed for these purposes and relates the estimated hydraulic conductivity to the cube of the fracture aperture, provided that the fracture is clean, smooth, parallel and completely saturated. The validity of the cubic law, however, is often queried given the difficulty in achieving laminar flow as discontinuities are rarely smooth, parallel and open.

This research also assesses geotechnical centrifuge modelling and the potential application to practical problems associated with variably saturated fracture flow. Additionally, this research seeks to contribute to the correlation between mathematical assumptions, field data and numerical models. A case study is therefore also presented to contribute to some knowledge gaps in the upscaling of site-specific field hydraulic tests for incorporation into regional groundwater models and planning.

This research project aims to quantify the hydraulic parameters pertaining to the intermediate vadose zone relating to fractured rock mass through:

1. Assessing discreet unsaturated fracture flow; and
2. Investigating the possible link between discontinuity descriptors and rock mass permeability.

The implications of better understanding of partially saturated flow through rock mass fracture networks are numerous. Worldwide surface infrastructure is presently extending skywards as

well as to greater depths below surface. The increased need for natural resources also implies deeper mines, larger dewatering cones around mines, dewatering of fractured rock aquifers, increased size and toxicity of waste disposal sites, and deep nuclear waste repositories on land surface and in subsurface excavations.

Prospects of deep hydraulic fracturing (fracking) for shale gas or coal-bed methane raise questions about upward migration of hydrocarbon liquids and gases, potentially rendering groundwater aquifers susceptible to contamination. The quantification of water movement through rock masses also has enormous economic implications. Water inflow into deep mines, building basements, civil engineering tunnels (water and transport), subsurface waste disposal sites (nuclear and other) and large rock caverns (hydro-electric and storage facilities) needs to be quantified to create safe operational conditions. Closer to surface, water seepage into road cuts and through rock can affect stability of surface infrastructure.

State-of-the-science

Typical discontinuity survey data collected in rock mechanical context record parameters for each discontinuity intersecting a line set out along an exposed rock face or surface or core from boreholes. Partial saturation can therefore be accommodated in these descriptors, although pore water pressure is generally calculated for saturated conditions (discontinuity filled with water). The normal effective stress component in both the Mohr-Coulomb and Barton-Choubey empirical equations allows for any value to be used from dry to saturated conditions. However, typically full saturation is assumed to calculate for the lowest effective stress. Groundwater measurements are generally limited to visual assessment, water loss measurements in a single borehole or water pressure measurements (Palmstrom and Stille, 2010)

The cubic law is mostly employed for quantifying flow through a discrete fracture, based on the smooth parallel plate model (e.g. Bear, 1972; Berkowitz, 2002; Gudmundsson et al., 2003; Hoek and Bray, 1977; Indraratna and Ranjith, 2001; Liu et al., 2013; Neuman, 2005; Silberhorn-Hemminger et al., 2005; Singhal and Gupta, 2010; Weiss et al., 2006; Witherspoon et al., 1980). As detailed in Zimmerman and Bodvarsson (1996), the cubic law is derived from the Navier-Stokes equation. The cubic law relates the estimated hydraulic conductivity to the cube of the fracture aperture, provided that the fracture is clean, smooth, parallel and completely saturated. However, the validity of cubic law is discussed by several researchers (Lee and Farmer, 1993), and some examples where the cubic law failed are listed by date:

- 1985 (Raven and Gale): rough natural discontinuities subjected to high normal stresses with abundant contact points due to surface roughness.
- 1985 (Pyrak et al.) and 1986 (Witherspoon): only 30% contact area was achieved at effective stresses of 90 MPa in natural fractures.

- 1992 (Cook) and 2003 (Sisavath et al.): flow through a fracture decreases at a rate exceeding the cube of the mean aperture and a nonlinear relationship exists between mean aperture and normal stress.
- 2001 (Aydin): low flow rates with a wide range of friction affected flow domains.

In order to understand the specific influences of geologic media on variable saturated flow in the subsurface, one needs to directly measure or observe the behaviour of fluids. To achieve this, physical modelling of fluid flow through artificial or natural geologic media, simulated at a smaller laboratory scale provides the best approach. Physical models would allow one to directly measure or observe the influence that different fracture properties will have on the flow of fluid. If the model is proportionately scaled and one is aware of the assumptions made and their implications on the modelling results, then the model may ultimately be regarded as a representative simplification of the real system (Silberhorn-Hemminger et al., 2005). If the model is considered to be representative, then the results will aid greatly to the understanding of fluid flow through geologic media. Small scale physical models offer the user maximum control of the boundary conditions and the tests are more repeatable and less costly than large scale tests (Culligan-Hensely and Savvidou, 1995).

Geotechnical centrifuge modelling has developed into an important physical modelling tool due to its ability to replicate natural stress conditions in a reduced-scale model, allowing for many complex interaction problems to be investigated. Centrifuge modelling is unique in that the most complex numerical models are only mathematical approximations of reality, while physical modelling negates the need for complex constitutive models to be selected. Unlike constitutive models, no assumptions need to be made (or are otherwise well understood) and an actual physical event can be observed at model scale (Jacobsz, 2013).

Materials and methods

Centrifuge models are usually scaled down from a prototype site to benchmark the results obtained from the scaled and accelerated tests. The De Hoop Dam was selected as prototype due to existing seepage along a potentially well-defined discontinuity in the rock mass. Data from the investigation phase, foundation mapping during construction and Lugeon testing prior to and during grouting were available. To find a correlation and/or relationship between discontinuity parameters and Lugeon values, statistical and comparative analyses were conducted.

The grouting as-built sheets were used to locate and identify high and low permeability zones of the different blocks. The geological foundation mapping was used to identify possible significant geological features that may influence the characteristics and permeability of the rock mass. These significant features within the blocks were compared to their specific Lugeon values of the block to determine a possible correlation.

The joint line survey data were grouped into the three discontinuity types, viz. tension joints, fault fractures and stress-relief joints. Average values for each parameter that may influence the permeability of a rock mass were calculated for each discontinuity type. These parameter values were weighted against each other. The same statistical analysis was also conducted for the packer test data, with the low and high permeability blocks weighted against each other for all three discontinuity types. Stereographic projections were used to establish possible correlations between the three discontinuity types, as well as between the high and low permeability blocks.

Due to the good correlation that existed between seepage values, and the presence of a pegmatite vein in block 108 and 110 at De Hoop Dam, Matlab® was used to numerically model this feature. The as-built foundation maps of the exposed rock mass were used to model the pegmatite vein as it contained relatively detailed information on the geometry of the fracture, specifically regarding the strike and dip variations along its length within Block 108 and 110. The hydraulic head was calculated, followed by the flow through the pegmatite feature. These results are then to be compared to recorded seepage values, as measured on site.

Prior to attempting any full-scale field and laboratory testing, and modelling for verification of results, fundamental principles pertaining to variably saturated fracture flow and geotechnical centrifuge modelling were evaluated. Experiments were constructed to investigate the fundamental concept of the cubic law under conditions of variable saturation, both at 1G and under increased gravitational acceleration, in the geotechnical centrifuge. The findings of these tests are expected to provide insight into the validity of the cubic law to unsaturated conditions, as well as assessing the use of geotechnical centrifuge modelling in addressing problems associated with unsaturated fracture flow in rock masses.

An investigation followed, attempting to quantify this seepage through this single feature in the rock mass. The various structural properties of the pegmatite vein were determined from a combination of joint line survey data and surface maps. The available data were subsequently extrapolated such that a 3D model of the pegmatite vein could be obtained. The results obtained were correlated with measured discharge values from two relief wells drilled into Block 108 and 110. The numerically modelled discharges varied significantly over the ranges of hydraulic conductivity assumed; and as such, no clear result can be validated with the measured discharges. However, the most likely assumed hydraulic conductivity yielded discharge results within one order of magnitude to that of the measured discharge.

Present experimental research looked only at the validity of existing fracture flow models for a single fracture due to the lack of valid theory and empirical equations to quantify flow through a rock mass. In literature discontinuity orientation, aperture, roughness, infill, continuity, and spacing are listed as the most critical parameters influencing flow through rock discontinuities without any published correlation including all the above.

Main findings

From the study the conclusion can be reached that it is highly unlikely that only a single discontinuity parameter is responsible for high or low Lugeon values. A more plausible answer is that rather a set of parameters are responsible for high or low Lugeon values. A single discontinuity parameter may have a great impact on the permeability of the rock mass, but will not be solely responsible. However, it has been determined that the pegmatite veins associated with the fault fractures that contribute mostly to the high seepage values in the dam foundation. Most notably, a good correlation exists in block 108 and 110, where high seepage values have been measured, with a prominent pegmatite vein running through the foundation of the dam.

The validity of the cubic law can be questioned from the results on a vertical, smooth, clean, parallel fracture, seeing that:

- Full saturation is not ever truly achieved, regardless of centrifugal acceleration or water supply.
- Flow remains as oscillating rivulets and, occasionally, as localised sheets with substantial air pockets.
- Flow achieved is neither uniform, laminar nor saturated.

Although full saturation was observed in some of the horizontal, smooth, clean, parallel plates test, it appears to be compromised when inflow conditions are intermittent, with partial saturation observed in the models tested at increased gravitational acceleration. Moreover, even if the horizontal fracture is fully saturated, this saturation is lost as the fluid exits at the vertical wall. Here the flow regime is observed as exiting at discrete points of the fracture as non-uniform separate rivulets or droplets.

Conclusions

If fairly basic test such as the conceptual tests presented in this report, aiming to directly mimic the smooth parallel plates model, cannot duplicate the basic assumptions of the cubic law, its use in numerical models should also be queried. While orientation has been listed as a parameter influencing flow through discontinuities, it may have a more critical role in governing flow, over other fracture geometry properties.

Results presented in this report show that similar flow regimes described in literature were observed at both 1G and at increased gravitational acceleration (20G), which proves that the geotechnical centrifuge may indeed be a valid method in answering practical problems associated with variably saturated flow.

The present research has underlined the existing issues with using the cubic law to quantify flow through rock fractures. Until a reasonable estimation of flow through rock fractures of

variable geometry (viz. joint descriptors) can be deduced no correlation will exist between joint parameters and flow.

Important contributions to the understanding of flow through discreet fractures include the following:

- Saturated sheetflow is not likely achieved, especially in non-horizontal fractures, resulting in failure of the cubic law .
- Preferential flow still occupies the vast minority of cross-sectional area in a vertical fracture, even if the water supply implies that it should achieve near-saturation.
- Movement of water through the fractured vadose zone becomes a matter of the continuity principle, whereby water should theoretically be transported downward at significantly higher flow rates given the very low degree of water saturation.
- How we aim to quantify discreet fracture flow, notably at sub-saturation, is implicitly inaccurate as is evident by even this study's aims to qualify rather than quantify this flow regime.
- Even an improved qualitative understanding in sub-saturated fracture flow improves the modelling input where presently we rely on quantitative estimates, which proves to be very inaccurate.

Important knowledge gaps exist which mar applications such as estimation of groundwater recharge (notably in thick fractured vadose zones), contaminant transport through the vadose zone, and controlling of pore water pressures in engineering works. In order to address these applications, it is necessary to understand the empirical and modelling assumptions that clearly do not always mimic natural conditions.

Table of Contents

List of Figures

List of Tables

1. INTRODUCTION

1.1. Rationale

The vadose zone is of fundamental importance in protection of groundwater resources. Lack of understanding unsaturated flow through earth materials compromises hydrological models and resource management through, for instance, inaccurate estimations of travel times of contaminants and recharge.

The intermediate vadose zone is often composed of fractured rock. Unsaturated flow through this fractured rock cannot be quantified through commonly applied saturated estimate approaches and need to be addressed for varying saturation and flow path characteristics. The main issue is the quantification of the link between fracture geometry and its hydraulic connectivity. A question therefore exists on how the improvement of field experimentation and measuring relevant parameters can compensate for uncertainty in fracture locations, properties, connectivity and boundary conditions.

According to Berkowitz (2002), fractured geological formations are important in the contexts of exploitation as water supply reservoirs, contamination from surface waste repositories, petroleum reservoir exploitation, geothermal exploitation and heat sinks, mining and mineralization processes (leaching), geotechnical applications and earthquakes. His review paper addresses primarily saturated and partially saturated domains. He concludes that interpretation of field measurements to estimate power law exponents and fractal dimensions pose certain problems. The rock model needs to incorporate geometrical components such as fracture length, orientation, location, density and aperture as well as connectivity.

Large variations in fracture conductivity are caused by anisotropy of fracture roughness and orientation of the hydraulic gradient relative to wall roughness (Mehreust & Schmittbuhl, 2001).

Flow through single discontinuities/fractures has been exhaustively researched (e.g. Raven et al,, 1988; Moreno, et al., 1988; David, 1993). Questions remaining are the quantification of the non-linear relationship between volumetric flow and hydraulic gradient as a function of anisotropy in fracture wall roughness and how the influence of large-scale and small-scale roughness can be separated (Berkowitz, 2002).

The same unanswered questions and more are relevant for fracture networks with the main issue being the quantification of the connection between geometrical and hydraulic connectivity of fracture networks (Berkowitz, 2002).

The inclusion of fractures in the flow model is presently limited to the evaluation of the existing fracture conditions with regards to the aperture, roughness and mineral infilling. Little

attention has been given to the long-term changes in fracture characteristics and the influence on groundwater flow.

It is clear from the above that a number of critical parameters influence flow through rock fractures and the fracture characteristics are the most important variables in the system. The following specific fracture characteristics are listed as critical: orientation, aperture, roughness, infill, connectivity (continuity) and spacing. All these parameters are included in the standard joint line survey data collection process during geotechnical site investigations. The data are applied in rock engineering to model the rock mass with regards to rock mass classification, tunnelling support, dam foundations, rock slope stability analysis, and so forth.

Unsaturated flow and vadose zone hydrology are well documented in local and international research (e.g. summarised by Dippenaar et al., 2014). As most employed methods pertain to fairly uniform sandy soils, the focus of this report is on the lesser researched aspects pertaining to fractured rock.

Dippenaar and Van Rooy (2015; in print) reviewed current and theoretical field methodologies and models to determine fracture flow characteristics in unsaturated fractured rock media. The general approach is to view fractured systems as either bulk systems where flow occurs through fracture networks with possible contribution from the matrix hydraulic conductivity, or alternatively as discrete fractures governing the flow.

As bulk flow generalizes fluxes on a more regional scale, the research presented here focuses almost exclusively on discrete fractures with the purpose of contributing to the questions as to which geometrical properties govern flow. The cubic law is mostly employed for these purposes and relates the estimated hydraulic conductivity to the cube of the fracture aperture, provided that the fracture is clean, smooth, parallel and completely saturated. The highest estimate of hydraulic conductivity is subsequently represented by the cubic law and the lowest by incorporation of the matrix conductivity and infill conductivity (see Hoek and Bray, 1977). The validity of the cubic law, however, is often queried given the difficulty in achieving laminar flow as discontinuities are rarely smooth, parallel and open.

Partially saturated fracture flow and the influence of fracture or discontinuity geometry and intersections have subsequently been identified as key research questions by for instance Berkowitz (2002) and Neumann (2005).

1.2.   Scope

It is intended that this research will assess geotechnical centrifuge modelling focused around partial saturation in the fractured vadose zone. In order to asses the use of geotechnical centrifuge modelling, the research seeks to highlight the potential implications for using the geotechnical centrifuge in answering practical problems associated with variably saturated flow.

Additionally, contributions to the correlation between mathematical assumptions, field data and numerical models are lacking. A case study is therefore also presented to contribute to some knowledge gaps in the upscaling of site-specific field hydraulic tests for incorporation into regional groundwater models and planning.

This research project aims to quantify the hydraulic parameters pertaining to the intermediate vadose zone relating to fractured rock mass through:

1. Assessing unsaturated fracture flow in fractured rock masses; and
2. Investigating the possible link between discontinuity descriptors and rock mass permeability at the hand of a case study at the De Hoop Dam.

1.3.   Applications

Unsaturated flow through geological media has an extensive area of application, and therefore has a widespread area of implication. However as highlighted, a significant knowledge gap exists in this field of research.

In order to understand the specific influences of geologic media on variable saturated flow in the subsurface, one needs to directly measure or observe the behaviour of fluids. To achieve this, physical modelling of fluid flow through artificial or natural geologic media, simulated at a smaller laboratory scale provides the best approach. Physical models would allow one to directly measure or observe the influence that different fracture properties will have on the flow of fluid.

If the model is proportionately scaled and one is aware of the assumptions made and their implications on the modelling results, then the model may ultimately be regarded as a representative simplification of the real system (Silberhorn-Hemminger *et al.*, 2005). If the model is considered to be representative, then the results will aid greatly to the understanding of fluid flow through geologic media. Small scale physical models offer the user maximum control of the boundary conditions and the tests are more repeatable and less costly than large scale tests (Culligan-Hensely and Savvidou, 1995).

The use of the geotechnical centrifuge applied to unsaturated and fractured systems are, therefore, two important research questions in their own rights.

Geotechnical centrifuge modelling has developed into an important physical modelling tool due to its ability to replicate natural stress conditions in a reduced-scale model, allowing for many complex interaction problems to be investigated. Centrifuge modelling is unique in that the most complex numerical models are only mathematical approximations of reality, while physical modelling negates the need or complex constitutive models to be selected (Jacobs, 2013). Unlike constitutive models, no assumptions need to be made (or are otherwise well understood) and an actual physical event can be observed at model scale (Jacobs, 2013)

Centrifuge modelling of soil behaviour has received much more attention than the modelling of rock masses. Consequently, the available literature that deals with fluid flow through a rock mass is scarce and limited to transport studies and petroleum industry research. A significant objective of this project aims at assessing geotechnical centrifuge modelling focused around partial saturation in the vadose zone. In order to asses the use of geotechnical centrifuge modelling, the research seeks to highlight the potential implications for using the geotechnical centrifuge in answering practical problems associated with variably saturated flow. This alone highlights the extreme novelty of this research.

The implications of better understanding of partially saturated flow through rock mass fracture networks are numerous. Worldwide surface infrastructure is presently extending skywards as well as to deeper depths below surface. The increased need for natural resources also implies deeper mines, larger dewatering cones around mines, dewatering of rock aquifers, increased size and toxicity of waste disposal sites, deep nuclear waste repositories, both on land surface and in subsurface excavations. Prospects of deep hydraulic fracturing (fracking) for shale gas or coal-bed methane raise questions about upward migration of hydrocarbon liquids and gases, potentially rendering groundwater aquifers susceptible to contamination. These anthropogenic activities impact on the hydrosphere and lithosphere and need to be quantified to determine negative impacts and remedial measures.

The quantification of water movement through rock masses also has enormous economic implications. Water inflow into deep mines, building basements, civil engineering tunnels (water and transport), subsurface waste disposal sites (nuclear and other) and large rock caverns (hydro-electric and storage facilities) needs to be quantified to create safe operational conditions.

2. CHARACTERISATION OF FRACTURED ROCK MASSES

2.1. Fundamentals of Discontinuity Surveys in Rock

The terms *discontinuity* and *fracture* are often used interchangeably, although the definition of the prior is mostly applied in a rock mechanical and the latter in a geological and hydrogeological sense. Given that flow occurs through fractures and that discontinuities determine the strength of rock masses, the application of the terms often overlap.

Fracture or discontinuity planes are not always smooth and parallel. As shown in Figure 2-1, *roughness* of fractures comprises large-scale waviness (i_1), as well as small-scale *asperities* (i_2) on the fracture walls that influence strength and stress relationships (Hoek and Bray, 1977; Indraratna and Ranjith, 2001; Look, 2007).

Field descriptions simplify roughness and asperities as shown in Figure 2-2. Typical discontinuity survey data collected in rock mechanical context are shown in Figure 2-3 and Figure 2-4. These parameters are recorded for each discontinuity intersecting a line set out along an exposed rock face or surface. The same parameters can be recorded on an exposed rock outcrop across an area and is then referred to as joint window mapping.

Discontinuity data collection generally depends on accessible, exposed rock outcrops or core from boreholes. The calculation of shear strength and determination of rock classes in rock mass classifications usually incorporate a parameter describing the water condition in the discontinuity (Bieniawski, 1989; Jaeger and Cook, 1979.) These descriptions vary between dry, moist, wet, dripping and flowing.

Partial saturation can therefore be accommodated in these descriptors, although pore water pressure is generally calculated for saturated conditions (i.e. for a discontinuity filled with water). The normal effective stress component in both Mohr-Coulomb and Barton-Choubey empirical equations allow for any value to be used from dry to saturated conditions. However, typically full saturation is assumed to calculate for the lowest effective stress.

Groundwater measurements are generally limited to visual assessment, water loss measurements in a single borehole or water pressure measurements (Palmstrom and Stille, 2010)
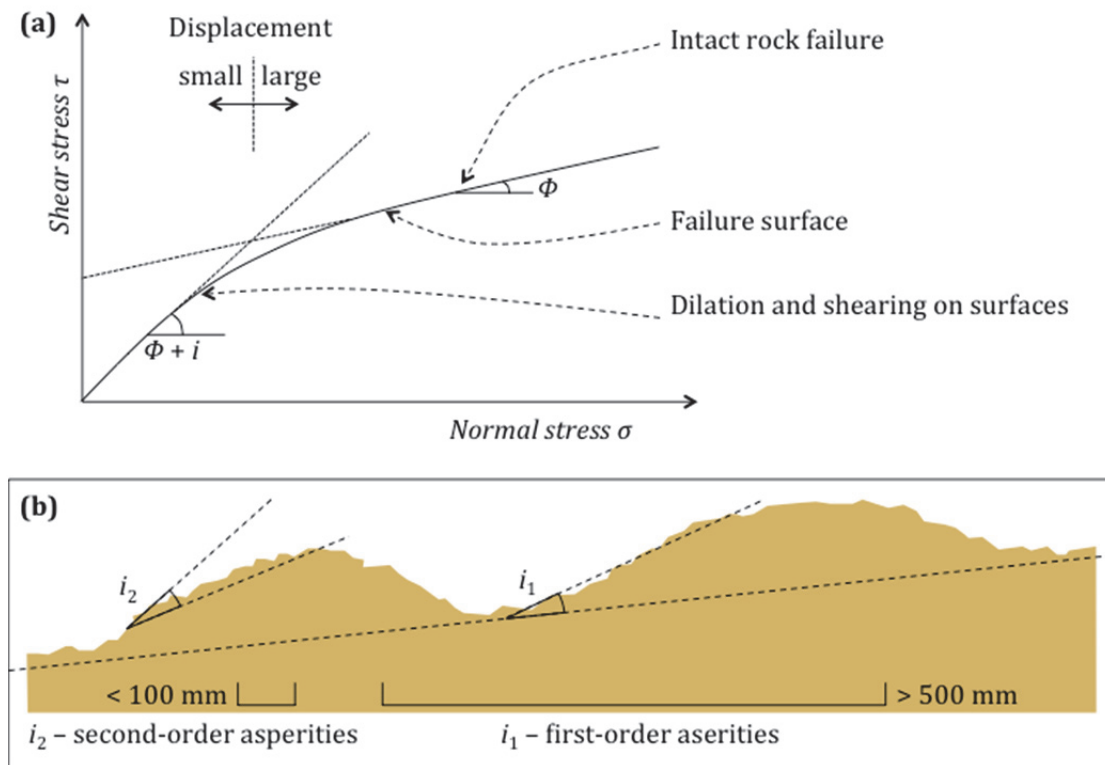
Figure 2-1. (a) Effects of surface roughness *i* on friction Φ and (b) different scales of roughness (e.g. Hoek and Bray, 1977; Indraratna and Ranjith, 2001; Look, 2007).
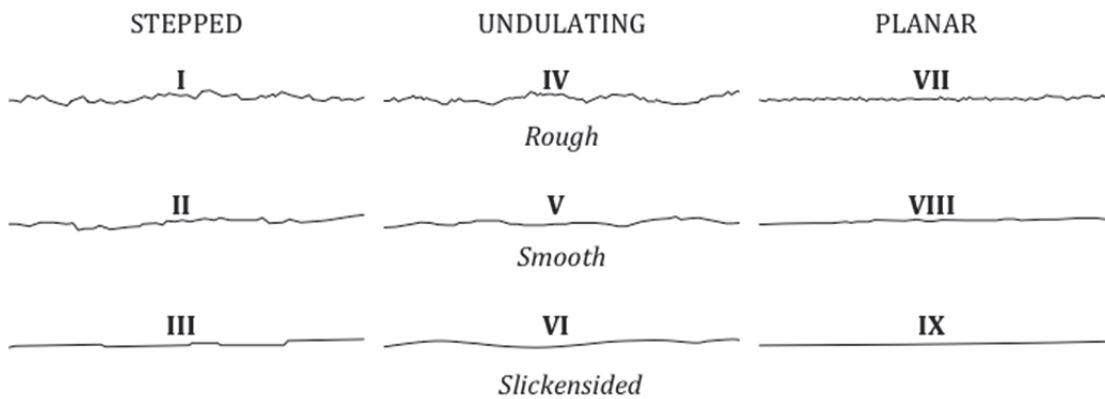
Figure 2-2. Field description of roughness (horizontal scale 10cm) (after ISRM, 1981).

1. TYPE OF STRUCTURE	3. INFILLING – NATURE	4. INFILLING – COMPRESSIVE STRENGTH	5. FRACTURE ROUGHNESS
0 Fault zone	1 Clean	1 Very soft (< 40 kPa)	1 Polished
1 Fault	2 Surface staining	2 Soft (40–80)	2 Slickensided
2 Joint	3 Non-cohesive	3 Firm (80–150)	3 Smooth
3 Cleavage	4 Inactive clay	4 Stiff (150–300)	4 Rough
4 Schistosity	5 Swelling clay	5 Very stiff (300–500)	5 Defined ridges
5 Shear	6 Cemented	6 Hard/ very weak (600–1250)	6 Small steps
6 Fissure	7 Chlorite, talc, gypsum	7 Weak (1.25–5 Mpa)	7 Very rough
7 Tension crack	8 Other – specify	8 Mod. weak (5–12.5)	
8 Foliation		9 Mod. strong (12.5–50)	**7. WATER**
9 Bedding		10 Strong (50–100)	1 Dry

2. APERTURE (mm)			
1 Wide (> 200)		11 Very strong (100–200)	2 Damp
2 Moderately wide (6 200)		12 Ext. strong (> 200)	3 Seepage Flow
3 Moderately narrow (20–60)			4 < 10 ml/s
4 Narrow (6–20)		**6. WAVINESS**	5 10–100 ml/s
5 Very narrow (2–6)		1 Wavelength (m)	6 0.1–1 l/s
6 Extremely narrow (< 2)		2 Amplitude (m)	7 10–100 l/s
7 Tight			8 > 100 l/s

Figure 2-3.   **Descriptors for discontinuity surveys (after Anon, 1977).**
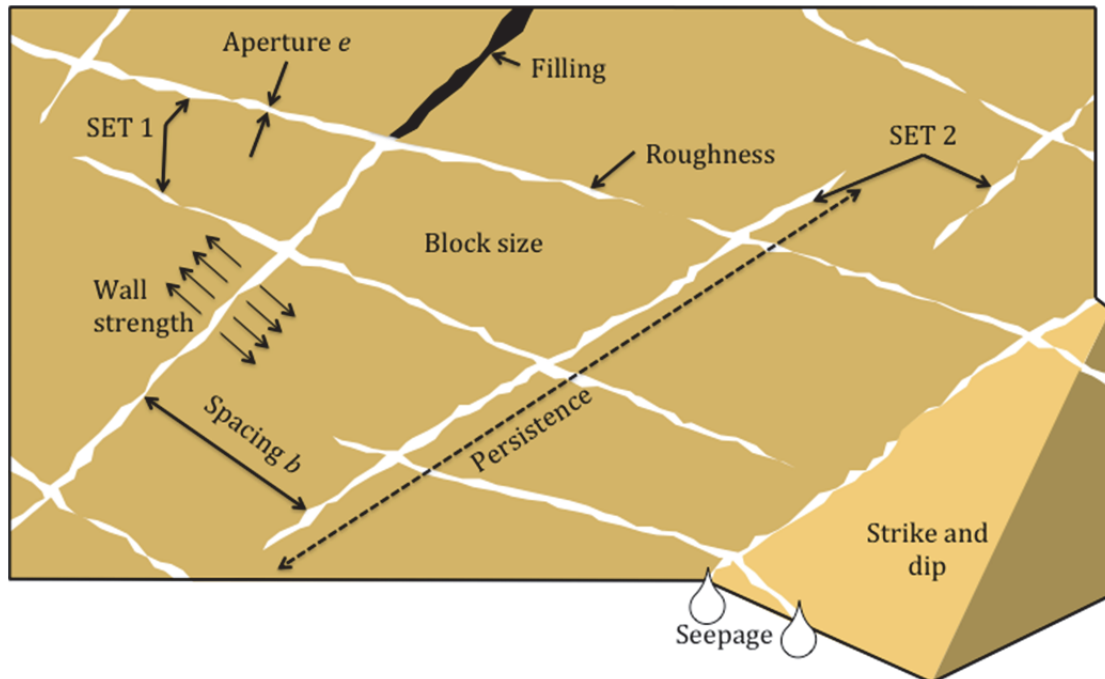
Figure 2-4.   **Geometric properties of discontinuities to be recorded (after Hudson, 1989 in González de Vallejo and Ferrer, 2011).**

2.2.   Fracture Flow

2.2.1.   Aperture versus hydraulic conductivity

In a rock mechanical context, *aperture* (*e*) is broadly defined as the distance between two discontinuity distances normal to those surfaces. However, from a hydrogeological point of view, it is often unclear whether this implies open, infilled, or natural joint conditions. For the sake of this report, the definitions as stated in Figure 2-5 and Table 2-1 are used, where:

- e_f is the fracture aperture;
- e_{if} is the infill aperture;
- e_h is the fracture aperture;
- K_m is the matrix hydraulic conductivity;
- K_f is the fracture hydraulic conductivity;
- K_{if} is the infill hydraulic conductivity; and
- K_h is the effective hydraulic conductivity.

These definitions are thereby related as follows:

- $e_f = e_{if} > e_h$
- $K_f > K_h > K_{if}$

Figure 2-5 is not a conceptual model but rather an adaptation of a natural fracture to that visualised in the smooth parallel plate model. Figure 2-5a illustrates the hydraulic conductivity contributed by a completely open fracture (K_f) with a specific fracture aperture (e_f).

Figure 2-5b shows how the hydraulic conductivity of the fracture is controlled only by the low permeability infill material (K_{if}), even though the infill aperture (e_{if}) is equal to the fracture aperture (e_f). In this specific instance the fracture is completely infilled with low-permeability or impermeable material, such as precipitates or clays, which is contained by the fracture walls.

Figure 2-5c illustrates how open spaces within the distance between the fracture walls and the infill is defined as the effective/hydraulic aperture (K_h), characterised by partially infilled fractures. The infill can be composed of materials, which includes clay, sand and gravel (or a mixture). These materials will each contribute differently to the hydraulic conductivity of the fracture. As shown in Figure 2-5c the preferential flow path for the within the fracture could be open spaces between a partially clay (or precipitate) infilled fracture or within the large pore spaces of granular infill.

NATURAL FRACTURE

SMOOTH PARALLEL PLATE MODEL

(a) e_f Fracture $K_f \gg$

(b) e_{if} Infill $K_{if} \ll$

(c) e_h Effective/ Hydraulic $K_f > K_h > K_{if}$

Rock material

Air-filled fracture

Clays or precipitates

Granular infill
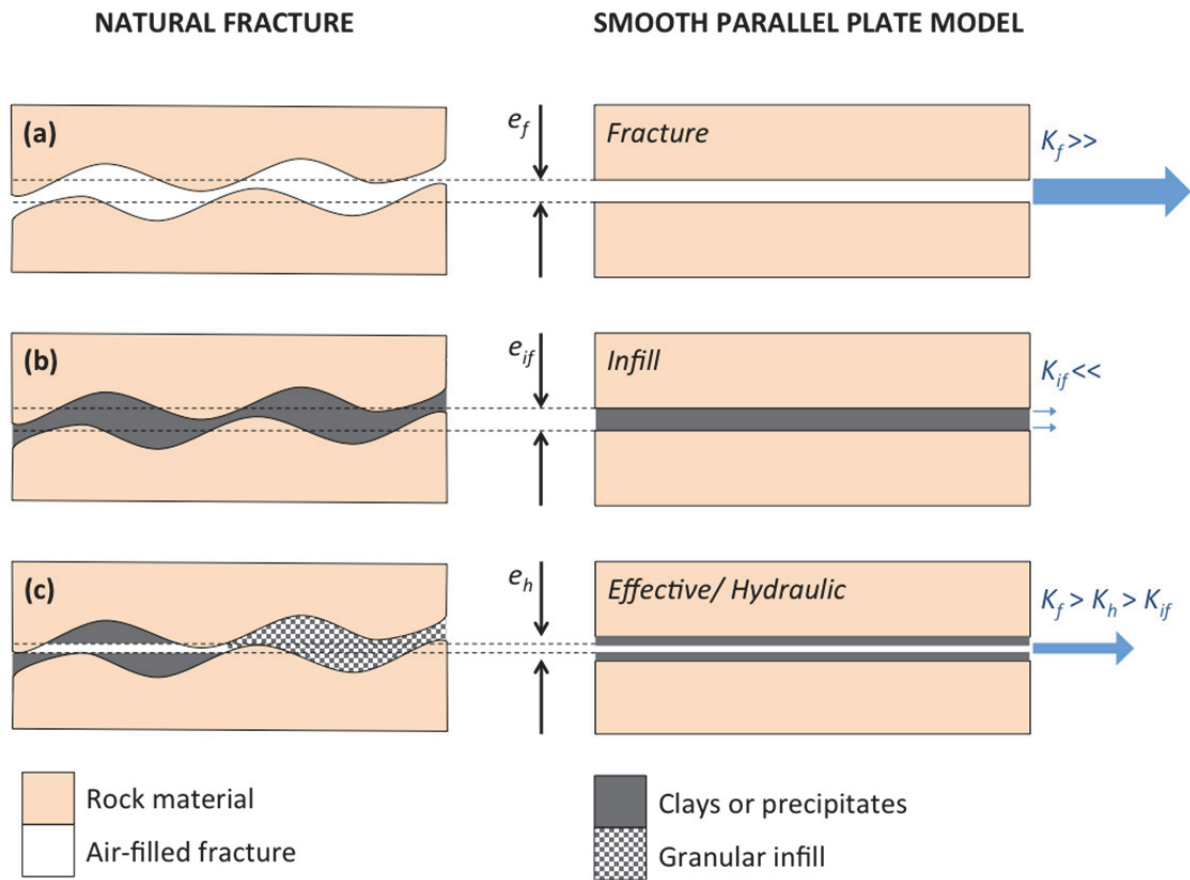
Figure 2-5. **Schematic illustrating the definition of terminology by relating a natural fracture condition to the equivalent smooth parallel plate model.**

Table 2-1. **Definition of terminology pertaining to aperture and hydraulic conductivity of fractures in rock masses.**

	Aperture	Conductivity
Matrix *	n/a	The matrix hydraulic conductivity (K_m) relates to the interstitial porosity of the intact rock material.
Fracture *	The fracture aperture is the average (smoothed) distance, normal to the discontinuity planes, whether open or infilled. (e_f).	The fracture hydraulic conductivity (K_f) relates to the secondary (fractured) porosity of the rock mass; i.e. of open non-infilled discontinuities.
Infill *	The infill aperture is the thickness of the infill in the discontinuity (e_{if}).	The infill hydraulic conductivity (K_{if}) relates to the secondary (fractured) porosity of the rock mass; i.e. of infilled discontinuities.
Effective */ hydraulic *	The hydraulic aperture refers to that distance, normal to the discontinuity planes, which are open and can contribute to the storage and movement of water, as required for use in the cubic law (e_h).	The effective hydraulic conductivity (K_h) of the open portion of the fracture, as required for use in the cubic law.

2.2.2. Cubic law

Literature is abundant on the topics of the smooth parallel plate model and the associated cubic law (e.g. Bear, 1972; Berkowitz, 2002; Gudmundsson et al., 2003; Hoek and Bray, 1977; Indraratna and Ranjith, 2001; Liu et al., 2013; Neuman, 2005; Silberhorn-Hemminger et al., 2005; Singhal and Gupta, 2010; Weiss et al., 2006; Witherspoon et al., 1980). As detailed in Zimmerman and Bodvarsson (1996), the cubic law is derived from the Navier-Stokes equation.

Singhal and Gupta (2010) summarise the derivation of the cubic law, firstly by stating that Darcy's law for flow in a single fracture can be written as Eq. 2.1.

$$V = K_f I$$

Equation 2-1

Where K_f is the hydraulic conductivity of the fracture, defined by Eq. 2.2.

$$K_f = \frac{\gamma_w a^2}{12\mu}$$

Equation 2-2

Where a is the fracture aperture, γ_w is the unit weight of water, and μ is the viscosity of water. As the hydraulic conductivity (K) and permeability (k) are related by Eq. 2.3.

$$K_f = \frac{\gamma}{\mu} k$$

Equation 2-3

Therefore, the permeability of the fracture, k_f, can be defined according to Eq. 2.4.

$$k_f = \frac{a^2}{12}$$

Equation 2-4

By combining Eq. 2.1 and Eq. 2.2, the average velocity $\bar{V}_a$ in the fracture expressed by a single parallel plate model is given by Eq. 2.5.

$$\bar{V}_a = \frac{\gamma a^2}{12a} \frac{dh}{dl}$$

Equation 2-5

Here it is assumed that the fracture walls are impermeable.

Based on Eq. 2.5, Novakowski et al. (2007) computed groundwater velocities over a range of hydraulic gradients and is presented in Figure 2-6.
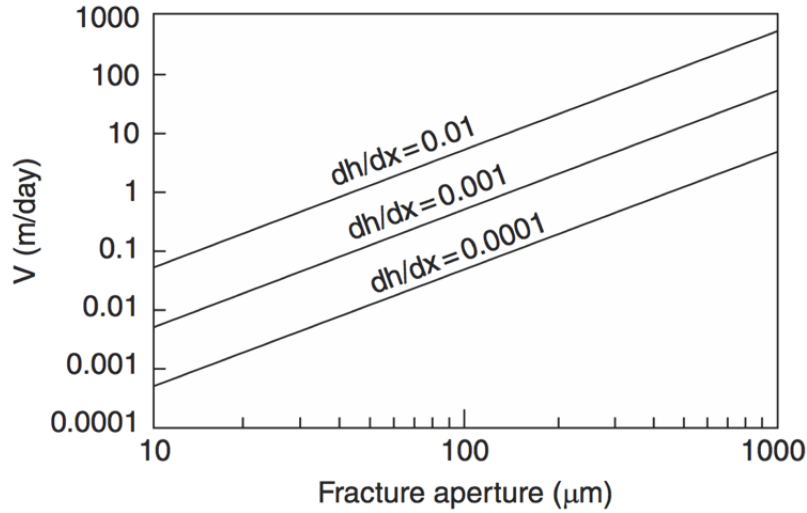
Figure 2-6. **Groundwater velocities in a single fracture as predicted by the cubic law (after Novakowski et al., 2007 in Singal and Gupta, 2010).**

In terms of transmissivity of the fracture, T_f, Eq. 2.4 can be written as Eq. 2.6.

$$T_f = \frac{\gamma}{u} \frac{a^3}{12} = K_f a \qquad \text{Equation 2-6}$$

Many researchers also define T_f as the hydraulic conductivity of the fracture (Bear, 1993 in Singal and Gupta, 2010).

The volumetric flow rate (Q_f) per unit plate (fracture) width will be as per Eq. 2.7.

$$Q_f = \left(\frac{\gamma a^3}{12u}\right) I \qquad \text{Equation 2-7}$$

Eq. 2.7 is referred as the cubic law which is valid for laminar flow through parallel wall fractures with smooth surfaces, and relates the estimated hydraulic conductivity to the cube of the fracture aperture. Singhal and Gupta (2010) importantly state that these assumptions usually do not hold good in natural conditions. Furthermore, it is also difficult to define the representative distance between the fracture walls under field conditions.

The validity of cubic law is discussed by several researchers (Lee and Farmer, 1993), and some examples where the cubic law failed are listed by date:

- 1985 (Raven and Gale): rough natural discontinuities subjected to high normal stresses with abundant contact points due to surface roughness.
- 1985 (Pyrak et al.) and 1986 (Witherspoon): only 30% contact area was achieved at effective stresses of 90 MPa in natural fractures.

- 1992 (Cook) and 2003 (Sisavath et al.): flow through a fracture decreases at a rate exceeding the cube of the mean aperture and a nonlinear relationship exists between mean aperture and normal stress.
- 2001 (Aydin): low flow rates with a wide range of friction affected flow domains.

2.2.3. *Flow regimes in partially saturated fractures*

Flow regimes in open fractures differ from those anticipated in soils. Depending on the aperture, continuity, roughness and other factors, air–water flow in discontinuities is governed by the wetting behaviour of water as well as the water saturation. Different classifications exist for such flow phases, although single vertical fractures with relatively low water saturation are mostly considered systems where water will flow as droplets or films, either as laminar or turbulent flow, on the discontinuity surfaces.

Typical flow mechanisms are shown in Figure 2-7, although the possibility of different mechanisms (e.g. drop flow on fracture walls of vertical fractures at low water saturation) and influences of discontinuity intersections (e.g. larger pore spaces) and orientations (e.g. vertical versus horizontal) should also be considered.
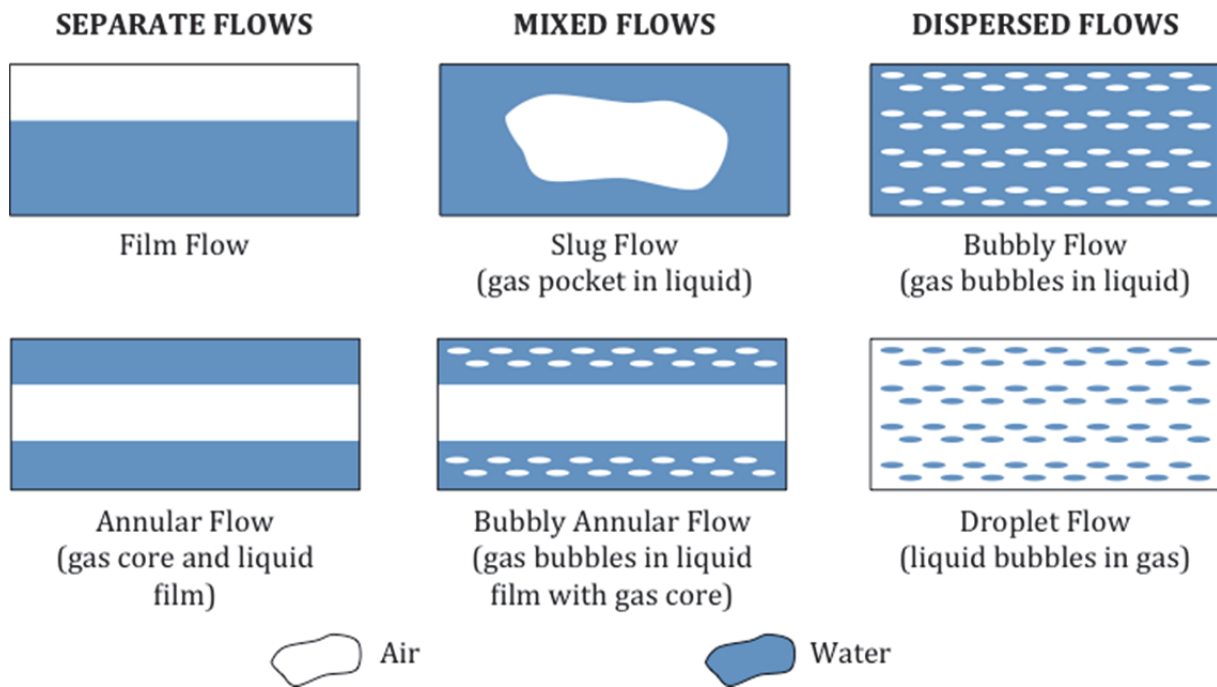
Figure 2-7.   **Flow mechanisms of water–air systems through single fractures or macropores (after Indraratna and Ranjith, 2001; Dippenaar et al., 2014).**

3.   GEOTECHNICAL CENTRIFUGE MODELLING

Geotechnical centrifuge modelling entails the acceleration of a model representing natural conditions to a number of times more than Earth's gravitational field, which correlates to the vertical downscaling of the actual conditions (such as geometry and stresses), as well as accelerating processes such a flow. Centrifuge modelling of soil behaviour has received much more attention than the modelling of rock masses. Consequently, the available literature that deals with fluid flow through a rock mass is scarce and limited to transport studies and petroleum industry research. However, the flow of water through soil centrifuge models has been well studied and has provided a solid platform from which to derive the basic scaling laws for flow in a centrifuge.

A geotechnical centrifuge model is a form of physical modelling and is generally designed to replicate processes that occur in a prototype (Taylor, 1995). Particularly, processes that are affected by gravitational forces are enhanced in geotechnical centrifuge models, with the fundamental requirement for the model and prototype to be similar is that the dimensionless groups are identical (Phillips, 1995; Butterfield, 2000). Before results from models may be extrapolated to prototype scales, similitude must be achieved, which occurs when three types of similarities are satisfied (Kumar, 2007):

1.   Geometric similarity is satisfied when there is a constant ratio of lengths in the model and prototype

2.   Kinematic similarity is satisfied when the ratios of velocities and acceleration between the model and the prototype are constant.

3.   Dynamic similarity is achieved when there is a constant ratio of forces between the model and prototype, where the force may be due to self-weight, viscosity or pressure.

Often the geometric scale factor is selected to fit a prototype situation that causes the least amount of boundary effects in the model (Phillips, 1995). This scaling factor is constrained by the maximum model size, but often this scale factor is made as small as possible and the acceleration level in the centrifuge is normally identical to the geometric scaling factor.

3.1.   Basic Scaling Laws

The fundamental scaling laws of geotechnical centrifuge modelling have been based on the stress-strain properties of soil, which are highly non-linear resulting in soil behaviour being a function of in situ stress levels and stress history (Taylor, 1995; Jacobsz, 2013). Therefore, to ensure accurate strain measurements and process mechanics, it is necessary to replicate the correct stress distribution of prototype situations in the model.

The basic geotechnical centrifuge apparatus spins a model around a fixed axis of rotation at an angular velocity, which increases self-weight of the model by increasing the centripetal acceleration (Taylor, 1995). This centripetal acceleration induces an artificial gravitational acceleration that, with respect to the model, represents a gravitational acceleration that is scaled N times stronger than Earth's gravity. This scaled gravitational acceleration achieves similitude stress distributions between the model and the prototype with the stress distribution for the model and prototype shown in Figure 3-1.
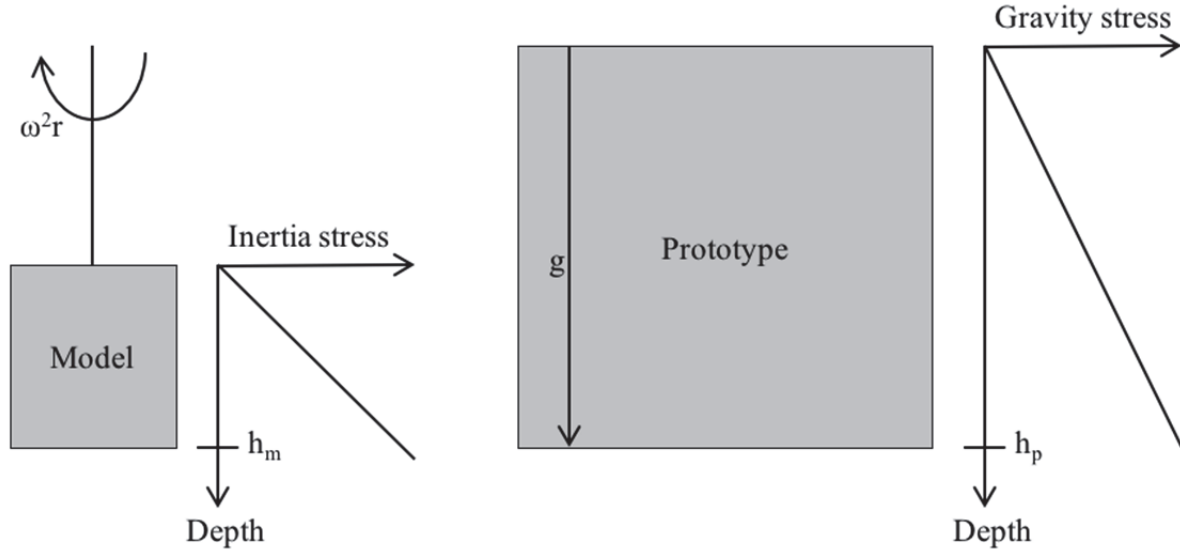
Figure 3-1.   **Inertial stresses in a centrifuge model induced by rotation about a fixed axis correspond to gravitational stresses in the corresponding prototype (after Taylor, 1995).**

3.2.   Linear Dimensions

The basic scaling law requires that there is similitude between the stress levels in the model and the prototype. To determine the stress level in the prototype, Eq. 3.1 can be used, with the subscript p denoting prototype and subscript m denoting model.

$$\sigma_{vp} = \rho g h_p \qquad \text{Equation 3-1}$$

Here the term σ_v is the vertical stress in the profile, ρ is the density, g is the gravitational acceleration and h is the depth. Similarly, the stress in the model can be calculated using Eq. 3.2 where the gravitational acceleration is scaled by a factor of N.

$$\sigma_{vm} = \rho N g h_m \qquad \text{Equation 3-2}$$

Therefore, by using the same prototype soil material in the model, making the density constant, for $\sigma_{vp} = \sigma_{vm}$, then $h_p = h_m N$. This shows that the scale factor for linear dimensions is 1:N for model to prototype (Taylor, 1995). From this it follows that displacement, being a linear dimension, also has a scale factor of 1:N and strains (ε) have a scale factor of 1:1 (Eq. 3.3).

$$\varepsilon = \ \Delta l/l = \ \frac{\Delta l_p}{N\Delta l_m} \ / \ \frac{l_p}{Nl_m} \ = \mathbf{1:1}$$

<div align="right">Equation 3-3</div>

3.3.   Scaling of Seepage

For all scaling factors regarding seepage flow in a geotechnical centrifuge, it is assumed that the soil is fully saturated and these scaling factors are derived from using one-dimensional expressions (Culligan-Hensley & Savvidou, 1995). However, it has been considered that scaling factors are also valid for multi-dimensional problems and unsaturated conditions, but when the model is in fully saturated condition, the flow of the liquid does not depend on surface tension, but only depends on gravitational force, viscosity and average grain size (Laut, 1975).

3.3.1.   Darcy's Law

The rate of seepage flow in a geotechnical centrifuge is determined through Darcy's Law and is increased by a scaling factor of N. However, there is currently some controversy behind how the scaling factor is determined with the debate focusing on two main factors (Taylor, 1995). These factors are the interpretation of the hydraulic gradient and permeability used in Darcy's equation.

If the same fluid is used in the model and prototype, then the permeability is apparently a function of gravitational acceleration and scales as $k_m = \ Nk_p$, while the hydraulic gradient does not scale as it is a dimensionless ratio and therefore $i_m = \ i_p$. Therefore, from Eq. 3.4, which relates the seepage velocity (v) between the model and prototype, it can be seen that the seepage velocity in the model occurs N times faster then the prototype seepage velocity and supplying a scaling factor of 1:N.

$$v_m = \ i_m k_m = \ i_p N k_p = \ N v_p$$

<div align="right">Equation 3-4</div>

This implies a worrying situation where soils are impermeable under a zero gravity field. This implication assumes that seepage is gravity driven and therefore at zero gravity there would be no driving force to induce seepage flow. With this in mind, it is more realistic to think of hydraulic gradient as a pressure gradient. By treating the permeability as a constant material property such that $k_m = \ k_p$. Then, since the stresses are the same, while distances reduced by a scaling factor of N times between the prototype and model, implies a scaling factor of $i_m = \ Ni_p$ for the hydraulic gradient. Substituting this assumption into seepage velocity, as shown in Eq. 3.5, provides the same scaling factor as in Eq. 2.4.

$$v_m = \ i_m k_m = \ Ni_p k_p = \ N v_p$$

<div align="right">Equation 3-5</div>

A study conducted by Thusyanthan and Madathusi (2003) evaluated this conundrum and proposed that Darcy's law is equivalent to Navier-Stokes equations and that the flow is not gravity driven but rather pressure driven. They proposed that Eq. 3.6 should be used to calculate seepage velocity.

$$\boldsymbol{v = \frac{k}{\mu} \times \frac{\Delta[p+zpg]}{\Delta L}}$$ **Equation 3-6**

In this equation, the $\Delta[p + zpg]$ term represents the pressure difference that drives flow in Darcy's law.

3.3.2. Reynolds Number

Darcy's law is only valid at low Reynolds numbers where flow is laminar (Culligan-Hensley and Savvidou, 1995). In order to obtain strict similitude between the prototype and the model, the fluid motion in the model must equal the fluid motion in the prototype and is only satisfied when $R_{em} = R_{ep}$ (Culligan-Hensley and Savvidou, 1995). Since seepage flow velocities in the geotechnical centrifuge are scaled by a factor of 1:N, Reynolds number is scaled by a factor N as shown in Eq. 3.7 to ensure strict similitude.

$$\boldsymbol{R_{em} = NR_{ep}}$$ **Equation 3-7**

However, even if $R_{em} \neq R_{ep}$, there can still be similarity of fluid motion in the model and prototype provided the same manner of flow occurs in both cases. It is therefore always necessary to confirm that laminar flow conditions are present to ensure that Darcy's law is valid and can be suitably modelled in the test (Culligan-Hensley & Savvidou, 1995).

3.3.3. Time

When performing seepage flow scenarios in a geotechnical centrifuge, another parameter that is scaled is time (Taylor, 1995). Since the scaling factor for seepage velocity is 1:N and the scaling factor for the flow paths is 1:N, since it may be considered as linear dimension, the time scaling factor for seepage flow can be derived as shown in Eq. 3.8, providing a scaling factor of 1:N2.

$$\boldsymbol{t_m = \frac{L_m}{vm} = \left(\frac{L_p}{N}\right)\left(\frac{1}{Nv_p}\right) = \frac{1}{N^2}t_p}$$ **Equation 3-8**

It is possible that if soils in the model and prototype have different permeabilities that this effect can be taken into account as shown in Eq. 3.9 (Taylor, 1995).

$$\boldsymbol{t_m = \frac{1}{N^2}\frac{K_p}{K_m}t_p}$$ **Equation 3-9**

4. IN-SITU (FIELD) VALIDATION

4.1. Hydraulic Conductivity and Discontinuity Survey Data

A relationship between hydraulic conductivity and fracture properties was investigated by Hamm et al. (2007) within fractured granite of Mt. Geumjeong area, Korea. Hydraulic conductivity is closely related to the fracture characteristics like orientation, spacing, persistence, wall strength, roughness, filling and interconnectivity.

The hydraulic conductivity of six boreholes using Lugeon tests was related to the fracture spacing, orientation and aperture using borehole data. The discontinuity spacing data was obtained through geophysical surveys (acoustic televiewer) and core logs. The fracture orientation and aperture data were determined using geophysical surveys. The fracture system of the study area is also highly affected by numerous dextral strike slip faults and dykes running through the fractured granite.

Hamm et al. (2007) related each of the three fracture characteristic parameters individually to hydraulic conductivity. The hydraulic conductivity is high in areas of high fracture spacing, related to areas with the same fracture spacing having low hydraulic conductivity. Hydraulic conductivity estimations are variable due to fracture persistence, the presence of hydrological boundaries, influence of free water surfaces and the possibility of water flowing around the packer of the Lugeon test. Low hydraulic conductivity values in fractures can possibly be due to clay matrix infillings, the closeness and healed character and poor connectivity in the testing area. They also found a higher correlation between the fracture apertures and hydraulic conductivity, than between fracture spacing and hydraulic conductivity. A lower relationship exists between hydraulic conductivity and fracture aperture of major orientation opposed to case of not considering orientation for fracture aperture, which could be due to the small scale of the investigated area, as well as the flow direction against the orientation of the fractures.

The assessment of permeability and injection depth in basalt and pyroclastic rocks at the Atasu dam site in Turkey, was conducted by Gurocak and Alemdag (2012) using both experimental and numerical analyses. Investigation studies were conducted in three stages, data was collected via core samples, scanline surveys and Lugeon tests within the core-drilled boreholes.

Gurocak and Alemdag (2012) analysed the relationship between permeability and discontinuity surfaces, and concluded that the discontinuity orientation is very important as the direction of water flow is governed by this parameter. The infilling of the discontinuities as well as the roughness will have a major effect on the permeability value. Although the basalts have moderate apertures filled with calcite veining, it is unlikely that the orientation parameter will increase the permeability. The pyroclastic rocks indicate that flow will occur along bedding planes, which are vertical to the dam axis, even though tight and weathered bedding planes

exist. The author also states that the permeability and injection depth of the rock mass is controlled by the discontinuity network and parameters such as aperture, spacing, infilling, roughness and orientation.

4.2. Packer (Lugeon) Tests

Packer tests are a type of constant head test used to obtain the in-situ hydraulic conductivity of a rock mass. These tests are also known as Lugeon tests and are expressed in Lugeon values with 1 Lugeon equivalent to flow of 1 litre per minute per meter, tested at a constant pressure of 1 MPa. In dam engineering, a value above 1 Lugeon generally implies that grouting is necessary to reduce seepage through foundation rock.

These tests are conducted in a portion of a borehole by pumping water through a perforated pipe at a constant pressure between a single packer and the base of a borehole or a section between two packers, as shown in Figure 4-1. Generally, five tests are conducted at different constant pressures per borehole section for a period of 10 min each. Both water pressure and flow rates are recorded for each stage. The average value of the flow rate and the water pressure is then used to calculate the Lugeon value for a specific stage.
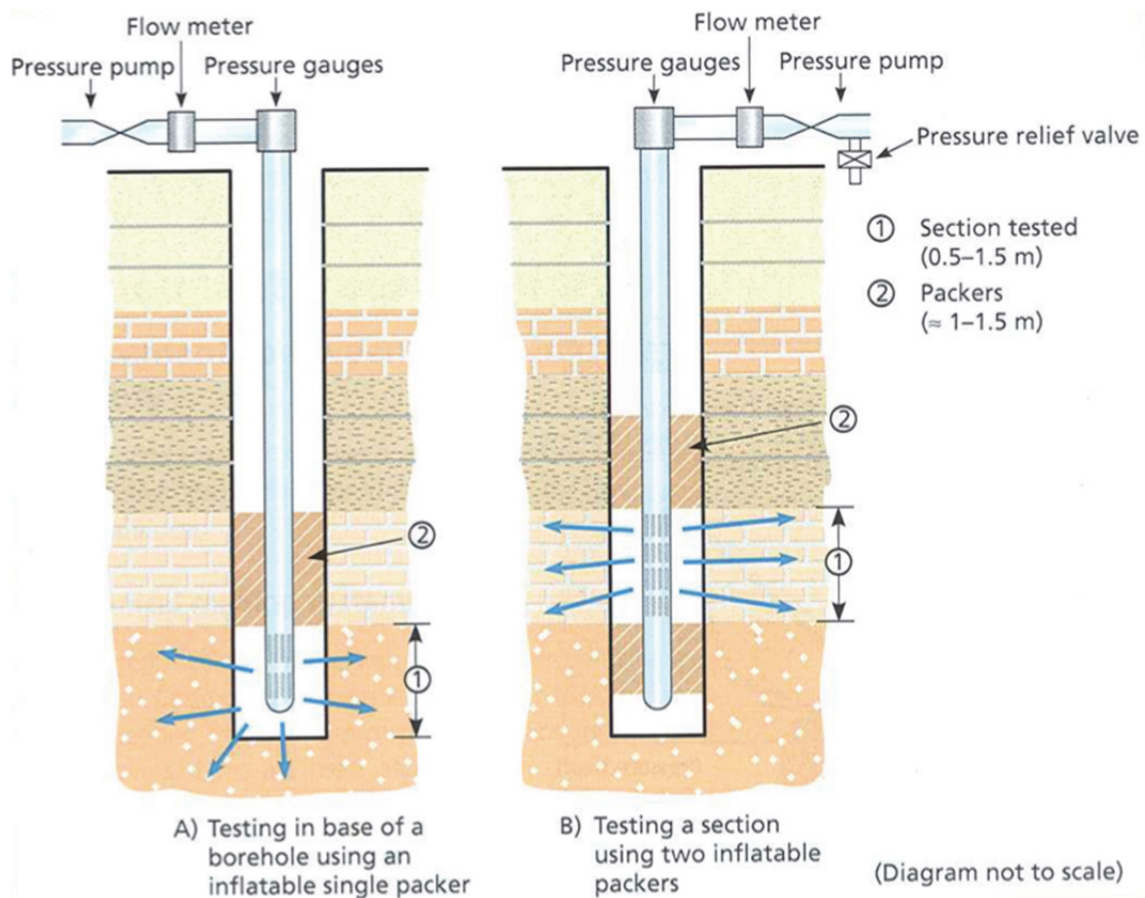
Figure 4-1. **Cross-sectional view of a general Packer test configuration. A) Single packer, B) Double packer (from González de Vallejo and Ferrer, 2011).**

5. MATERIALS AND METHODS

5.1. De Hoop Dam

The Department of Water Affairs (now the Department of Water and Sanitation) appointed De Hoop Dam Consultants (DHDC) to supervise the construction of the De Hoop Dam. Knight Piesold Consulting (KPC), on behalf of DHDC, supplied the following data:

- Discontinuity parameter data and stereographic plots from the dam foundation
- Permeability data from packer tests as conducted prior to and during grouting.

The complete case study, which includes the interpreted data, is contained in Appendix A, whilst the raw data set is held at KPC.

5.1.1. Geological foundation mapping

Geological mapping of each block on the dam foundation was conducted once the block was cleaned and ready for concrete placement. All the major geological features were recorded together with their orientation and were then plotted on graph paper. Digital photographs of each foundation block were taken from different angles, both in the upstream and downstream direction. In the case of specific or significant features more detailed and close-up photographs were taken. Mapped display sheets of each block were generated that contain the geological foundation mapping, stereo plots, typical foundation photographs and rock mass descriptions (Van der Merwe, 2013).

The joint line surveys were conducted in two directions namely parallel to the dam centreline (10 m) and a second survey perpendicular to the centreline. The perpendicular surveys were conducted starting from the upstream side. The length of these surveys varies due to the width of the foundation block for the dam wall, but range from 15 to 65 m. Larger blocks, such as the outlet and the spillway may contain up to three to four line surveys. Most of the perpendicular surveys were conducted on the centre of the foundation block or on the block interfaces (Van der Merwe, 2013).

The discontinuity parameters were recorded along a 50 m measuring tape placed on the exposed foundation and the following parameters were recorded for each intersected discontinuity: distance along the tape, rock type, rock description, orientation (dip and dip direction), continuity, joint surface roughness, gouge or filling and water (seepage).

A total of 1151 discontinuity entries were obtained from Block 88 to 118.

The stereographic projections of each block orientation were created using Rocscience DIPS V5.0®. Stereo plots of both joint line surveys in each block were created, with a third being the combined stereo plot of the two surveys (Van der Merwe, 2013).

Two as-built foundation maps, 18 block foundation mapping sheets and three grouting as-built maps were also obtained. The 18 as-built foundation mapping sheets contain detailed geological mapping of the most prominent geological features. These sheets also provide information on the orientation of the discontinuities found within the individual blocks, along with a short description of the rock mass. An example of one of the sheets is shown in Figure 5-1.

Figure 5-1.   **Example of an as-built foundation mapping sheet for a 10 m foundation block (Van der Merwe, 2013).**

5.1.2.   *Interpretation*

To find a correlation and/or relationship between discontinuity parameters and Lugeon values, statistical and comparative analyses were conducted. JLS data were captured into MS Excel © to facilitate statistical analysis as shown in Figure 5-2.

Dip	Dip direction	Block number	Ref line	Distance	Type	Hardness	Weathering	Structure	Dip Length	Dip Ends	Strike Length	Strike Ends	Roughness	Amplitude	Base	Aperture	Fill type	Fill consistency
13	291	88	Parallel	0.2	G	R4	S-U	T	1	1	0.7	2	10	40	0.6	0		
13	291	88	Parallel	0.6	G	R4	S-U	T	1	1	0.7	2	10	40	0.6	0		
88	185	88	Parallel	1	G	R4	S-U	T	0.1	0	0.6	2	11	10	0.2	0	Ss	
88	185	88	Parallel	1.3	G	R4	S-U	T	0.1	0	0.6	2	11	10	0.2	0	Ss	
86	54	88	Parallel	1.8	G	R4	S-U	T	0.05	0	0.7	2	10			0	Sd	
74	176	88	Parallel	2.3	G	R4	S-U	T	0.05	0	0.9	2	10			0	Sd	
74	176	88	Parallel	2.5	G	R4	S-U	T	0.05	0	0.9	2	10			0	Sd	
20	242	88	Parallel	3	G	R4	S-U	T	1.7	1	2.1	2	13	40	0.9	0	Sd	
87	327	88	Parallel	4.4	G	R4	S-U	T	0.05	0	1.5	2	12			1	Wr	
87	327	88	Parallel	4.6	G	R4	S-U	T	0.05	0	1.5	2	12			1	Wr	
87	327	88	Parallel	5	G	R4	S-U	T	0.05	0	1.5	2	12			1	Wr	
20	245	88	Perpendicular	0	G	R4	S-U	T	2.5	1	2.4	2	12	20	0.4	5	Sd	
85	15	88	Perpendicular	1.3	G	R4	S-U	T	0.2	0	0.3	2	10			0	Sd	
25	355	88	Perpendicular	1.6	G	R4	S-U	T	0.7	0	0.7	2	12	30	0.5	0		
70	30	88	Perpendicular	2.1	G	R4	S-U	T	0.2	0	1	2	11			0	Sd	
60	232	88	Perpendicular	2.3	G	R4	S-U	T	0.1	0	0.4	2	10			0	Sd	
21	294	88	Perpendicular	2.7	G	R4	S-U	T	0.5	1	1.5	2	12	10	0.3	0	Sd	
76	193	88	Perpendicular	3.8	G	R4	S-U	T	0.1	0	0.2	2	10			0	Sd	
77	54	88	Perpendicular	4	G	R4	S	T	0.2	0	0.5	2	11			1	Sd/Ss	

Figure 5-2.   Example of the final combined JLS data sheet.

The combined data sheet was used as the master file in the DIPS V5.0 program. The data were extracted statistically via queries and charts for analysis, and was also extracted via stereographic projections for correlation analysis. These methods are discussed in more detail in the sub-sections that follow.

The grouting as-built sheets were used to locate and identify high and low permeability zones of the different blocks, and these are presented in a summarised table. The distinction between low and high permeability was set at a Lugeon value of Lu = 5, where Lu < 5 being low and Lu > 5 being high. The geological foundation mapping as well as digital photographs was also consulted to identify possible geological significant features that may influence the characteristics and permeability of the rock mass. These significant features within the blocks were compared to their specific Lugeon values of the block to determine a possible correlation.

The large volume of JLS data entries were grouped into the three discontinuity types, viz. tension joints, fault fractures and stress-relief joints. Average values for each parameter that may influence the permeability of a rock mass were calculated for each discontinuity type. These parameter values were weighted against each other. The same statistical analysis was also conducted for the packer test data, whereby the low and high permeability blocks weighted against each other for all three discontinuity types.

Stereographic projections were used to establish possible correlations between the three discontinuity types, as well as between the high and low permeability blocks.

5.1.3. Packer tests

The packer tests were conducted in three stages. These tests were conducted using a single, downhole packer for each stage and comprised of 3 x 5 min steps at a constant pressure of 150 kPa. The Lugeon values and grout takes were obtained during the construction phase of the dam wall.

5.1.4. Numerical Model

Due to the good correlation that existed between seepage values and the presence of a pegmatite vein in block 108 and 110 at De Hoop Dam, Matlab® was used to numerically model this feature.

The as-built foundation maps of the exposed rock mass were used to model the pegmatite vein as it contained relatively detailed information on the geometry of the fracture, specifically regarding the strike and dip variations along its length within Block 108 and 110 (Figure 5-3). A local coordinate system was established whereby x, y and z coordinates where approximated from the foundation map, and subsequently extrapolated over the 3D block. The x-axis of the coordinate system follows the reference line of the dam and starts at a chainage of 720 m, and ends at a chainage of 700 m. The y-axis starts at the reference line and is positive towards the downstream side and negative towards the upstream side of the reference line. The z-axis starts 10 m below the excavation depth and increases with depth. A maximum depth of 10 m was chosen as this was the depth to which the relief wells were drilled.

Figure 5-3 outlines the process to determine the coordinates of the surface contact of the pegmatite vein. This entailed identifying a number of linear elements whereby the orientation of the pegmatite vein could be approximated. From this, five linear elements were identified and their orientation data are summarised in Table 5-1.

Table 5-1. **Orientation data for the modelled elements of the pegmatite vein.**

Element	x-start	x-end	y-start	y-end	Strike*	Dip-start	Dip-end
1	15.08	14.43	0	5.36	173.06	66.8	35
2	14.43	10.16	5.36	13.40	152.03	35	55
3	10.16	8.18	13.40	21.15	165.68	55	28.33
4	17.06	15.08	-15.89	0	173.06	66.8	66.8
5	8.18	5.63	21.15	31.13	165.68	28.33	28.33

*Note: the strike is relative to the x-axis (0°)

Element 4 is an extrapolation upstream of element 1, except for the dip which is kept constant from its start as no data was available on its orientation. Similarly element 5 is an extrapolation downstream of element 3 save for the dip which is kept constant from its start. The reason for including extrapolated elements was such that there is a region upstream (element 4) and downstream (element 5) of the dam wherefrom the hydraulic head can be calculated. These extrapolated elements extend 10 m to either side of the dam wall.
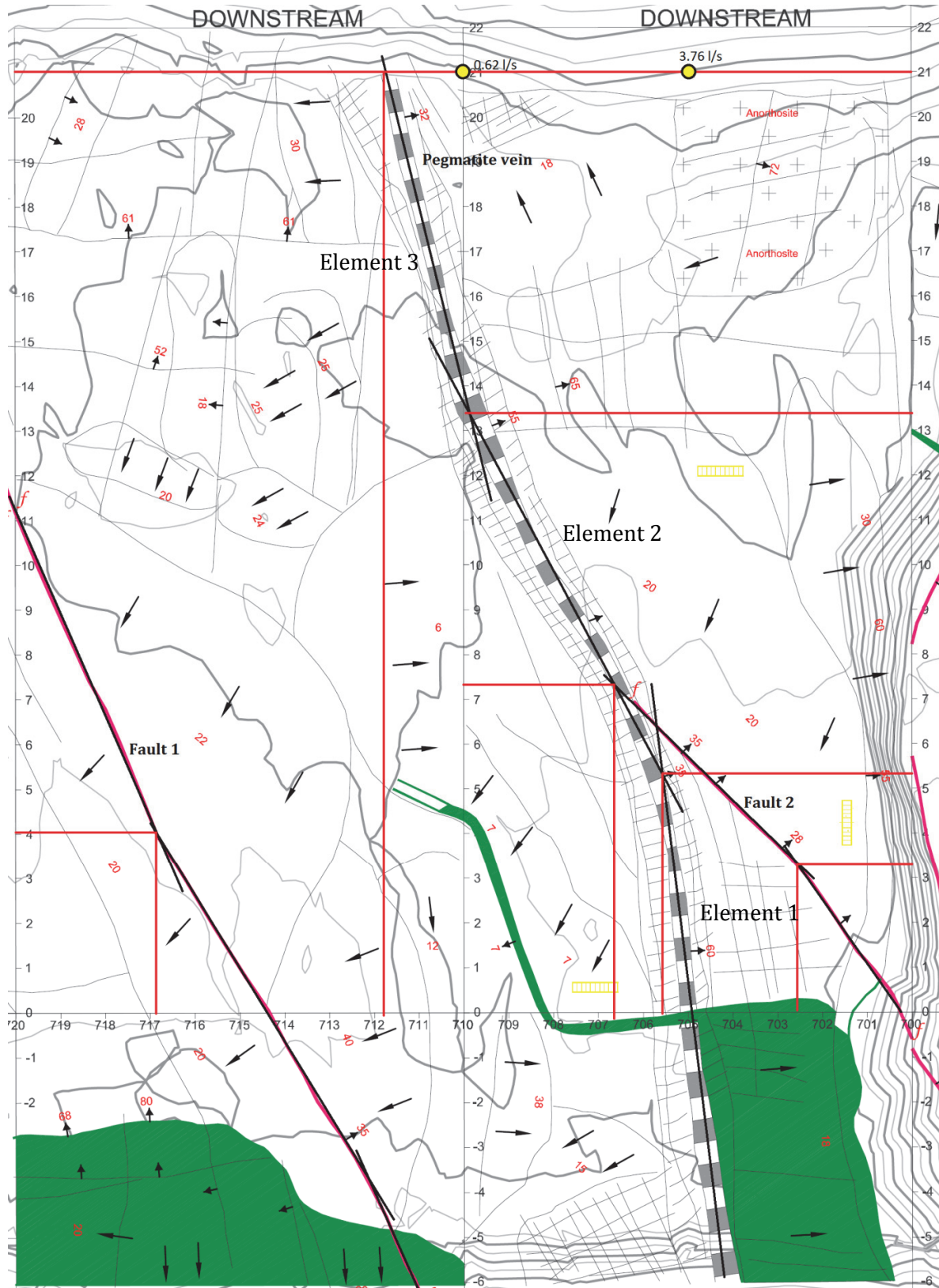
Figure 5-3. As-built foundation map of block 108 (right) and 110 (left). The black lines represent the approximated strike of each element, and the dip directions are represented by the small arrows. Dip magnitude is given by the red numbers.

5.2. Experimental Validation of Literature

Prior to attempting any full-scale field and laboratory testing, and modelling for verification of results, fundamental principles pertaining to variably saturated fracture flow and geotechnical centrifuge modelling were evaluated.

The following experiments seek to investigate the fundamental concept of the cubic law under conditions of variable saturation, both at 1G and under increased gravitational acceleration. The findings of these tests are expected to provide insight into the validity of the cubic law to unsaturated conditions, as well as assessing the use of geotechnical centrifuge modelling in addressing problems associated with unsaturated fracture flow in rock masses.

5.2.1. Vertical Clean Smooth Parallel Plates

The vertical model test was performed on a fracture measuring 100 mm height x 110 mm width, with a constant aperture of 1 mm (e_f). Figure 5-4 schematically shows the model set-up.
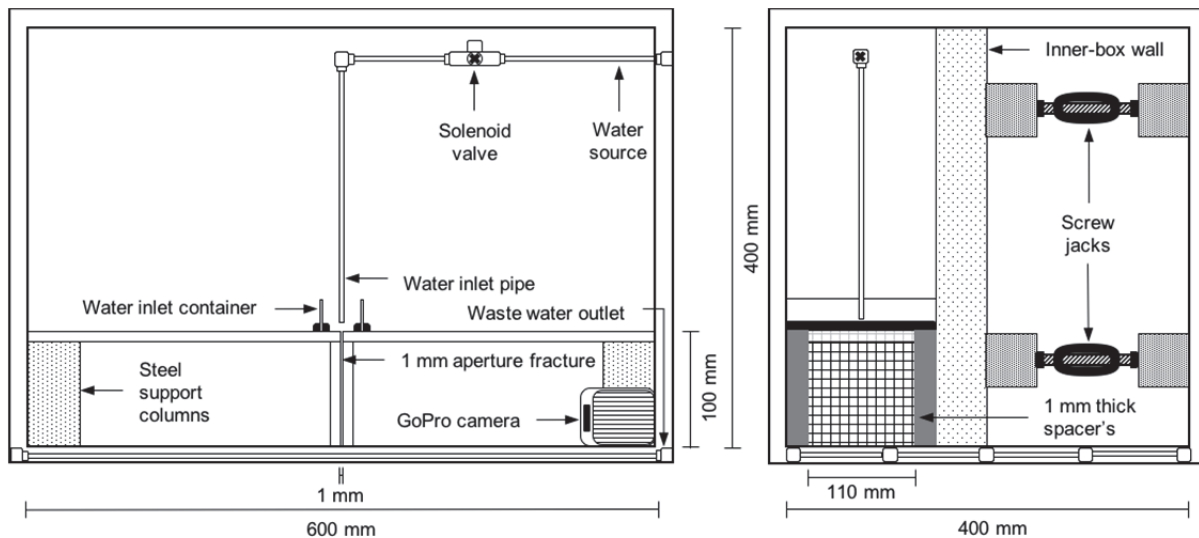
Figure 5-4. **Model set up for the vertical dry, smooth, parallel plate test. The cross-sectional view is shown on the left, with the side view (observing the vertical fracture perpendicularly) is shown on the right.**

A camera was placed at the right of the model in order to record the flow of water through the vertical fracture. The model was then constructed using two L-section Perspex sheets, 299.5 mm long placed in a strongbox measuring a length of 600 mm. This allowed a constant aperture of 1 mm to be maintained for the fracture between the Perspex sheets. The back inner-box wall was jacked into place and a water inlet container is constructed around the fracture. Foam sealant tape was placed around the inside and outside perimeter of the water inlet container to maintain a watertight seal. Crystals of potassium permanganate are scattered through the container to colour the water in order to make it visible. The model is placed on the geotechnical centrifuge platform, where a water input pipe with a solenoid valve is installed and

connected to remote access ports. A waste-water outlet is installed at the base of the model and all loose cables and wires are tied down.

The complete case study, with additional photographs and multimedia videos is contained in Appendix B.

5.2.2. Horizontal Clean Smooth Parallel Plates

The horizontal model test was performed on a horizontal fracture measuring 270 mm length x 110 mm width, with a constant aperture (ef) of 1 mm. The model was constructed using the same two L-section Perspex sheets, with one placed as an invert on top, slightly offset to allow for construction of the inlet container, as illustrated in Figure 5-5.

The use of spacers allowed a constant aperture of 1 mm to be maintained for the fracture between the Perspex sheets. Once the water inlet container was constructed on the left of the model and the foam sealant tape is placed around the inside and outside perimeter, the back inner-box wall was then jacked into place to maintain a watertight seal. Two cameras were placed, on position by a bracket above the model in order to observe the flow through the horizontal fracture, and the second on the right of the model in order to observe the outflow of water from the horizontal fracture, into an unconfined vertical wall. Crystals of potassium permanganate are again scattered throughout the container to colour the water in order to make it visible. The model is placed on the geotechnical centrifuge platform, where a water input pipe with a solenoid valve is installed and connected to remote access ports. A waste-water outlet is installed at the base of the model and all loose cables and wires are tied down.

The complete case study, with additional photographs and multimedia videos is contained in Appendix B.

5.2.3. Experimental Procedure

Two separate interval methodologies were adopted for the 1G and 20G test, respectively. These are illustrated in Figure 5-6. Three-minute interval stepped flux input increases where performed for the 1G tests, where an additional 20 l/h is added to the current flux until a total constant flux of 100 l/h is obtained for 3 minute. The water is then switched off and the system is allowed to drain for 2 minutes. A re-wetting phase follows the same stepped flux procedure stated above, but following a time interval of 1 minutes between increases. After the final minutes, the water and solenoid valve are closed, and the drying stage observed for 10 minutes.

For the accelerated tests, the completed model is accelerated to 20G when the solenoid valve is opened remotely and water is introduced into the system at a constant rate of 20 l/h. This is followed by 1-minute interval stepped flux input increases, where an additional 20 l/h is added to the current flux until a total constant flux of 100 l/h is obtained for 1 minute. The water is then closed off and the system is allowed to drain for additional minute. A re-wetting phase follows the same stepped flux procedure stated above, but following a time interval of 30

seconds between increases. After the final 30 seconds, the water and solenoid valve are closed, and the drying phase is observed for an additional 2 minutes.
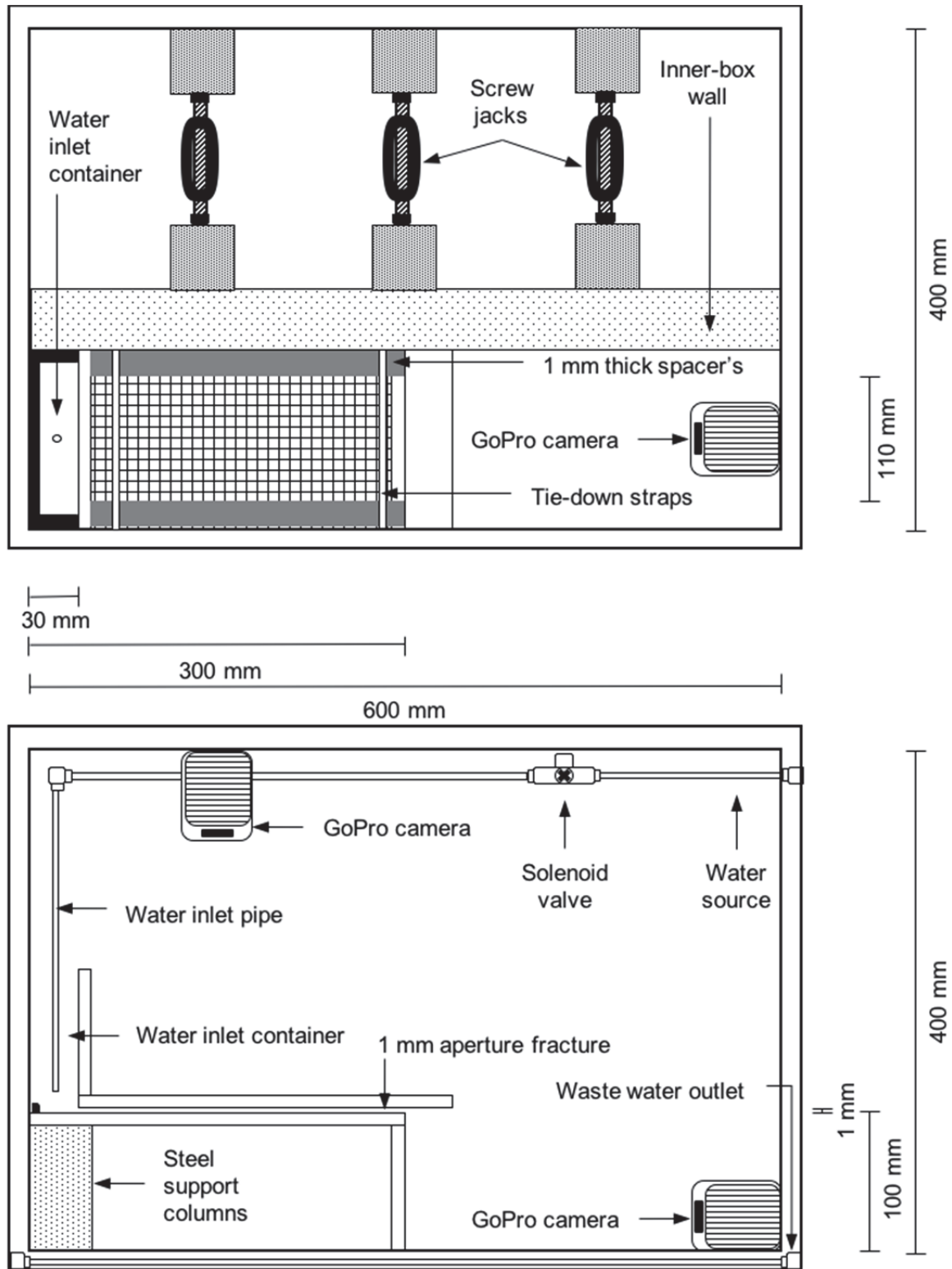
Figure 5-5. **Model set up for the horizontal dry, smooth, parallel plate test. The plan view (observing the horizontal fracture perpendicularly) is shown on the top, whilst the cross-sectional view is shown on the bottom.**
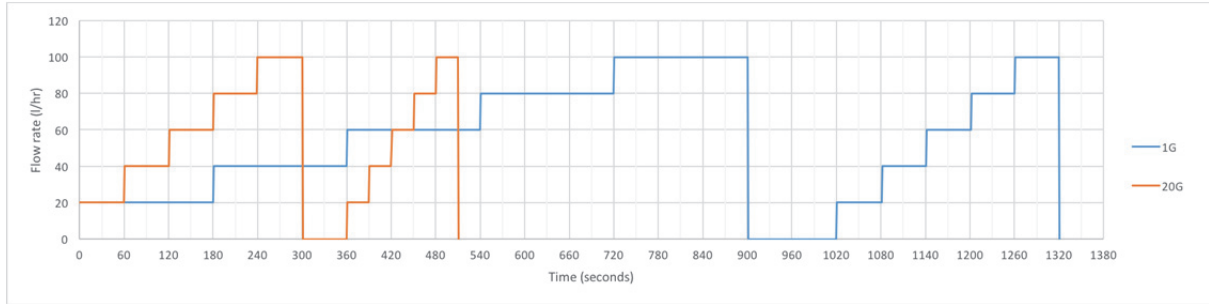
Figure 5-6. **Methodology for the continuous flow tests at 1G and 20G, showing the interval step fluxes.**

Initially testing only consisted of this addition of a continuous flow, but initial results highlighted the need to observe the flow regime under intermittent flow conditions. As such, the models where tested by slowing the inflow rate to approximately 0.7 l/hr, by discrete droplets. The procedure for this test was to let the intermittent flow continue for 3 minutes and then stop the experiment.

6. RESULTS AND DISCUSSION

6.1. De Hoop Dam

The De Hoop Dam was selected as prototype due to existing seepage along a well-defined discontinuity in the rock mass. Data from the investigation phase, foundation mapping during construction and Lugeon testing prior to and during grouting were available.

6.1.1. Discontinuity Analysis

The vast amount of discontinuity data was summarised into three main structural groups to facilitate the statistical analysis of the geological structures. All of the blocks were combined to calculate the averages of each structural group. In order to find a possible correlation between a discontinuity parameter or set of parameters that may influence the permeability, the structural group that would have the greatest influence on permeability was analysed.

Table 6-1 provides a summary of average parameter values between the three different discontinuity types under investigation.

Table 6-1.   Summary of the average parameter values for the three discontinuity types.

| Data entries | Rock description | | | | Continuity | | Surfaces | | | Gouge | |
	Structure	Hardness	Weathering	Type	Dip Length (m)	Strike Length (m)	Roughness (JRC)	Waviness Amplitude (mm)	Waviness Base (m)	Aperture (mm)	Type
1004	Tension joints	Strong rock 9rR4)	40% Slightly to un- 39% Slightly 13% Unweathered	86% Gabbro 10% Dolerite 4% Anorthosite	0.34	1.18	9.90	24	0.57	0.37	30% No data 37% Stained 8% Sandy silt
132	Fault fractures		46% Slightly to un- 24% Medium 14% Slightly	90% Gabbro 10% Anorthosite	0.31	5.23	11.31	146.27	2.25	16.60	27% No data 26% Stained 20% Weathered
15	Stress relief joints		47% Slightly to un- 33% Slightly 13% Medium	100% Gabbro	0.32	0.69	10.86	35.71	0.51	0.60	40% No data 20% Stained 20% Silt

Stereographic projections for each of the three major structural groups were analysed to find a possible trend between the groups that may influence the permeability. The tension joints indicate two major joint sets with the following average orientation J1: 298/18 and J2: 233/87, as shown in Figure 6-1a. The fracture faults show three prominent fracture sets, the orientations of which are S1: 140/58, S2 253/85 and S3: 216/80 (refer to Figure 6-1b). These fracture faults strike predominantly perpendicular to sub- perpendicular to the dam wall with some small parallel-striking fracture faults that also exist.
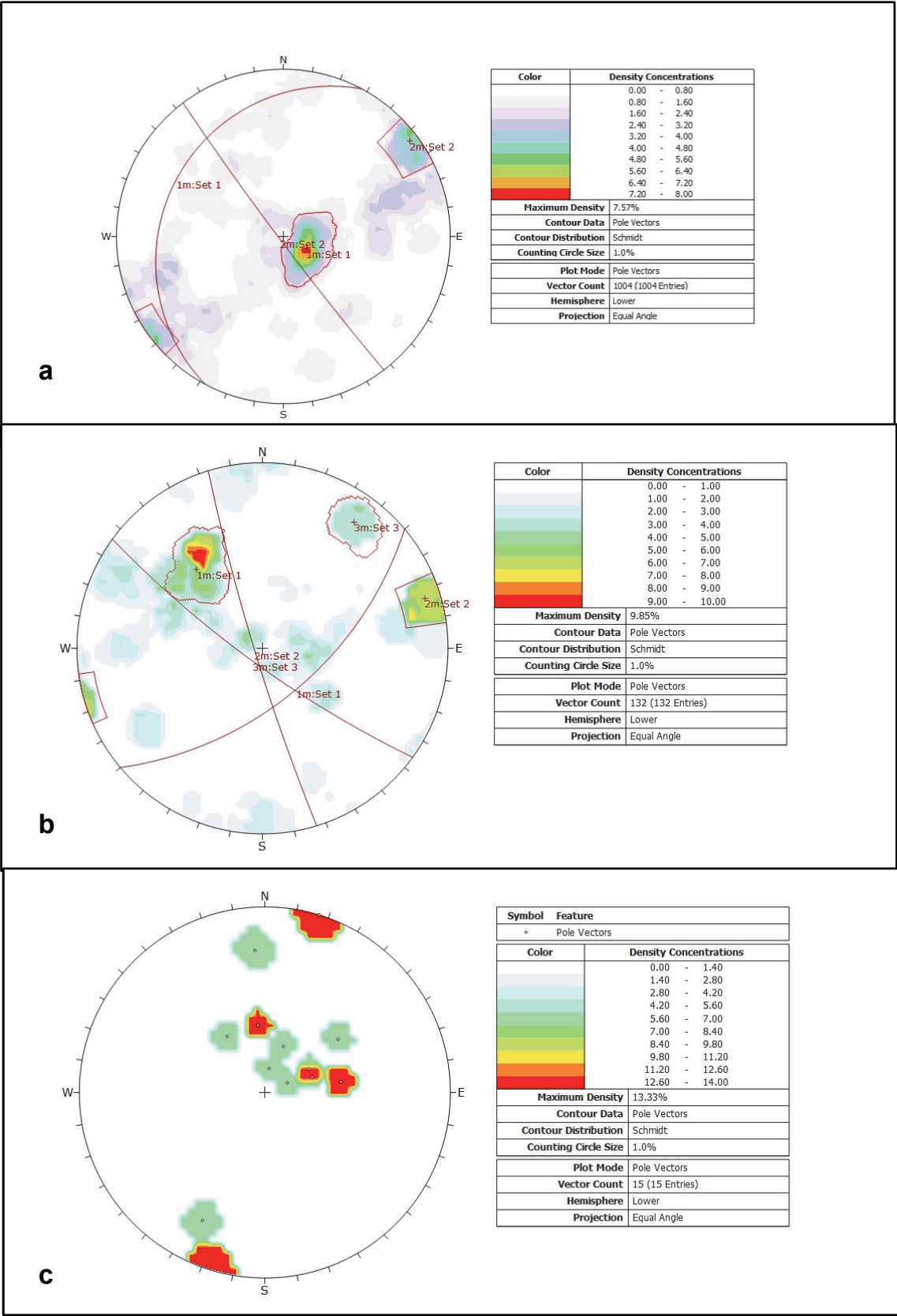
Figure 6-1. **(a) Stereographic projections of the tension joints with two prominent sets; (b) of the fracture faults with fracture sets; and (c) of the stress relieve joints (using DIPS V6.0® 2013).**

The 15 stress relief joints in Figure 6-1c shows no particular joint set orientation and the poles are scattered over the stereographic projection. Focus was placed on the fault fractures because the stress relief joints and tension joints are considered to not play a major role in rock mass permeability. The possible correlations between the low and high permeability fault fracture zones were investigated and a brief summary of certain parameters between the two is provided in Table 6-2. Parameters such as weathering, Joint Roughness Coefficient (JRC), aperture and filling are presented since these parameters play a major role in the permeability of a rock mass. The averages for roughness and aperture between the two zones are provided, where weathering and fill type gives the highest average values for each of the above parameters.

Table 6-2. Summary of some average values obtained for high and low permeability fault fracture zones.

Fracture faults	Weathering	Rough-ness (JRC)	Aper-ture (mm)	Fill type	Blocks
High permeable zones	Moderately weathered (40%) Slightly to unweathered (40%)	11.10	13.10	Mostly no data recorded (42%) Weathered rock/pegmatite (27%)	92, 94, 96, 108, 110, 114, and 116
Low permeabilit y zones	Slightly to unweathered (40%) Slightly weathered (40%)	11.50	20.30	Stained (40%) Weathered rock (27%)	88, 90, 98, 100, 102, 104, 106, 112, and 118

Figure 6-2 shows the stereographic projection of the fracture faults for zones of high permeability. In these blocks of high permeability, two prominent fracture sets can be seen with the sets S1; 149/64 and S2: 124/11. Most of the fracture orientations are still scattered as the maximum pole density is 11.76%. The two joint sets strike in a north-east direction, which is perpendicular to the dam wall.

A stereographical projection was also created for fracture faults situated in the low permeability blocks. This was done to ascertain how the low permeability and high permeability blocks relate to each other. As shown in Figure 6-3, the low permeability blocks have three prominent fracture sets opposed to the two of the high permeability blocks. This stereographic projection shows less scattering of poles than the high permeability blocks, with a maximum pole density of 14.06%. The orientation of the three fracture sets are S1:253/85, S2: 140/54 and S3: 217/80.

The JLS data of each block were grouped into three major structural groups to simplify the data and make it easier to analyse. The averages of all the parameters in the JLS were calculated. Although the roughness of the three major discontinuity types are more or less the same, the major difference is observed in the fill type, the aperture, the weathering and the orientation.
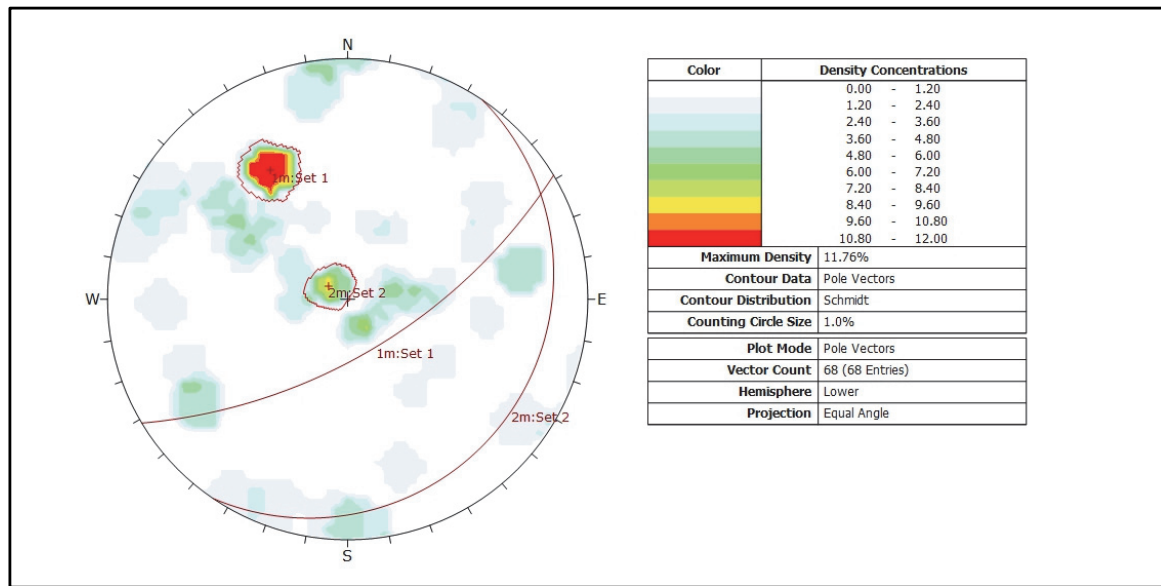
Figure 6-2. **Fracture fault stereographic projection of high permeability blocks (using DIPS V6.0® 2013).**
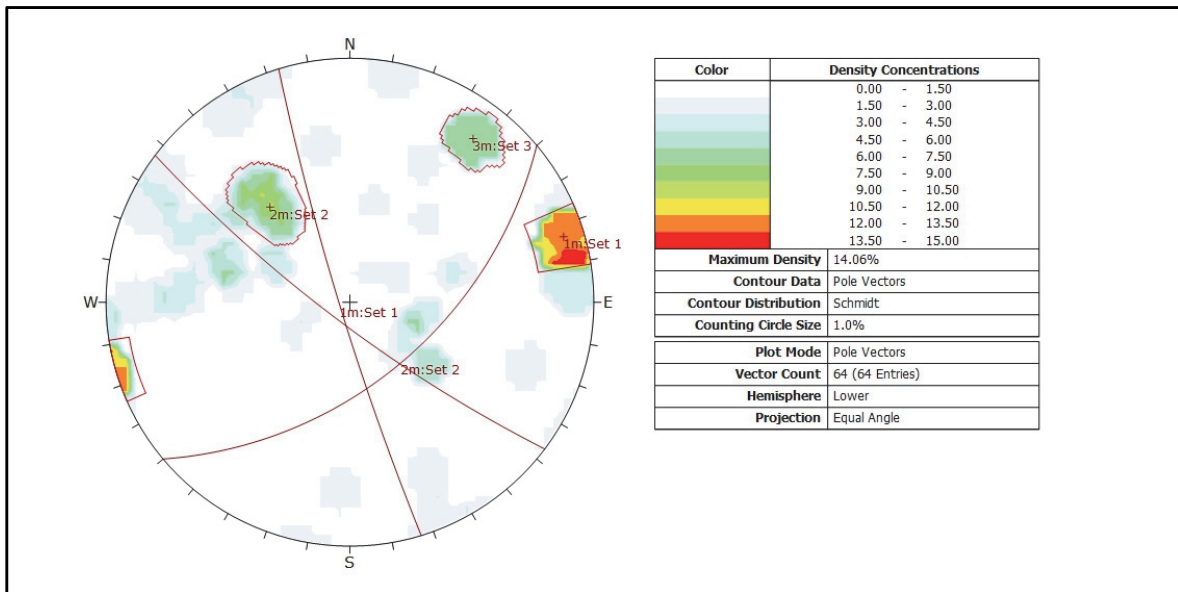
Figure 6-3. **Fracture fault stereographic projections of low permeability blocks (using DIPS V6.0® 2013).**

The tension joints, as well as stress relief joints, have apertures of 0.4 mm and 0.6 mm respectively. Two major joint sets can be seen in the tension joints, striking in a perpendicular and parallel orientation in relation to the dam wall. The stress relief joints have no specific orientation and are thus excluded from finding a possible correlation between low and high permeability. Although these two major joint types may transmit water, they do not have a major influence on the permeability of the rock mass due to their tight apertures. Most of these joints also do not have a recorded fill type measurement, which leads to the joints being partially closed to closed.

Therefore, for these purposes the focus was placed on fault fractures. Fault fractures would have sufficient apertures to transmit large quantities of water, which could influence the permeability of the rock mass. This can be seen by the average aperture of 16.5 mm for the fault fractures, which have more weathered surfaces than the other two major discontinuity types. The first two major fracture sets of the fracture faults strike perpendicular and sub-perpendicular to the dam wall. Thus, together with the aperture and weathering parameters, indicate that these fault fractures are preferred pathways for water flow under the dam wall. The fault fractures would be the focus point when attempting to find a possible correlation between the permeability and discontinuity parameters of a rock mass.

The seven blocks with Lu > 5 (high permeability) were compared to the 9 blocks with Lu < 5 (low permeability) for the fault fractures. In the low permeability blocks the fractures have an average roughness of JRC 11.5, which is slightly greater than the high permeability blocks with an average roughness JRC 11.1. On their discontinuity surfaces the low permeability blocks have an average waviness angle of 23°, opposed to the 4° of the high permeability blocks. This correlates well with the theory, stating that a rough discontinuity with high waviness angles have slower flow or lower permeability due to turbulent flow regimes.

The dip continuity (length and ends) between the low and high permeability zones of the fault fractures are approximately the same. The dip lengths for the two zones are approximately 0.3 m and the dip ends mostly disappear into the rock profile. A significant difference is observed in the strike length between the two zones. The average strike length for the low permeability zones is 7.4 m, opposed to the 3.2 m of the highly permeable zone. The persistence for the fault fractures tend to be longer in strike length and will therefore be more favourable to water flow along this continuous path. These results contradict the theory that states more continuous discontinuities are the preferred pathways for water flow

Another lack of trend occurs between the apertures of the two zones. The average aperture of the low permeability zone is 20.3 mm, which is wider than the 13.1 mm of the high permeability zone. This tends to contradict the theory (e.g. Singhal and Gupta, 2010; Sahimi, 2011) which state that a larger aperture would allow for more flow of water. However, more parameters than this are linked to aperture, namely, weathering, presence of infill, the fill composition and nature, roughness of surface and the stresses acting on the opening. High permeability blocks contain more fractures that have medium weathered surfaces opposed to the slightly weathered surfaces of low permeability blocks. The discontinuity surfaces of low permeability blocks are mostly stained with some weathered rock infill. The high permeability blocks have a large amount of missing fill data, but show some stains with a few pegmatite and weathered rock fillings.

It should be noted that an additional three pegmatite veins occurring in the investigated area have been geologically mapped, and were not always included in the JLS. From analysing the foundation mapping blocks and descriptions the pegmatite veins tend to occur in faulted zones and are filled with loosely packed pegmatite gravel or quartz gravel. These pegmatite veins can

transmit significant amounts of water due to their aperture size, weathered state and loose packed infill material. Most notably, a good correlation exists in block 108 and 110, where high seepage values have been measured, with a prominent pegmatite vein running through the foundation of the dam.

6.1.2. *Numerical model: pegmatite vein*

The numerical model presented in the following section is based on the pegmatite vein identified in block's 108 and 110, and was modelled using Matlab®. The resulting hydraulic head distribution for the pegmatite vein given in Figure 6-4 was determined in a homogenous manner. A detailed methodology for the numerical model is presented in Appendix A.
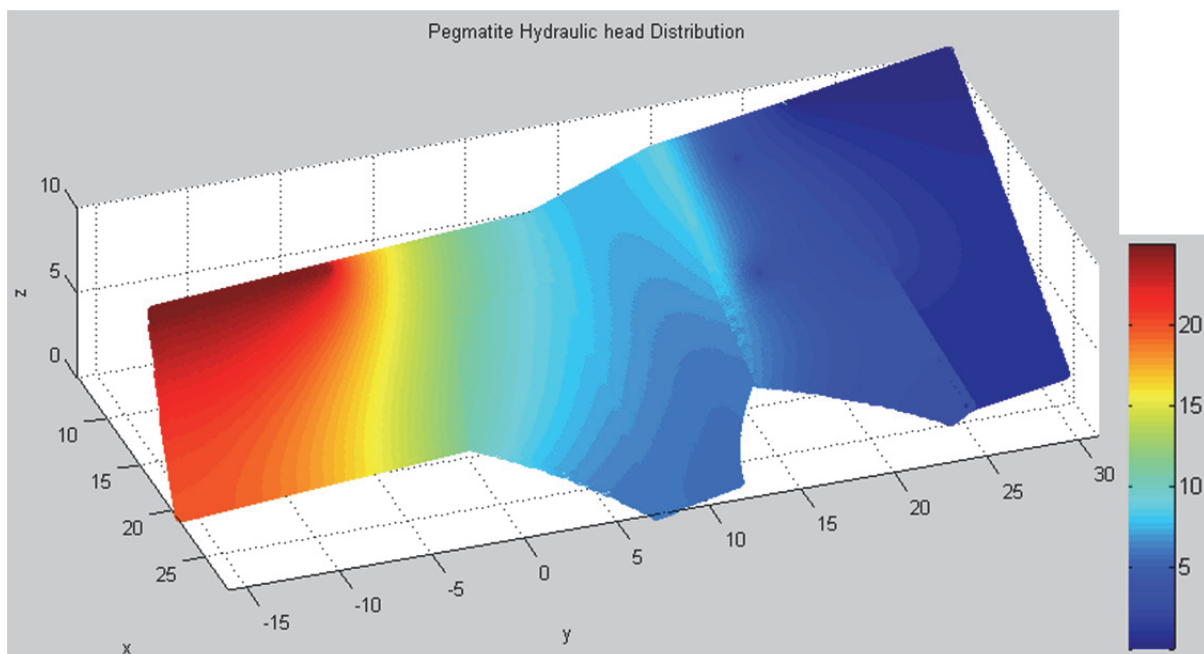
Figure 6-4.   The hydraulic head distribution within the assumed isotropic and homogenous pegmatite vein.

Figure 6-5 is a close-up on the relief wells, where it can be seen that the equipotential lines are distributed such that they tend more towards normal angles to the drains/wells when in closer proximity to them. This is due to the fact that the flow direction tends more towards the drains as it approaches them. Furthermore, a high concentration of flow lines can be seen around these drains, principally upstream of them. This indicates that the hydraulic gradient is significantly larger around the drains; thus indicating higher flow rates.
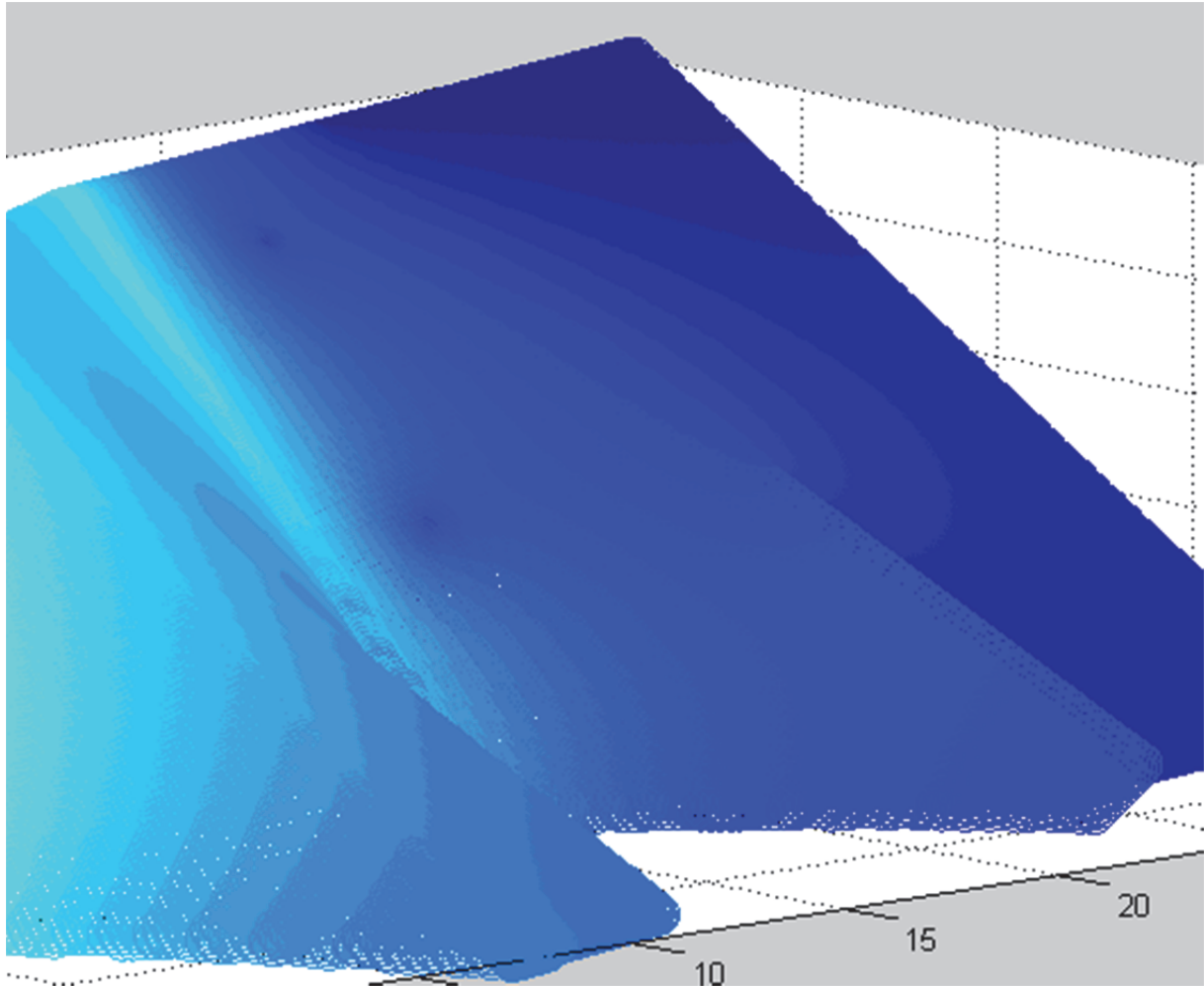
Figure 6-5. **Close-up view of the hydraulic head distribution around the relief wells.**

The relief wells were distributed such that there is one between and one in the centre of each block on the immediate downstream side of the dam wall. The wells of interest along with their measured and numerically modelled discharges are given in Table 6-3.

Table 6-3. **The instantaneous (1-step) and measured discharge into the relief wells.**

Well	Location	Discharge (l/s)			
		Measured	Modelled without fill	Modelled with fill	
				K=1.00e-03 m/s	K=1.00e-09 m/s
1	Boundary of Block 108 & 110 X=10 m; Y=21 m	0.62	2.2091 e+05	0.4500	3.2646 e-07
2	Centre of Block 108 X=15 m; Y=21 m	3.76	1.6027 e+05	0.3265	4.4997 e-07

Due to the large differences in hydraulic conductivity used in the flow modelling, a very large range in discharge into the wells was obtained.

The clean fracture yielded the highest seepage, being significantly larger (by several orders of magnitude) than that of the measured discharge. This result is not feasible as seepage from this single fracture into the wells cannot exceed that of the measured seepage by such an extent so as to account for measurement or assumption errors. Furthermore, the feature was characterised as having infill, thus this result purely marks the upper limit for possible seepage through the fracture/pegmatite vein in the scenario where erosion has removed the infill.

The lower limit of the hydraulic conductivity for a clayey infill yielded discharges well below (by several orders of magnitude) those of the measured discharges recorded for either wells. These results are not necessarily unrealistic as other seepage paths, not included in the model, may have accounted for the additional seepage. This is however unlikely, as the pegmatite vein is deemed to account for the large majority of seepage due to its favourable flow properties.

The upper limit of the hydraulic conductivity for a weathered and fractured crystalline infill yielded values much closer (within one order of magnitude) to those of the measured discharge, in relation to the other results. This result is definitely feasible as it accounts for the dominant impact the pegmatite vein is predicted to have on the seepage through the rock mass.

Due to the large variation in results for the modelled seepage into the relief wells, the range in results would essentially accommodate any practical measured discharge. Furthermore, the large number of assumptions required in order to initially model the pegmatite vein resulted in a model that could potentially be highly inaccurate. As a result, the credibility of the results cannot be determined accurately, only inferred.

The upper limit of the hydraulic conductivity for the fractured crystalline infill provided the most feasible modelled seepage. This result is promising in the sense that a pegmatite vein by definition should contain crystalline infill. Furthermore, due to the thin nature of this deposit and the anticipated seepage through it, a highly fractured and weathered infill can be expected. As a result, the upper limit hydraulic conductivity assumed may potentially be representative of that of the pegmatite vein. If this is the case, and the modelling assumptions of the plane are respectable, then the upper limit hydraulic conductivity seepage result can be deemed acceptable.

6.2. Vertical Clean Smooth Parallel Plates

Findings from the numerical model highlighted short-comings in fundamental conceptual theory. As such, the cubic law was revisited in order to assess the parallel plate theory. This lead to a process of validating fundamental conceptual model. The results of a vertical clean, parallel, smooth fracture are presented in the following section.

Results of the 1G model test, which was not accelerated, represent a 1 mm aperture fracture, whilst the second test was accelerated to 20G, which according to linear scaling laws for the centrifuge, represents a 20 mm aperture fracture. A detailed presentation of the tests is provided in Appendix B.

6.2.1.   1G Conditions

The observed flow regimes in the continuous flow test consist of a number of air-water menisci invading the vertical fracture as a droplet, with a thread behind which does not snap but forms a continuous rivulet.   Each rivulet is approximately 2 to 3 mm in width.   A number of these rivulets form throughout the vertical fracture, oscillating during all intervals (Figure 6-6).   In contrast, the intermittent flow experiment highlights how a thread behind a droplet moving through the fracture snaps and leaves static and localised droplets along the flow path (Figure 6-7). Subsequent droplets follow the same path as determined by the position of these static droplets.   Most notable is that even at high inflows into the vertical fracture, full saturation is not met but rather these fixed set of rivulets (approximately 30% of the cross-sectional area) were maintained to drain the overlying influx of water.
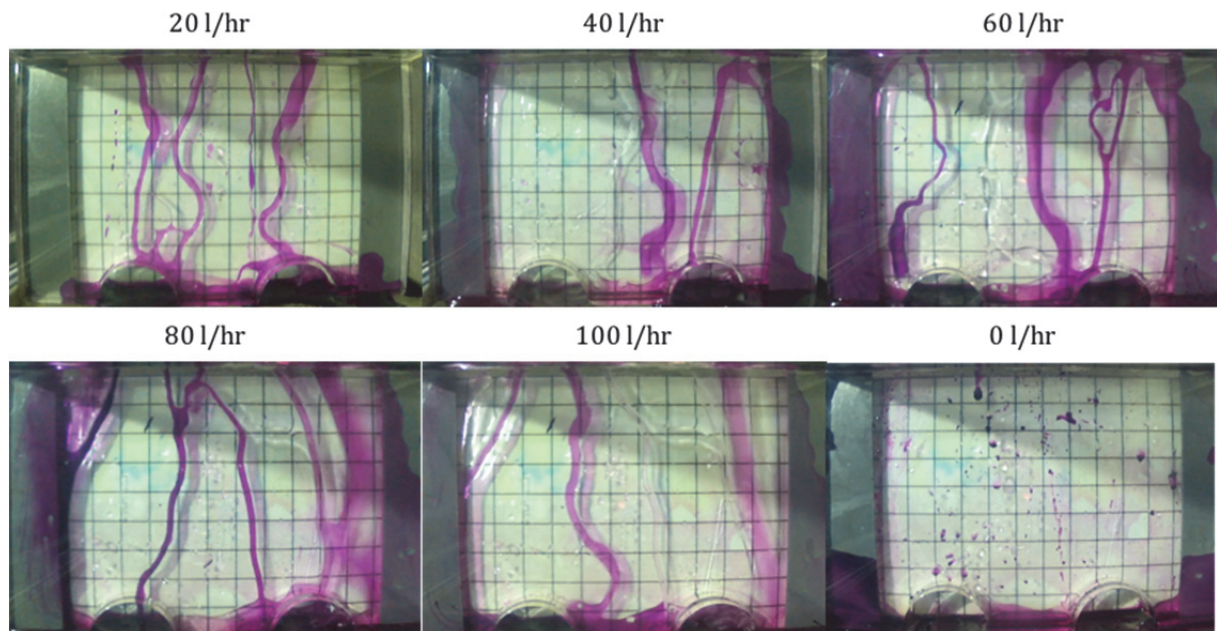
Figure 6-6.   **Screenshots of the continuous flow experiment at each interval during the test, under 1G conditions (10 mm x 10 mm grid).**

The flow that occurs within the fracture mimics the findings of Su et al. (1999) and Dragila and Weisbrod (2003), whereby initially there are snapping droplets, until ultimately there are fully maintained rivulets within the fracture. This supports the conceptual models of film flow proposed by Tokunaga and Wan (1997) and droplet flow proposed by Doe (2001), illustrating that these flow regimes do play a significant role. As Hsieh et al. (2001) stated, the interaction of film and capillary forces is still poorly understood but it is a current research area in unsaturated fluid mechanics with multiple authors attempting to comprehend the complex flow regimes and force interactions (Tuller and Or, 2002; Ghezzehei, 2004; Peters and Durner, 2008; Lebeau and Konrad, 2010; Zhang, 2011; Kordilla et al., 2013).
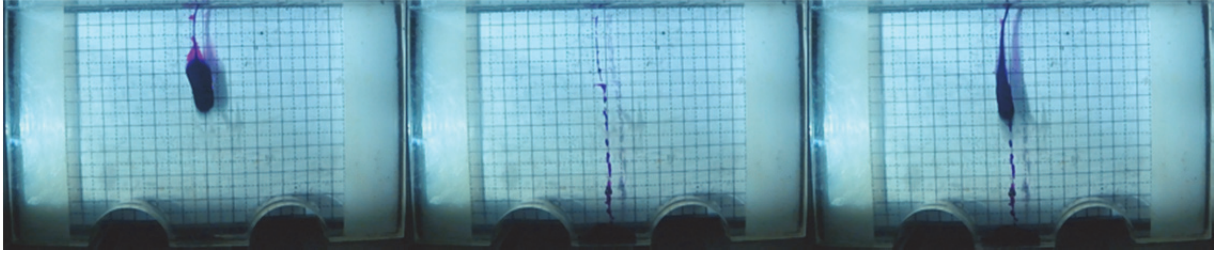
Figure 6-7.   Screenshots of the intermittent (droplet) seepage experiment, under 1G conditions (5 mm x 5 mm grid).

6.2.2.   20G Conditions

The 20G test mimics the findings of the 1G test, whereby oscillating rivulets occupy approximately 10% of the cross-sectional area at lower influxes, with no more than 30% being saturated at higher influx intervals (Figure 6-8).
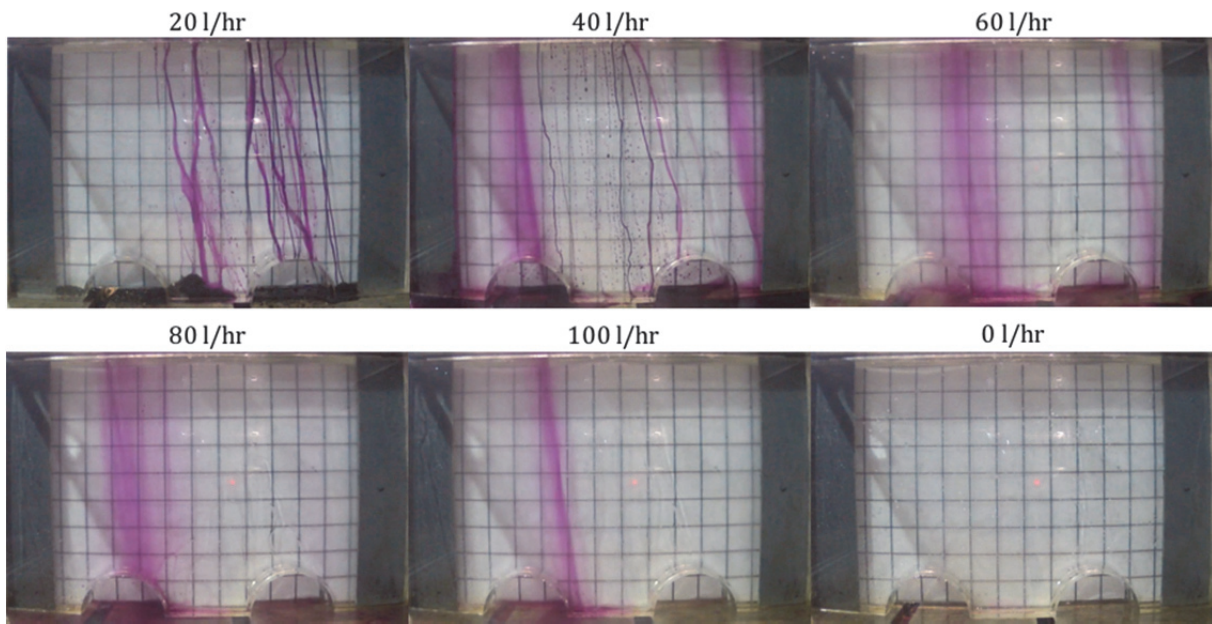
Figure 6-8.   Screenshots of the continuous flow experiment at each interval during the test, under 20G conditions (10 mm x 10 mm grid).

At lower influx intervals thin rivulets are approximately 0.5 to 1 mm in model width, which corresponds to a width of 10 to 20 mm in prototype scale. It is evident that these rivulets do not occupy the entire aperture of the fracture and are not constrained between both fracture walls, thus highlighting an important observation of film flow. At higher volumetric influx intervals these rivulets tend to give way to a much wider film flow, almost mimicking a wide sheet flow along a fracture wall.

At 20G in the intermittent seepage test, droplet flow as identified by Su et al. (1999) and Dragila and Weisbrod (2003) is also observed, as in the 1G test (Figure 6-9). The observation of this flow regime at increased gravitational acceleration importantly eludes to the centrifuge potentially being valid in answering questions relating to conditions of variable saturation within fractures.
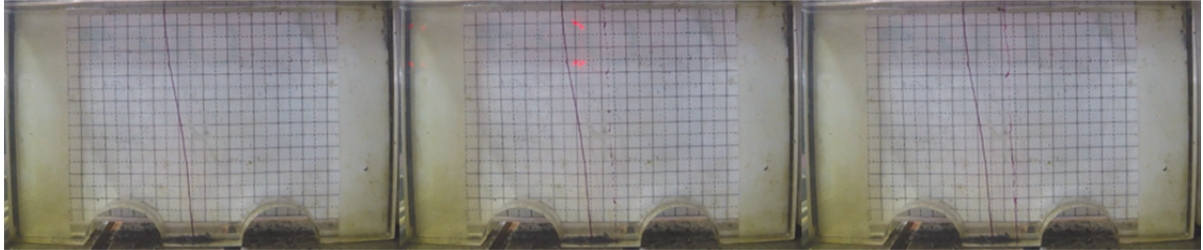
Figure 6-9. **Screenshots of the intermittent (droplet) seepage experiment, under 20G conditions (5 mm x 5 mm grid).**

6.3.   Horizontal Clean Smooth Parallel Plates

The following section provides a discussion of the results from a horizontal smooth, clean, parallel, fracture, and the water regime at the exit into an unconfined vertical wall. Results of the 1G test, which was not accelerated, represent a 1 mm aperture fracture. The second test was accelerated to 20G, which according to linear scaling laws for the centrifuge, represents a 20 mm aperture fracture. Appendix C provides a detailed presentation of the results from both tests.

6.3.1.   1G Conditions

The observations from the horizontal fracture support the cubic law, whereby the entire horizontal fracture is saturated for both conditions of continuous flow and intermittent flow, before flow is observed exiting at the vertical wall. Figure 6-10 presents the observations from the continuous flow tests, whilst Figure 6-11 presents screenshots of the intermittent flow test. Although full saturation of the horizontal fracture is maintained, the vertical wall is variably saturated with water exiting the horizontal fracture at discrete points as oscillating rivulets. As the flow rate is increased per interval in the continuous flow test, these rivulets occupy an increasingly wider cross-sectional area of the vertical fracture. They carry an increasingly larger volume of water from the horizontal fracture occupying a surface area from 20% to 45% at the highest inflow interval. Upon drying, a large single capillary island invades the horizontal fracture from the inlet, which leads to scattered discrete capillary islands evident in the horizontal fracture during the re-wetting stages.
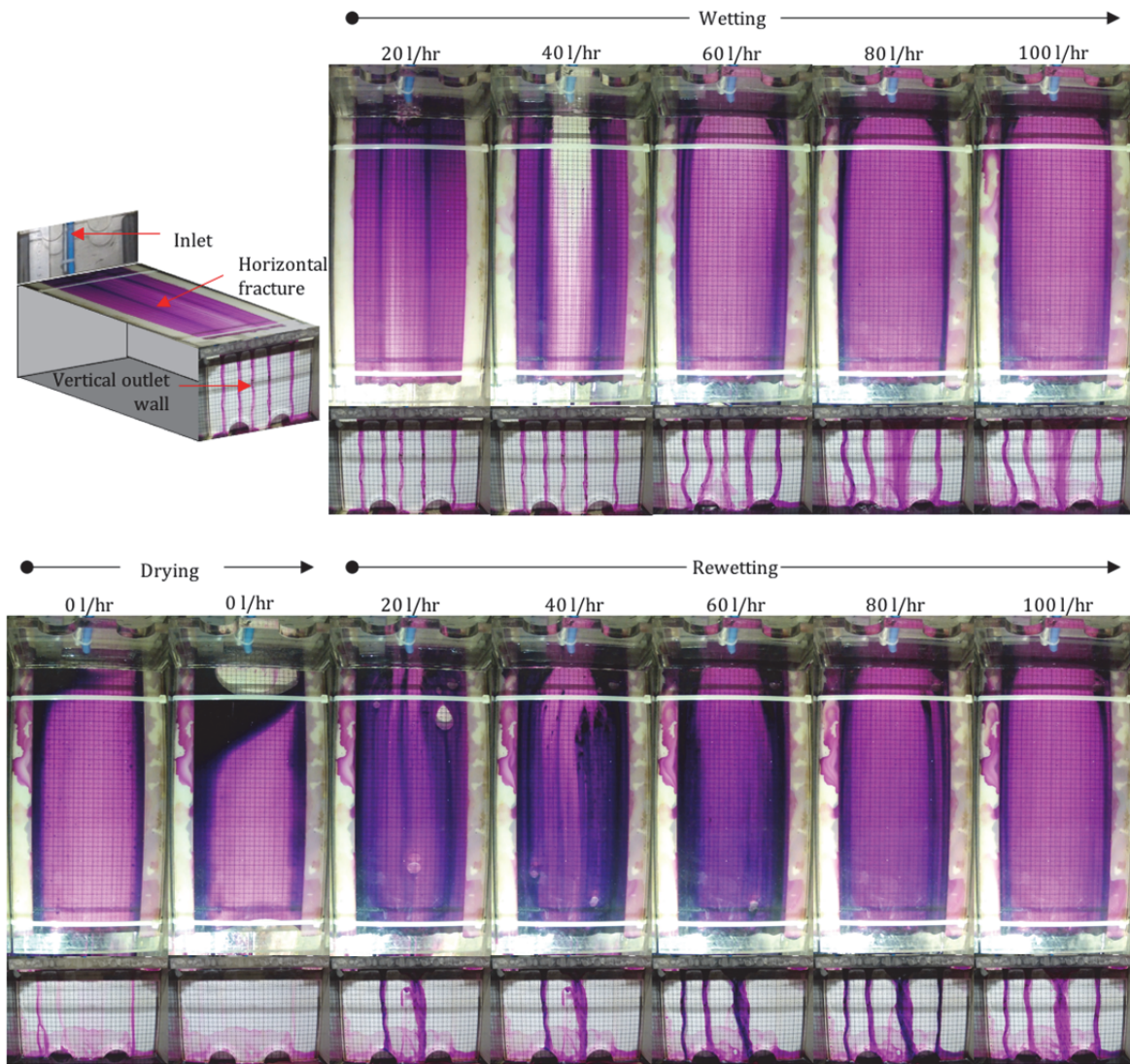
Figure 6-10. Screenshots of the horizontal fracture and vertical wall for the continuous flow experiment at each interval during the test, under 1G conditions (5 mm x 5 mm grid).

Figure 6-11. Screenshot of the horizontal fracture (elongated picture) and vertical wall (shorter picture) for the intermittent (droplet) flow experiment, under 1G conditions (5 mm x 5 mm grid).

Static capillary islands are removed as the flow rate is increased. Water from the horizontal fracture again exits at discrete points along the vertical wall as rivulets. The same regime is observed under intermittent seepage conditions, where the horizontal fracture is saturated with only a single discrete point at the vertical wall forming a rivulet which does not snap.

6.3.2. 20G Conditions

Although the model dimensions are the same as the 1G test, according to centrifuge scaling laws, the 20G test represents a horizontal fracture with the following properties at prototype scale: a length of 5.4 m; a width of 2.2 m; and an aperture of 20 mm. When the horizontal fracture is fully saturated it is holding a volume of 29.7 ml in model dimensions, which corresponds to 237.6 l in prototype. Full saturation is only achieved in the continuous flow tests and is achieved throughout all intervals provided that the inlet volume is continuous (Figure 6-12).
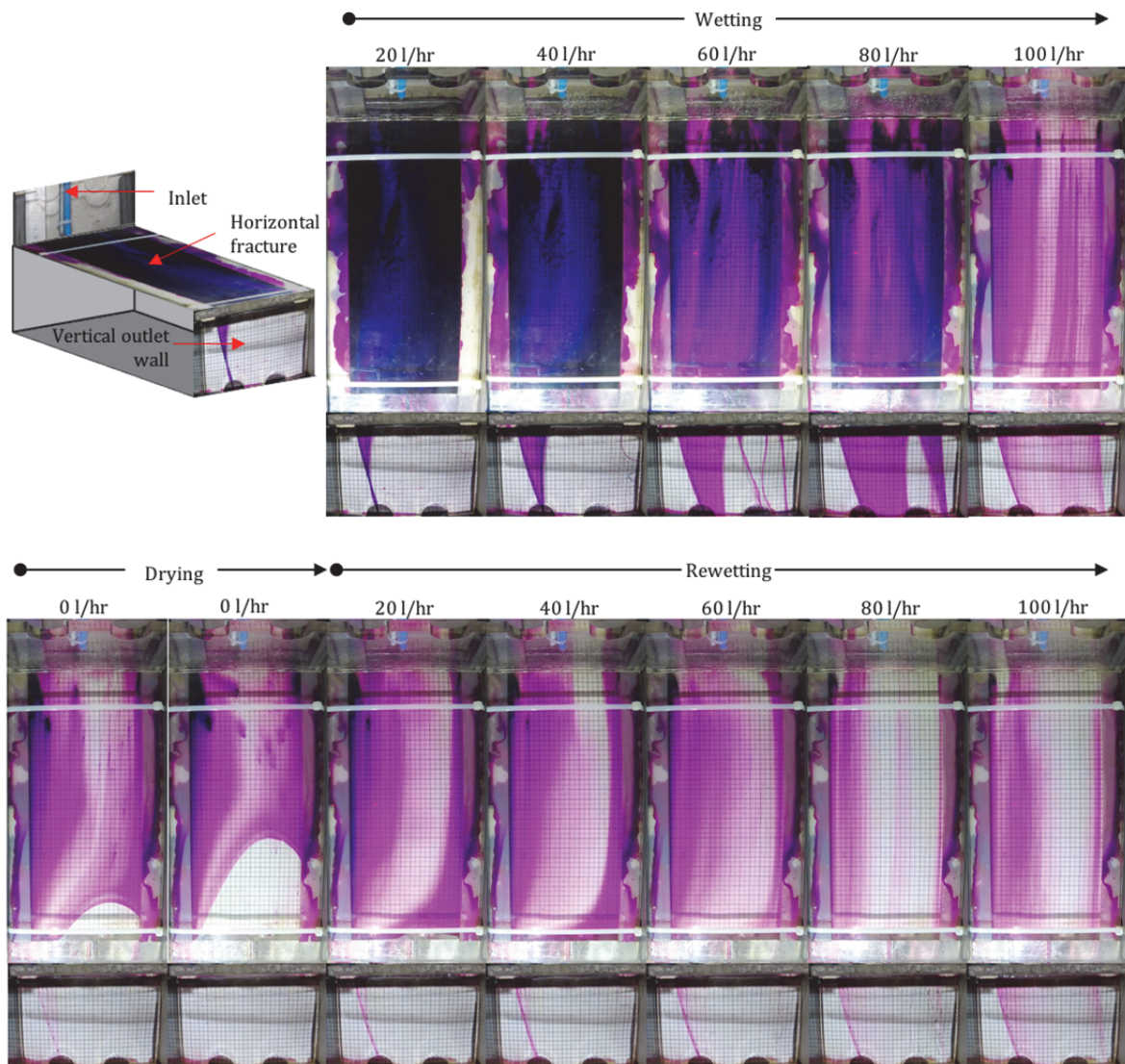
Figure 6-12. Screenshots of the horizontal fracture and vertical wall for the continuous flow experiment at each interval during the test, under 20G conditions (5 mm x 5 mm grid).

As soon as flow is stopped or reduced, even briefly, a capillary island invades the horizontal fracture. In contrast, only partial saturation conditions occur throughout the intermittent flow test with approximately 60% of the horizontal fracture being saturated. At the vertical wall, the flow regime observed is that of discrete droplets approximately 1 mm in width (Figure 6-13).
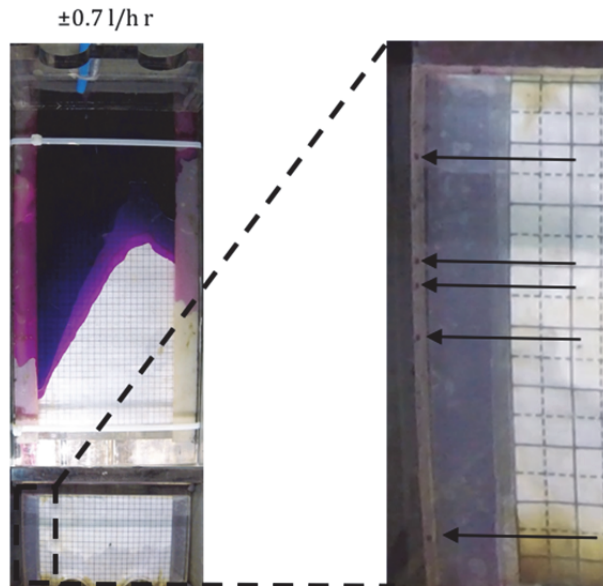
Figure 6-13. **Snapshot of the horizontal fracture (elongated picture) and vertical wall (shorter picture) for the intermittent (droplet) flow experiment, under 20G conditions (5 mm x 5 mm grid). Arrows indicate discrete droplets.**

7.   CONCLUSIONS

7.1.   Flow through the Fractured Intermediate Vadose Zone

Flow through the fractured rock part of the intermediate vadose zone was researched using the De Hoop Dam as a field model. The seepage along structures through a section of the dam wall created the opportunity to use the original site investigation, as-built plans and present seepage data to construct 1G, accelerated geotechnical centrifuge 20G, and numeric models based on the prototype site conditions.

Present research looked only at the validity of existing fracture flow models for a single fracture due to the lack of valid theory and empirical equations to quantify flow through a rock mass. In literature discontinuity orientation, aperture, roughness, infill, continuity, and spacing are listed as the most critical parameters influencing flow through rock discontinuities without any published correlation including all the above.

The De Hoop dam near Steelpoort was used to determine if a correlation exists between a single or set of discontinuity parameters and high or low Lugeon values in a rock mass. Joint line survey (JLS) data along with Lugeon permeability tests were used in statistical and comparative analyses of Blocks 108 to 110 of the dam wall. These blocks were chosen as experimental site due to known high permeabilities determined during the packer testing and present seepage through the dam foundations at these blocks. The analyses concluded that the permeability is highly affected by the characteristics of discontinuities in a rock mass. Furthermore, the discontinuities that exist in a rock mass are governed by the geological and geomorphological origin of the rock, as well as pre-tectonic stresses. This leads to a large amount of variables that may influence the characteristics of the rock mass.

From the study the conclusion can be reached that it is highly unlikely that only a single discontinuity parameter is responsible for high or low Lugeon values. A more plausible answer is that rather a set of parameters are responsible for high or low Lugeon values. A single discontinuity parameter may have a great impact on the permeability of the rock mass, but will not be solely responsible. It should also be noted that the results are highly dependent on the quality of the input data, which included JLS and Lugeon tests for this particular research site. The quality of the JLS is dependent on the knowledge and experience of the engineering geologist. Lugeon tests only give an indicative permeability value around a certain borehole and intersected discontinuities and not the true permeability value of the entire rock mass.

However, it has been determined that the pegmatite veins associated with the fault fractures that contribute mostly to the high seepage values in the dam foundation. Most notably, a good correlation exists in Blocks 108 and 110, where high seepage values have been measured, with a prominent pegmatite vein running through the foundation of the dam.

It was also established that the fault fractures in high permeability blocks have a lower roughness coefficient and waviness angle compared to the low permeability blocks with higher roughness and larger waviness angles.

Due to the significant seepage that has occurred below the De Hoop Dam wall, an investigation was set in order to attempt to quantify this seepage through a single feature in the rock mass. The feature modelled was a pegmatite vein present below Blocks 108 and 110 of the dam wall. The various structural properties of the pegmatite vein were determined from a combination of joint line survey data and surface maps. The available data were subsequently extrapolated such that a 3D model of the pegmatite vein could be obtained.

Prior to modelling the flow through the plane, the hydraulic head distribution was determined through the use of a numerical flow net analysis method. These hydraulic heads were subsequently used, along with the modelled plane, to model the seepage through the pegmatite vein. The results obtained were correlated with measured discharge values from two relief wells drilled into Blocks 108 and 110.

The numerically modelled discharges varied significantly over the ranges of hydraulic conductivity assumed; and as such, no clear result can be validated with the measured discharges. However, the most likely assumed hydraulic conductivity yielded discharge results within one order of magnitude to that of the measured discharge.

7.2.   Flow through Single Smooth Parallel Plates

Smooth parallel plate models were constructed to address flow through single horizontal and vertical fractures, aiming to address flow regimes and the applicability of the cubic law. Whereas horizontally orientated models appears to achieve near-saturation at both 1G and 20G centrifugal acceleration under variable water supplies, the vertically orientated models never achieved near-saturated conditions.

The validity of the cubic law can be questioned from the results on a vertical, smooth, clean, parallel fracture, seeing that:

- Full saturation is not ever truly achieved, regardless of centrifugal acceleration or water supply.
- Flow remains as oscillating rivulets and, occasionally, as localised sheets with substantial air pockets.
- Flow achieved is neither uniform, laminar nor saturated.
- The same flow regimes are observed even when water supply is from a saturated horizontal fracture with the same aperture.

Although full saturation was observed in some of the horizontal, smooth, clean, parallel plates test, it appears to be compromised when inflow conditions are intermittent, with partial saturation observed in the models tested at increased gravitational acceleration. Moreover,

even if the horizontal fracture is fully saturated, this saturation is lost as the fluid exits at the vertical wall. Here the flow regime is observed as exiting at discrete points of the fracture as non-uniform separate rivulets or droplets.

If a fairly basic test such as this, aiming to directly mimic the smooth parallel plates model, cannot duplicate the basic assumptions of the cubic law, its use in numerical models should also be queried.

7.3. Lessons Learnt and Future Research Opportunities

In aiming to understand discreet fracture flow at partial saturation, it became increasingly evident that a more fundamental knowledge gap exists in the understanding of not how *much* water flows through fractures, but rather how water flows through fractures *per se*. Using black box model approaches, bulk flow can generally be estimated with a fair amount of confidence. The problem faced relates to how water is transferred through individual fractures. In this regard, this research has proved, for instance, that:

- Saturated sheetflow is not likely achieved, especially in non-horizontal fractures, resulting in failure of the cubic law .
- Preferential flow still occupies the vast minority of cross-sectional area in a vertical fracture, even if the water supply implies that it should achieve near-saturation.
- Movement of water through the fractured vadose zone becomes a matter of the continuity principle, whereby water should theoretically be transported downward at significantly higher flow rates given the very low degree of water saturation.
- How we aim to quantify discreet fracture flow, notably at sub-saturation, is implicitly inaccurate as is evident by even this study's aims to qualify rather than quantify this flow regime.
- Even an improved qualitative understanding in sub-saturated fracture flow improves the modelling input where presently we rely on quantitative estimates, which proves to be very inaccurate.

These findings need to be validated against similar tests conducted on field discontinuities. This can be done both in the laboratory on small-scale fractures to observe flow regimes on natural rock surface. Further validation could also be quantified *in situ* via field testing techniques, such as comparing results from Lugeon tests to that of optical and acoustic televiewers down boreholes. A comparison would be required to identify likelihood of adhesion to discontinuity surface may result in significant lateral flow as water moves into near-horizontal discontinuities due to adhesive forces exceeding cohesive forces.

Results presented in this report show that similar flow regimes described in literature were observed at both 1G and at increased gravitational acceleration (20G), which proves that the

geotechnical centrifuge may indeed be a valid method in answering practical problems associated with variably saturated flow. In order to further validate centrifuge modelling, these fundamental conceptual models should be compared to results from an exact full-scale model. If the same flow regimes are observed for full-scale versions of these horizontal and vertical fracture tests, then centrifuge modelling is indeed a valid tool to quantify variably saturated fracture flow.

The present research has underlined the existing issues with using the cubic law to quantify flow through rock fractures. Until a reasonable estimation of flow through rock fractures of variable geometry (viz. joint descriptors) can be deduced, no correlation will exist between joint parameters and flow.

The relevance of this fundamental hydrogeological question – i.e. how water moves through discreet fractures at partial saturation – is understated. Accuracy of recharge estimation and contaminant transport, for instance, rely on accurate estimations of the vadose zone as a whole. Travel times and flow rates become functions of intricate flow regimes at partial saturation that allows for significant changes in these parameters. Additionally, it cannot be assumed that water (and associated contaminants) will take the assumed gravitational route of least effort, and modelling of when and where water will reach the phreatic surface presently are guesses at best.

The implications and applications to dewatering and stabilisation through the reduction of excess pore water pressures furthermore become evident. The conventional approach of water exerting isotropic pressures may be proven incorrect, as saturation is highly anisotropic and not uniform.

Inevitably, reasonable understanding of flow through fractured media will contribute to extensive applications, including shallow and deep mining, contamination studies for landfills, dewatering and drainage practices, safe construction and better recharge estimation.

8. REFERENCES

Aydin, A. (2001). Fracture void structure: implications for flow, transport and deformation. Environmental Geology. **40**(6):672-677.

Bear, J. (1972). Dynamics of Fluids in Porous Media. Elsevier. New York

Bear J (1993) Modeling flow and contaminant transport in frac- tured rocks, in Flow and Contaminant Transport in Fractured Rocks (eds Bear J, Tsang CF, de Marsily G), Academic Press, San Diego, pp. 1–36.

Bell, F. G. (2004). Engineering geology. 1st ed. Oxford: Butterworth-Heinemann.

Berkowitz, B. (2002). Characterizing flow and transport in fractured geological media: a review. Advances in Water Research. **25**:816.884.

Bieniawski, Z. T. (1989). Engineering rock mass classifications. John Wiley & Sons Inc.

Brady, B. H. G. and Brown, E. T. (2005). Rock mechanics. 1st ed. Dordrecht: Kluwer Academic

Butterfield, R., (2000). Scale-modelling of fluid flow in geotechnical centrifuges. Soils and foundations, 40(6), pp 39-45.

Culligan-Hensley, P.J., & Savvidou, C., (1995). Chapter 8 - Environmental geomechanics and transport processes IN Taylor, R. E. (Ed.). Geotechnical centrifuge technology. CRC Press.

Davies, G. (2006). Olifants River Water Resources Development Project: De Hoop Dam: Engineering geological report for design, Volume 1: Text, Volume 2: Figures, and Volume 3: Appendices 1 to 3. Report Ref. No. 2006-0187, dated July 2006.

Davies, G. (2007). Olifants River Water Resources Development Project: De Hoop Dam: Proposed Quarry Sites. Second engineering geological materials report, Volume 1: Report text and Appendices, Volume 2: Figures. Report Ref. No. 2006-0195 (REV 01), dated November 2007. Elsevier Scientific.

De Marsily, G. (1986). Quantitative Hydrogeology. Academic. San Diego, California.

Dippenaar, M. A. and Van Rooy, J. L. (2015; in print). Variably saturated flow in single rough discontinuities: a review. International Journal of Rock Mechanics and Mining Sciences. (in print).

Dippenaar, M. A., Van Rooy, J. L., Breedt, N., Huisamen, A., Muravha, S. E., Mahlangu, S. and Mulders, J. A. (2014). Vadose zone hydrology: concepts and techniques. WRC Report No. TT 584/13. Water Research Commission. Pretoria.

Doe, T.W., (2001). What do drops do? Surface wetting and network geometry effects on vadose-zone fracture flow *in* Conceptual Models of Flow and Transport in the Fractured Vadose zone, pp 243-270.

Dragila, M.I., & Weisbrod, N., (2003). Parameters affecting maximum fluid transport in large aperture fractures. *Advances in Water Resources*, 26(12), pp 1219-1228.

Ghezzehei, T.A., (2004). Constraints for flow regimes on smooth fracture surfaces. Water resources research, *40*(11).

Gimenes, E. and Fernandez, G. (2006). Hydromechanical analysis of flow behavior in concrete gravity dam foundations. Canadian Geotechnical Journal, 43(3), pp.244--259.

GonzaÌlez de Vallejo, L. I. and Ferrer, M. (2011). Geological engineering. 1st ed. Leiden, The Netherlands: CRC Press/Balkema.

Gudmundsson, A., Glesdal, O., Brenner, S. L. and Fjeldskaar, I. (2003) Effects of linking up of discontinuities on fracture growth and groundwater transport. Hydrogeology Journal. 11:84-99.

Gurocak, Z. and Alemdag, S. (2012). Assessment of permeability and injection depth at the Atasu dam site (Turkey) based on experimental and numerical analyses. Bulletin of Engineering Geology and the Environment, 71(2), pp.221--229.

Habibi, V. (2013). Evaluate the permeability Dam site Jamishan with Emphasis on engineering geology. In: International Symposium on Advances in Science and Technology. Tehran: Islamic Azad University, pp.1-2.

Hamm, S., Kim, M., Cheong, J., Kim, J., Son, M. and Kim, T. (2007). Relationship between hydraulic conductivity and fracture properties estimated from packer tests and borehole data in a fractured granite. Engineering Geology, 92(1), pp.73--87.

Hoek, E. and Bray, J. (1977). Rock slope engineering. 2nd Ed (revised). The Institution of Mining and Metallurgy. London.

Hudson, J. A. and Harrison, J. P. (2000). Engineering rock mechanics. 1st ed. Oxford: Pergamon.

Hsieh, P.A., Bahr, J.M., Doe, T.W., Flint, A.L., Gee, G., Gelhar, L.W., Solomon, D.K., van Genuchten, M., Wheatcrsaft, S.W., (2001). Panel Report *in* Conceptual Models of Flow and Transport in the Fractured Vadose Zone. pp 9- 44

Indraratna, B. and Ranjith, P. (2001). Hydromechanical aspects and unsaturated flow in jointed rock. A.A. Balkema Publishers. Lisse.

Jacobsz, S. W. (2013). Centrifuge modelling of a soil nail retaining wall. Journal of the South African Institution of Civil Engineering, 55(1), 85-93.

Jaeger, J. C, Cook, N. G. W. and Zimmerman, R. W. (2007). Fundamentals of rock mechanics. 4th ed. Oxford: Blackwell Publishing Ltd.

Kordilla, J., Tartakovsky, A.M. and Geyer, T., (2013). A smoothed particle hydrodynamics model for droplet and film flow on smooth and rough fracture surfaces. Advances in Water Resources, 59, pp.1-14.

Kumar, P. R., (2007). Scaling laws and experimental modelling of contaminant transport mechanism through soils in a geotechnical centrifuge. Geotechnical and Geological Engineering, 25(5), 581-590.

Laut, P. (1975). Application of centrifugal model tests in connexion with studies of flow patterns of contaminated water in soil structures, Géotechnique, Vol. 25, No. 2, pp. 401-406.

Lee CH, Farmer I (1993) Fluid Flow in Discontinuous Rocks. Chapman and Hall, London, p. 169.

Lebeau, M. and Konrad, J.M., (2010). A new capillary and thin film flow model for predicting the hydraulic conductivity of unsaturated porous media. Water Resources Research, 46(12).

Liu, H., Wei, M., Rutqvist, J. (2013). Normal-stress dependence of fracture hydraulic properties including two-phase flow properties, Hydrogeology Journal. 21:371-382.

Look, B. (2007). Handbook of geotechnical investigation and design tables. Taylor & Francis. Leiden.

Mehreust, Y & Schmittbuhl, J., 2001. Geometrical heterogeneities and permeability anisotropy of rough fractures. J Geophys Res. 106(B2) (2001) 2089-102.

Neuman, S. P. (2005). Trends, prospects and challenges in quantifying flow and transport through fractured rocks. Hydrogeology Journal. 13:124-147.

Novakowski KS et al. (2007) Groundwater flow and solute trans- port in fractured media, in The Handbook of Groundwater Engineering, 2nd edition, (Delleur JW ed.), CRC Press, Boca Raton, pp. 20–1 to 20–43.

Or, D. and Tuller, M. (2003). Hydraulic conductivity of partially saturated fractured porous media: flow in a cross-section. Advances in Water Resources. 26:883-898.

Palström, A. and Stille, H. (2010). Rock Engineering. Thomas Telford Limited. Plymouth. 408pp.

Peters, A. and Durner, W., (2008). A simple model for describing hydraulic conductivity in unsaturated porous media accounting for film and capillary flow. Water resources research, 44(11).

Phillips, R., (1995). Chapter 3 - Centrifuge medelling: practical considerations In: Taylor, R. E. (Ed.). Geotechnical centrifuge technology. CRC Press.

Priest, S. D. (1993). Discontinuity analysis for rock engineering. 1st ed. London: Chapman & Hall.Publishers.

Sadeghiyeh, S. M, Hashemi, M. and Ajalloeian, R. (2013). Comparison of permeability and groutability of Ostur dam site rock mass for grout curtain design. Rock Mechanics and Rock Engineering, 46(2), pp.341--357.

Silberhorn-Hemminger, A., Süβ, M. and Helmig, R. (2005). Natural fractured porous systems. In: Dietrich, P., Helmig, R., Sauter, M., Hötzl, H., Köngeter, J., and Teutsch, G. (Eds.). Flow and transport in fractured porous media. Springer. Berlin. 16-24.

Singh, B. and Goel, R. K. (2011). Engineering rock mass classification. 1st ed. Waltham, MA: Butterworth-Heinemann.

Singhal, B. B. S. and Gapta, R. (2010). Applied hydrogeology of fractured rocks. 2nd ed. Dordrecht: Springer.

Sisavath, S., Al-Yaarubi, A., Pain, C. C. and Zimmerman, R. W. (2003). A simple model for deviations from the cubic law for a fracture undergoing dilation or closure. Pure Appl. Geophys. 160:1009-1022.

Su, G.W., Geller, J.T., Pruess, K., & Wen, F., (1999). Experimental studies of water seepage and intermittent flow in unsaturated, rough-walled fractures. Water resources research, 35(4), pp 1019-1037.

Taylor, R.N., (1995). Chapter 2 - Centrifuges in modeling: Principles and scale effects In: Taylor, R. E. (Ed.). Geotechnical centrifuge technology. CRC Press.

Thiel, K. (1989). Rock mechanics in hydroengineering. 1st ed. Amsterdam: Elsevier.

Thusyanthan, N. I., & Madabhushi, S. P. G. (2003). Scaling of seepage flow velocity in centrifuge models. CUED/D-SOILS/TR-326.

Tokunaga, T.K., & Wan, J., (1997). Water film flow along fracture surfaces of porous rock. Water Resources Research, 33(6), pp 1287-1295.

Tuller, M. and Or, D., (2002). Unsaturated hydraulic conductivity of structured porous media. Vadose Zone Journal, *1*(1), pp.14-37.

Turkmen, S., Tauga, H. and Ozguler, E. (2013). Effect of Construction Material on Dam Type Selection of the Buyuk Karacay Dam (Hatay, Turkey). Geotechnical and Geological Engineering, 31(4), pp.1137--1149.

Van der Merwe, (2013). De Hoop Dam. Geological Completion Report. Pretoria: Knight Piesold, pp.1-8.

Van Vuuren, L. (2008). Water key to wealth building in Limpopo. The Water Wheel, 7(4), p.28.

Wahlstrom, E. (1974). Dams, dam foundations and reservoir sites. 1st ed. Amsterdam:

Weiss, M., Rubin, Y., Adar, E. and Nativ, R. (2006). Fracture and bedding plane control on groundwater flow in a chalk aquitard. Hydrogeology Journal. **14**:1081-1093.

Witherspoon, P. A., Wang, J. S. Y., Iwai, K. and Gale, J. E. (1980). Validity of cubic Llaw for fluid flow in a deformable rock fracture. Water Resources Research. **16**(6):1016-1024.

Winter, J. (2010). An introduction to igneous and metamorphic petrology. 1st ed. New York: Prentice Hall.

Wyllie, D. C. (1992). Foundations on rock. 1st ed. London: E. & F.N. Spon.

Zhang, Z.F., (2011). Soil water retention and relative permeability for conditions from oven-dry to full saturation. Vadose Zone Journal, 10(4), pp.1299-1308.

Zimmerman, R. W. and Bodvarsson, G .S. (1996). Hydraulic conductivity of rock fractures. Transport in Porous Meida. 23:1-30.

Appendix A.   CASE STUDY: DE HOOP DAM

A.1.   Background

The De Hoop Dam was constructed as bulk water supply to the rapidly expanding Sekhukhune district (situated on the eastern limb of the Bushveld Igneous Complex). The dam supplies water for infrastructure, mining activities as well as 800 000 people living on the Nebo Plateau. The construction of the dam is part of the second phase of the Olifants River Water Resources Development Project (ORWRDP) conducted by the Department of Water Affairs and Forestry (DWAF) (Davis, 2006; Van Vuuren, 2008).

The first reconnaissance level investigations were done in 1983 by BKS, followed by pre-feasibility investigations in the mid 1980s by the Council for Geoscience (CGS). Additional investigations were carried out in the late 1990s to present a detailed feasibility report in 2001. Most of the design investigations were done between 1999 and 2008, and the reports for the dam design and quarry investigations were documented in July 2006 and June 2007 (Davis, 2006; Van der Merwe, 2013).

The De Hoop Dam was constructed as a Roller Compacted Concrete (RCC) dam with a length of 1 016 m and a maximum height of 81 m. The dam can potentially hold a bulk water reserve volume of 346 x 10^6 m^3.

A.2.   Study area

The study area is located on the farm De Hoop 886 KS, approximately 27 km southwest of Steelpoort and 26 km north of Roossenekal in Limpopo, as shown in Figure A-1. The De Hoop Dam is situated in the Steelpoort valley and is constructed on the Steelpoort River. The Steelpoort River flows in a northerly direction and feeds directly into the dam with added inflow from the Klip River located roughly 500 m upstream of the dam wall (Van der Merwe, 2013).

The dam wall is divided into three zones, namely the right flank, the river section or spillway, and the left flank. These zones are then subdivided into 10 m foundation blocks; each block being allocated a specific number depending on the location along the dam centreline. Even numbers were given to the left flank blocks (eastern side of dam wall) and odd numbers for the blocks of the right flank (western side of dam wall). The centre of the spillway acts as the starting point (Block 1) from which the numbering is initiated. The Chainage (Ch) is used to indicate the length of the dam wall in metres on the reference line, from a fixed point "A", as shown in Figure A-2.

Figure A-1. Location of the De Hoop Dam site and the dam wall (© Google Earth 2015).

The Chainage starts (Ch 0) in the right flank of the dam on the most easterly point A and is measured on the dam reference line to the western point B of the dam wall (Ch 1016). Table A-1 provides a summary of the Chainage, amount of blocks and the block numbers for the 3 zones of the dam wall.

Table A-1. Zoning of the dam wall (Van der Merwe, 2013).

Zone	Chainage (Ch)	Blocks	Number of blocks in each group
Right flank	0 -110	13-33	11
River section	110 - 220	2-10 and 1-11	11
Left flank	220 - 1016	12-170	79

The portion chosen for the experimental site is located on the left flank, from Block 88 (Ch 600) to Block 118 (Ch 760) of the dam wall. This area was specifically chosen due to seepage that occurred after the completion of the dam wall, as well as anomalously high Lugeon values that were obtained from grout curtain borehole packer testing. This leads to a total of 16 blocks, with a total length of 160 m that are investigated, as shown in Figure A-2.
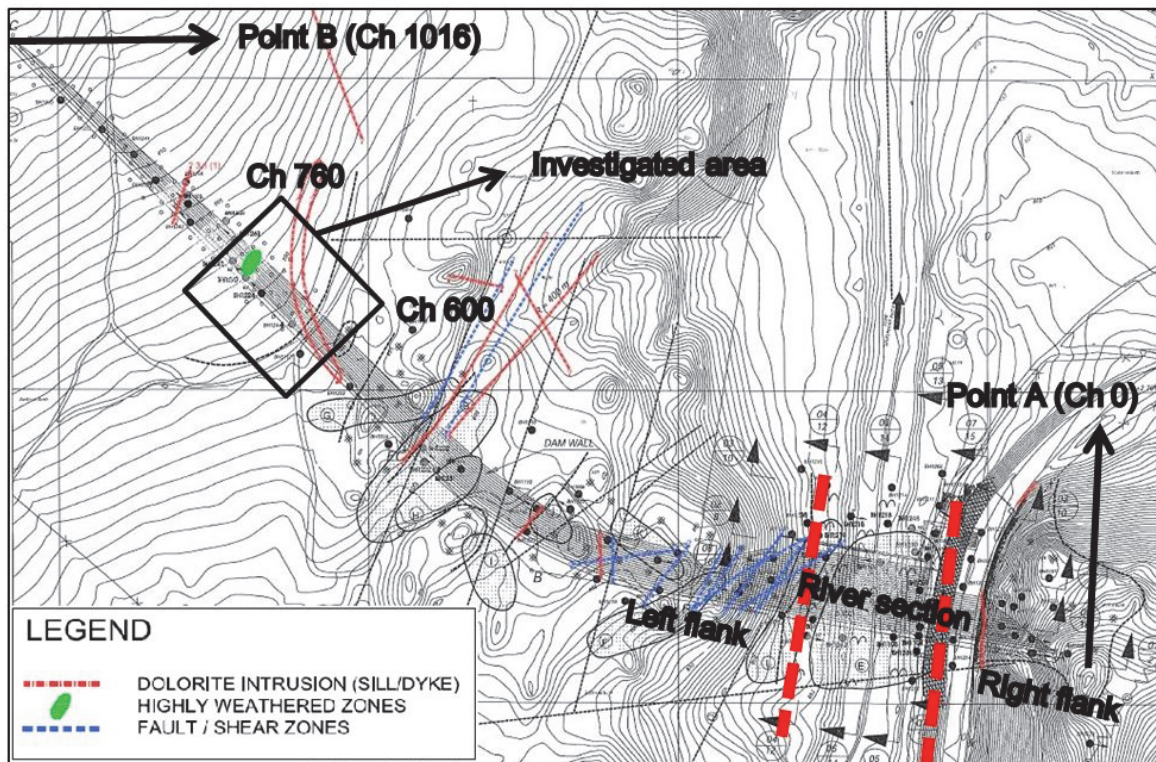
Figure A-2.   Plan view of the De Hoop Dam and the area investigated (modified from Van der Merwe, 2013).

A.2.1   Topography and drainage

The Steelpoort valley has a gradual continuous dip from the western escarpment towards the river section with the eastern (right) flank consisting of variable koppies and steeply sloped valleys; this could be due to various intrusions within the host rock that is more resistant to weathering.

On the dam centreline the left flank ranges in altitude from approximately 922 m above mean sea level (mamsl) at Ch 1016, towards 846 mamsl at the centre of the river section. The right flank has a steep slope from the river bed inclining towards the Mampurukop koppie over a short distance of approximately 150 m, towards Ch 33 with altitude roughly at 906 mamsl (Figure A-3).
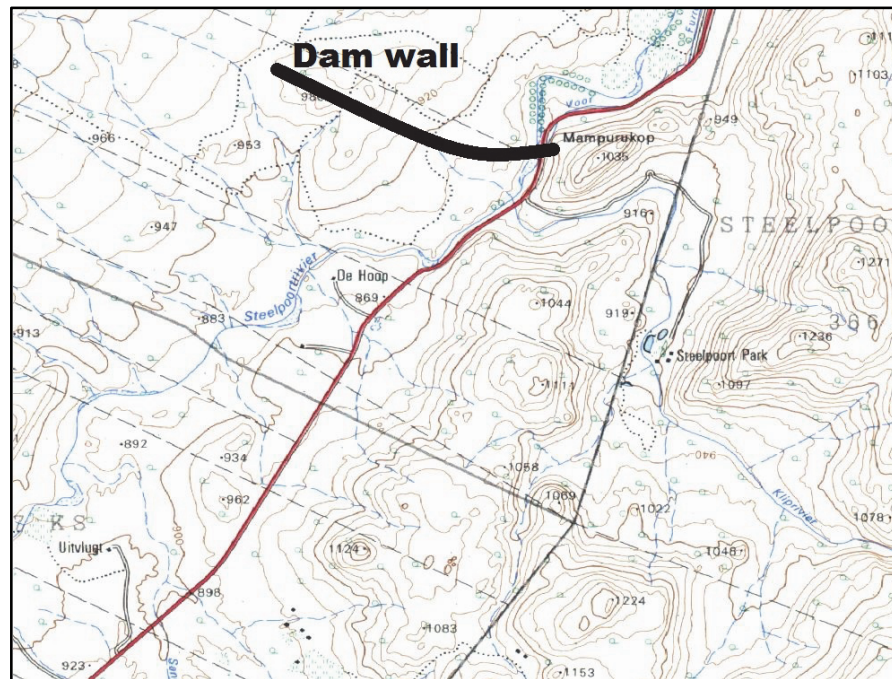
Figure A-3.   **Topographical map of the dam wall (modified from Davies, 2007).**

A.2.2   Geology

According to the 1:250 000 geological sheet, 2428 Nylstroom, the dam site is underlain by layered intrusive igneous rocks of the Rustenburg Layered Suite (RLS) in the eastern limb of the Bushveld Igneous Complex (Figure A-4.). The dam basin is generally underlain by magnetite gabbro-norite of the Upper Zone of the RLS, while the dam wall is mostly underlain by fairly uniform gabbro rocks of the Main Zone in the RLS. The layered intrusive igneous rocks of the RLS dip obliquely in a north-westerly direction on the site, with a gradual angle of $8°$ to $13°$ (Davis, 2006).

The major northeast-striking Steelpoort Fault is located roughly 600 m west of the left flank, as shown in Figure A-4. According to Davis (2006), the fault has a strike length of more than 100 km, with a maximum measured displacement of 750 m near the dam site. Davis (2006) suggests that the Steelpoort Fault is no longer active and will not cause any future disturbances on the drainage patterns of the dam site. According to Cawthorne et al. (2006), the Steelpoort Fault was active during the emplacement of the Nebo Granite at 2054±2 Ma.

Magnetite bands in the Upper Zone intersect the foundation geology, as well as the dam basin. This economically important magnetite band was first mined out before the construction of the dam commenced (Davis, 2006).
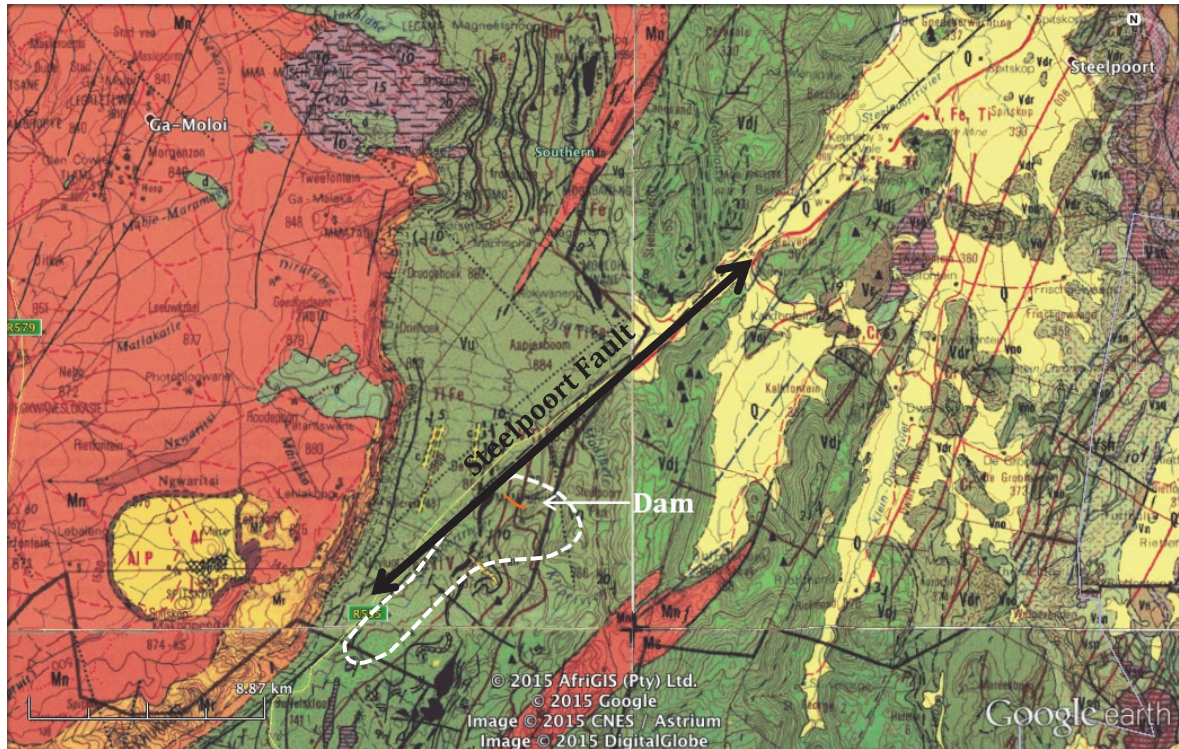
Figure A-4.   Regional geology of the De Hoop Dam (Government Printer 1986).

According to the as-built foundation maps of the De Hoop Dam the investigated area between Block 88 and 118, is highly jointed. These joints have prominent north-west and north-east strike directions with dips ranging from 15° to 87°. This area also contains numerous minor faults, pegmatite veins, dolerite intrusions and anorthosite zones. These structural features are considered to be related to the Steelpoort Fault (Van der Merwe, 2013). The pegmatite veins have a prominent strike in a northern direction generally dipping steeply at angles between 55° and 80°. They also vary in thicknesses from 20 to 200 mm, and are filled with loose packed pegmatite gravel.

Minor faults generally strike in a north to north-east direction, with a small number of the small- scale minor faults striking in an east to west direction. Some of these minor faults may contain sandy clay infillings, but the fault aperture thicknesses are generally between 2 to 50 mm. These minor faults have varying dip angles between 44° to 80°

Dolerite intrusions are also encountered in this area with widths varying between 0.4 to 4 m. Some poorer geological zones are associated with these dolerite intrusions and are related to the gabbro/dolerite contact zones. The few anorthosite zones are generally closely jointed near fault contacts and moderately weathered.

A.3.   Methodology

The Department of Water Affairs (now the Department of Water and Sanitation) appointed De Hoop Dam Consultants (DHDC) to supervise the construction of the De Hoop Dam. Knight Piesold Consulting (KPC), on behalf of DHDC, supplied the following data:

- Discontinuity parameter data and stereographic plots from the dam foundation; and
- Permeability data from packer tests as conducted prior to and during grouting.

A.3.1   Geological foundation mapping

Geological mapping of each block on the dam foundation was conducted once the block was cleaned and ready for concrete placement. All the major geological features were recorded together with their orientation and were then plotted on graph paper. Digital photographs of each foundation block were taken from different angles, both in the upstream and downstream direction. In the case of specific or significant features more detailed and close-up photographs were taken. Mapped display sheets of each block were generated that contain the geological foundation mapping, stereo plots, typical foundation photographs and rock mass descriptions (Van der Merwe, 2013).

The joint line surveys were conducted in two directions namely parallel to the dam centreline (10 m) and a second survey perpendicular to the centreline. The perpendicular surveys were conducted starting from the upstream side. The length of these surveys varies due to the width of the foundation block for the dam wall, but range from 15 to 65 m. Larger blocks, such as the outlet and the spillway may contain up to three to four line surveys. Most of the perpendicular surveys were conducted on the centre of the foundation block or on the block interfaces (Van der Merwe, 2013).

The discontinuity parameters were recorded along a 50 m measuring tape placed on the exposed foundation and the following parameters were recorded for each intersected discontinuity: distance along the tape, rock type, rock description, orientation (dip and dip direction), continuity, joint surface roughness, gouge or filling and water (seepage).

A total of 1151 discontinuity entries were obtained from Block 88 to 118.

The stereographic projections of each block orientation were created using Rocscience DIPS V5.0®. Stereo plots of both joint line surveys in each block were created, with a third being the combined stereo plot of the two surveys (Van der Merwe, 2013).

Two as-built foundation maps, 18 block foundation mapping sheets and three grouting as-built maps were also obtained. The 18 as-built foundation mapping sheets contain detailed geological mapping of the most prominent geological features. These sheets also provide information on

the orientation of the discontinuities found within the individual blocks, along with a short description of the rock mass. An example of one of the sheets is shown in Figure A-5.

Figure A-5. Example of an as-built foundation mapping sheet for a 10 m foundation block (Van der Merwe, 2013).

A.3.2 Packer tests

The packer tests were conducted in three stages. These tests were conducted using a single, downhole packer for each stage and comprised of 3 x 5 min steps at a constant pressure of 150 kPa. The Lugeon values and grout takes were obtained during the construction phase of the dam wall.

A.3.3 Interpretation

To find a correlation and/or relationship between discontinuity parameters and Lugeon values, statistical and comparative analyses were conducted. JLS data were captured into MS Excel © to facilitate statistical analysis as shown in Figure A-6.

	A	B	C	D	E	F	G	H	I	J	K	L	M	N	O	P	Q	R	S	T
1	Dip	Dip direction	Block number	Ref line	Distance	Type	Hardness	Weathering	Structure	Dip Length	Dip Ends	Strike Length	Strike Ends	Roughness	Discontinuity hardness	Amplitude	Base	Aperture	Fill type	Fill consistency
2	13	291	88	Parallel	0.2	G	R4	S-U	T	1	1	0.7	2	10		40	0.6	0		
3	13	291	88	Parallel	0.6	G	R4	S-U	T	1	1	0.7	2	10		40	0.6	0		
4	88	185	88	Parallel	1	G	R4	S-U	T	0.1	0	0.6	2	11		10	0.2	0	Ss	
5	88	185	88	Parallel	1.3	G	R4	S-U	T	0.1	0	0.6	2	11		10	0.2	0	Ss	
6	86	54	88	Parallel	1.8	G	R4	S-U	T	0.05	0	0.7	2	10				0	Sd	
7	74	176	88	Parallel	2.3	G	R4	S-U	T	0.05	0	0.9	2	10				0	Sd	
8	74	176	88	Parallel	2.5	G	R4	S-U	T	0.05	0	0.9	2	10				0	Sd	
9	20	242	88	Parallel	3	G	R4	S-U	T	1.7	1	2.1	2	13		40	0.9	0	Sd	
10	87	327	88	Parallel	4.4	G	R4	S-U	T	0.05	0	1.5	2	12				1	Wr	
11	87	327	88	Parallel	4.6	G	R4	S-U	T	0.05	0	1.5	2	12				1	Wr	
12	87	327	88	Parallel	5	G	R4	S-U	T	0.05	0	1.5	2	12				1	Wr	
13	20	245	88	Perpendicular	0	G	R4	S-U	T	2.5	1	2.4	2	12		20	0.4	5	Sd	
14	85	15	88	Perpendicular	1.3	G	R4	S-U	T	0.2	0	0.3	2	10				0	Sd	
15	25	355	88	Perpendicular	1.6	G	R4	S-U	T	0.7	1	0.7	2	12		30	0.5	0		
16	70	30	88	Perpendicular	2.1	G	R4	S-U	T	0.2	0	1	2	11				0	Sd	
17	60	232	88	Perpendicular	2.3	G	R4	S-U	T	0.1	0	0.4	2	10				0	Sd	
18	21	294	88	Perpendicular	2.7	G	R4	S-U	T	0.5	1	1.5	2	12		10	0.3	0	Sd	
19	76	193	88	Perpendicular	3.8	G	R4	S-U	T	0.1	0	0.2	2	10				0	Sd	
20	77	54	88	Perpendicular	4	G	R4	S	T	0.2	0	0.5	2	11				1	Sd/Ss	

Figure A-6.   Example of the final combined JLS data sheet.

The combined data sheet was used as the master file in the DIPS V5.0 program. The data were extracted statistically via queries and charts for analysis, and was also extracted via stereographic projections for correlation analysis. These methods are discussed in more detail in the sub-sections that follow.

The grouting as-built sheets were used to locate and identify high and low permeability zones of the different blocks, and these are presented in a summarised table. The distinction between low and high permeability was set at a Lugeon value of Lu = 5, where Lu < 5 being low and Lu > 5 being high. The geological foundation mapping as well as digital photographs was also consulted to identify possible geological significant features that may influence the characteristics and permeability of the rock mass. These significant features within the blocks were compared to their specific Lugeon values of the block to determine a possible correlation.

The large volume of JLS data entries were grouped into the three discontinuity types, viz. tension joints, fault fractures and stress-relief joints. Average values for each parameter that may influence the permeability of a rock mass were calculated for each discontinuity type. These parameter values were weighted against each other. The same statistical analysis was also conducted for the packer test data, whereby the low and high permeability blocks weighted against each other for all three discontinuity types.

Stereographic projections were used to establish possible correlations between the three discontinuity types, as well as between the high and low permeability blocks.

A.4. Numerical Model

A.4.1 Methodology

The as-built foundation maps of the exposed rock mass were used to model the pegmatite vein as it contained relatively detailed information on the geometry of the fracture, specifically regarding the strike and dip variations along its length within Block 108 and 110 (Figure A-7). A local coordinate system was established whereby x, y and z coordinates where approximated from the foundation map, and subsequently extrapolated over the 3D block. The x-axis of the coordinate system follows the reference line of the dam and starts at a chainage of 720 m, and ends at a chainage of 700 m. The y-axis starts at the reference line and is positive towards the downstream side and negative towards the upstream side of the reference line. The z-axis starts 10 m below the excavation depth and increases with depth. A maximum depth of 10 m was chosen as this was the depth to which the relief wells were drilled.

Figure A-7 outlines the process to determine the coordinates of the surface contact of the pegmatite vein. This entailed identifying a number of linear elements whereby the orientation of the pegmatite vein could be approximated. From this, five linear elements were identified and their orientation data are summarised in Table A-2.

Table A-2.   Orientation data for the modelled elements of the pegmatite vein.

Element	x-start	x-end	y-start	y-end	Strike*	Dip-start	Dip-end
1	15.08	14.43	0	5.36	173.06	66.8	35
2	14.43	10.16	5.36	13.40	152.03	35	55
3	10.16	8.18	13.40	21.15	165.68	55	28.33
4	17.06	15.08	-15.89	0	173.06	66.8	66.8
5	8.18	5.63	21.15	31.13	165.68	28.33	28.33

*Note: the strike is relative to the x-axis (0°)

Element 4 is an extrapolation upstream of element 1 save for the dip which is kept constant from its start as no data was available on its orientation. Similarly, element 5 is an extrapolation downstream of element 3 save for the dip which is kept constant from its start. The reason for including extrapolated elements was such that there is a region upstream (element 4) and downstream (element 5) of the dam wherefrom the hydraulic head can be calculated. These extrapolated elements extend 10 m to either side of the dam wall.
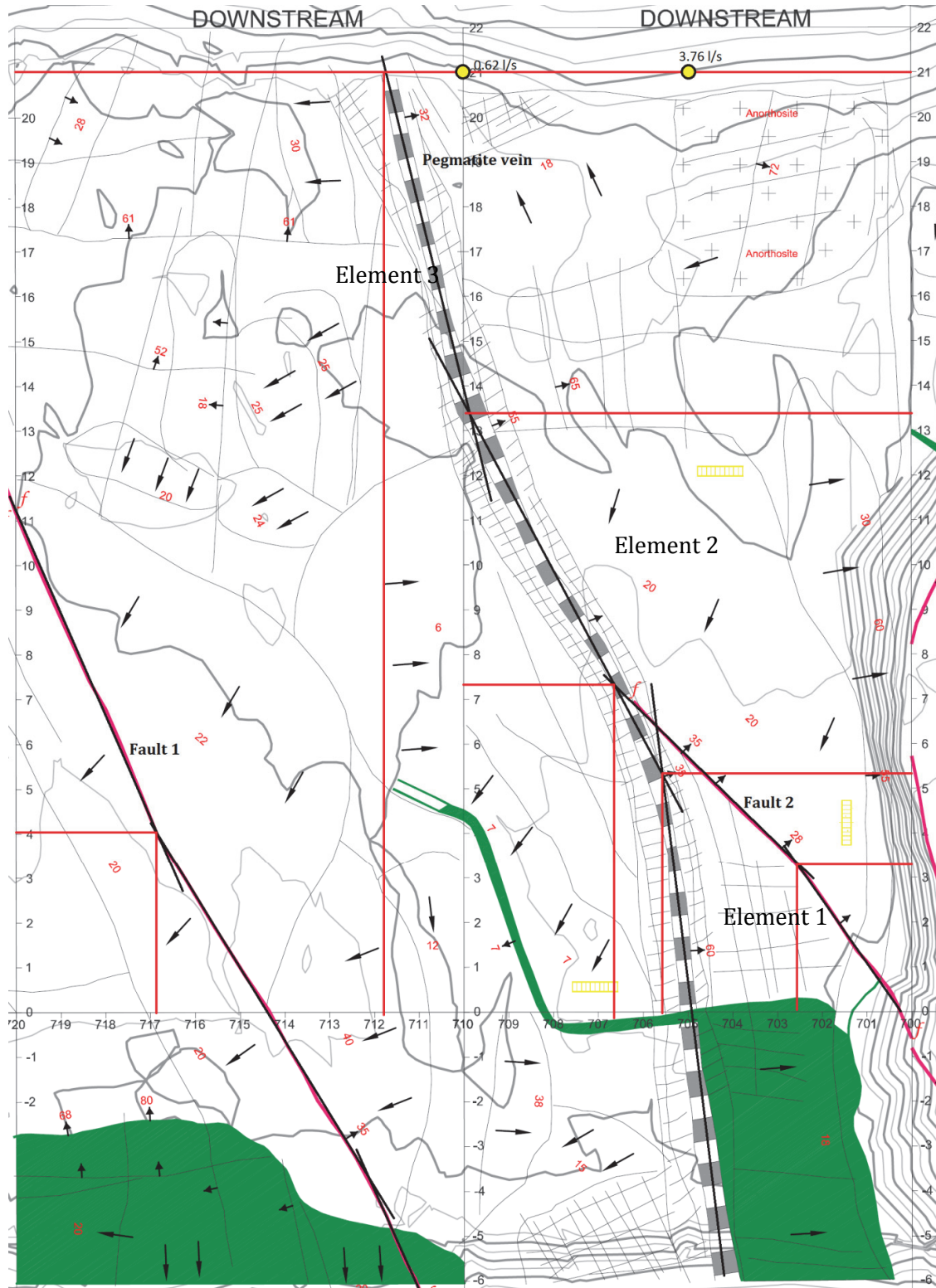
Figure A-7. As-built foundation map of block 108 (right) and 110 (left). The black lines represent the approximated strike of each element, and the dip directions are represented by the small arrows. Dip magnitude is given by the red numbers.

A.4.2 Mathematical modelling of the pegmatite vein

The pegmatite vein was mathematically modelled as a 2D plane in a 3D axis system. This was accomplished by initially creating a cell array of the appropriate dimensions (rows and columns) and subsequently calculating the coordinates for each cell based on its row and column position in the cell array. A cell scale of 10x10cm was chosen. Initially a linear element was modelled representing the surface profile of the pegmatite vein, whereby this constituted the first row of the plane. This was followed by approximating the dip over the length of each element and subsequently assigning coordinates to the rest of the cells in the array. As such the subsurface cells constituted of all the rows below the first, and are determined based on the assumption that the dip remains constant with depth. The resulting geometry of the Pegmatite vein is given in Figure A-8.
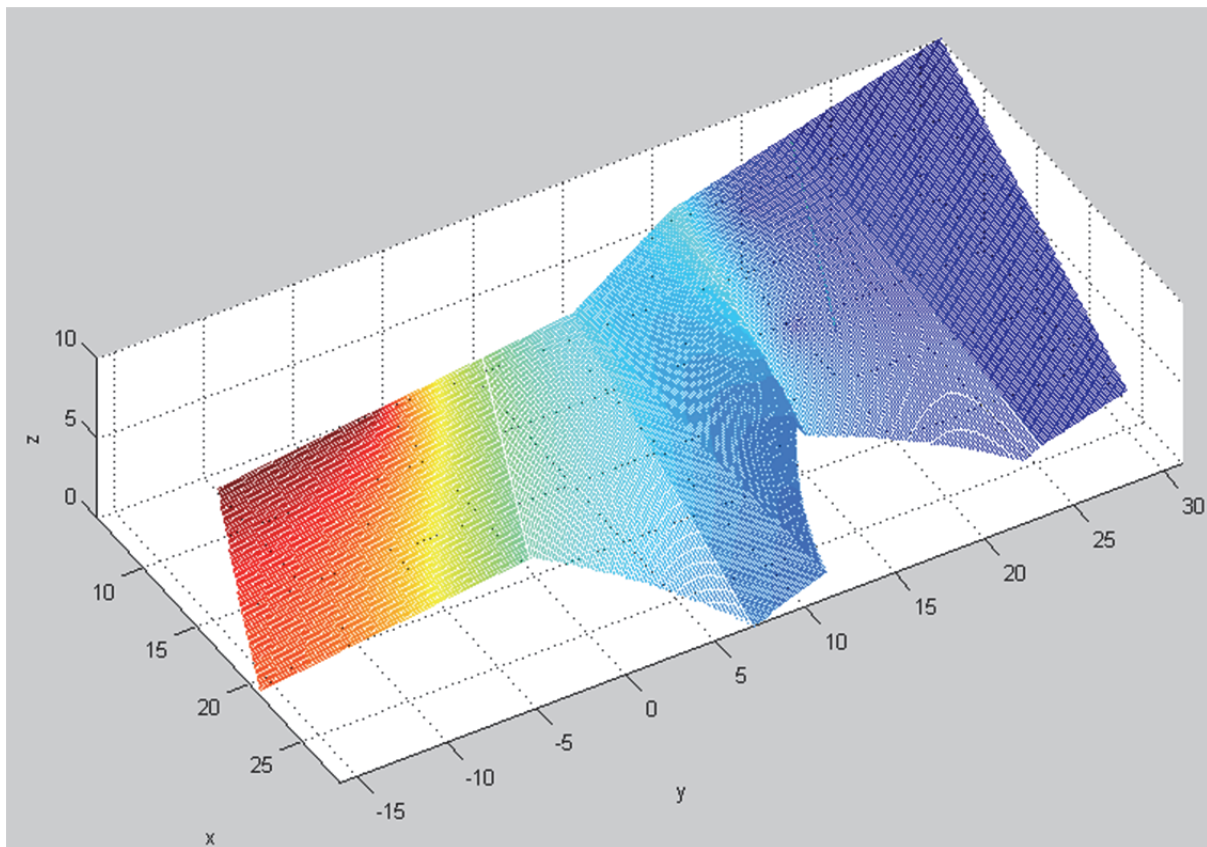

Figure A-8.   Geometrical representation of the modelled pegmatite vein across Blocks 108 and 110.

A.4.3 Adding and subtracting wedges

At the boundary between elements 1 & 2 and 2 & 3, the presence of a strike change resulted in either missing or excessive cells with depth. This is due to the fact that with a strike change, the adjacent columns, on the boundary of either element, move in different directions with depth, resulting in them moving progressively further away (in a wedge) from one another along their lengths. A missing wedge is obtained when the strike change is convex to the dip direction, and an excess wedge (cross-over) when concave to the dip direction. The missing wedge was

corrected by obtaining the coordinates of the cells on either boundary column, and extrapolating cells between them. The excess wedge required the finding of the intersection of the cross-over between the elements, and subsequent clearing of the cells between them.

A.4.4 Assigning other cell parameters

The advantage of using cell arrays is that each cell of the array has its own array of cells within it, wherein data can be stored relevant to that specific cell at a specific index (position in the array). The cell parameters are listed below with their respective index position given in brackets (index):

- X (3),Y (4) and Z (5) coordinates
- Degree of saturation (1) = water volume/cell volume
- Hydraulic head (2)
- Intersections with cells of other planes (6-11)
- Cell volume (12) = aperture*cell area
- Water volume in the cell (13)
- Aperture (14)
- Hydraulic conductivity (15)
- Fluid pressure (20).

The aperture was taken from the results of the joint line surveys conducted along Block 108, given as 29 mm. The first survey was conducted parallel to the reference line; however 3 m upstream of it. The second survey was conducted perpendicular to the reference line while starting at a chainage of 705 m at the reference line and ending 19.4 m downstream of the reference line. Both surveys identified the pegmatite vein at the approximate locations of the foundation map, and classified it as a fault zone with an aperture of 29 mm and a hard weathered rock infilling. However, the as-built foundation map of Block 108 described the infilling as varying between a sandy clay and highly weathered rock. As such, a variety of hydraulic conductivity values would need to be assumed and modelled for.

A.4.5 Determining the hydraulic conductivity

The hydraulic conductivity for a clean (no infill) fracture was calculated from the intrinsic permeability and the flow properties of water. The intrinsic permeability (k) of a clean fracture was determined from the cubic law with the aperture (b) through Equation A.1 (e.g. de Marsily, 1986).

$$k = \frac{b^2}{12} = \frac{0.029^2}{12} = 7.0083 \times 10^{-5} \text{ m}^2 \qquad \text{(A.1.)}$$

And subsequently the hydraulic conductivity (K) was determined from Equation A.2.

$$K = k\frac{\rho g}{\mu} = (7.0083 \times 10^{-5})\frac{1000 \times 9.81}{0.0014} = 491.08 \text{ m/s} \qquad \text{(A.2.)}$$

However, due to the sandy clay and highly weathered rock infilling, the hydraulic conductivity of the infilled fracture will be that of the infill material. The hydraulic conductivity ranges for the two infill materials were taken from Dippenaar et al. (2014) as:

1. Unfissured clay: $1.00 \times 10^{-9} < K < 1.00 \times 10^{-6} \, m/s$

2. Fractured crystalline rock: $1.00 \times 10^{-8} < K < 1.00 \times 10^{-3} \, m/s$

As such, the hydraulic conductivity range for the infill material was taken as 1.00×10^{-3} m/s for the upper limit, and 1.00×10^{-9} m/s for the lower limit.

The flow through the pegmatite vein was modelled for all three hydraulic conductivity values, being the clean fracture (491.08 m/s) and the range limits for the infill (1.00×10^{-3} and 1.00×10^{-9} m/s).

A.4.6   Determining the hydraulic head distribution

In order to model the flow through the pegmatite vein, it is required to know the hydraulic gradient under which the flow occurs. A confined flow net method was utilised to approximate the hydraulic head distribution throughout the plane. Due to the fact that the aquifer properties were extrapolated over its length, the plane was assumed as both homogenous and isotropic. As such, calculating the head distribution is fairly straightforward and can be conducted through Smyrell's method.

From Darcy's law, the specific discharges in the three directions are as per Equation A.3.

$$\text{v-}_x = -\frac{K \, \partial h}{\partial x}; \; \text{v-}_y = -\frac{K \, \partial h}{\partial y}; \; \text{v-}_z = -\frac{K \, \partial h}{\partial z} \qquad \text{(A.3.)}$$

Considering an infinitesimally small element through which steady state flow occurs; if the element experiences no change in total volume or water volume, and water is considered incompressible, then the water flowing into the element should be equal to that flowing out (Knappett and Craig, 2012). This is known as the continuity equation and can be characterised by Equation A.4.

$$\frac{\partial v_x}{\partial x} + \frac{\partial v_y}{\partial y} + \frac{\partial v_z}{\partial z} = 0 \qquad \text{(A.4.)}$$

By combining the above two equations for an isotropic (for K) medium; the second order partial derivative gives the Laplace equation, Equation A.5.

$$\frac{\partial^2 h}{\partial x^2} + \frac{\partial^2 h}{\partial y^2} + \frac{\partial^2 h}{\partial z^2} = 0 \qquad \text{(A.5.)}$$

Since only 2D flow is under consideration, the Laplace equation can be simplified to Eq A.6.

$$\frac{\partial^2 h}{\partial x^2} + \frac{\partial^2 h}{\partial y^2} = 0 \qquad \text{(A.6.)}$$

The plane is modelled with a regularly spaced grid, taking a finite difference approach, resulting in: $\Delta x = \Delta y$. As such, for a cell in question with an index of i and j (Akhter et al., 2006), Equation A.7-A.8. hold and can be substituting into the Laplace equation as per Equation A.9.

$$\frac{\partial^2 h}{\partial x^2} \approx \frac{h_{i-1,j} - 2h_{i,j} + h_{i+1,j}}{(\Delta x)^2} \tag{A.7.}$$

$$\frac{\partial^2 h}{\partial y^2} \approx \frac{h_{i,j-1} - 2h_{i,j} + h_{i,j+1}}{(\Delta y)^2} \tag{A.8.}$$

$$h_{i-1,j} + h_{i+1,j} + h_{i,j-1} + h_{i,j+1} - 4h_{i,j} = 0 \tag{A.9.}$$

Thus the hydraulic head at a point can be calculated from Equation A.10 (Knappett and Craig, 2012; Akhter et al., 2006; Williams et al,, 1993).

$$h_{i,j} = \frac{h_{i-1,j} + h_{i+1,j} + h_{i,j-1} + h_{i,j+1}}{4} \tag{A.10.}$$

This can be seen as the average of the cell above ($h_{i-1,j}$), below ($h_{i+1,j}$), to the right ($h_{i,j+1}$) and to the left ($h_{i,j-1}$) of the cell in question. This type of equation is known as a circular loop, as each cells value is dependent on the other cells in the array. However, if this is calculated iteratively with a number of boundary conditions set, the head distribution can be calculated such that increasing the number of iterations produces a better distribution. It is recommended by Williams et al. (1993) that the sequence should be iterated through until the tolerance (difference between old and new value) be within 0.001 m for all cells. Iterating past this tolerance would yield an insignificant improvement in accuracy.

The boundary conditions were set as:

- Upstream surface boundary (first row of element 4)
- Downstream surface boundary (first row of element 5)
- Relief wells.

The hydraulic head at the upstream boundary was taken as the height of the water level at that location being 25 m above ground level. The head for the downstream side and the relief wells was taken as the surface level at 0 m.

Due to the presence of no-flow boundaries in the modelled plane, a number of alternative head calculation equations were included into the iterative process, as shown below.

Head calculation equations for the various boundary conditions, modified from Williams et al,

(1993).

The common conditions are tabulated below:

Boundary condition	Graphical Depiction			Formula
None		Up		h
	Left	h	Right	$= \dfrac{Up + Down + Right + Left}{4}$
		Down		
Upper		Up		$h = \dfrac{(2Down) + Right + Left}{4}$
	Left	h	Right	
		Down		
Lower		Up		$h = \dfrac{(2Up) + Right + Left}{4}$
	Left	h	Right	
		Down		
Right		Up		$h = \dfrac{Up + Down + (2Left)}{4}$
	Left	h	Right	
		Down		
Left		Up		$h = \dfrac{Up + Down + (2Right)}{4}$
	Left	h	Right	
		Down		
Upper-Right		Up		$h = \dfrac{Down + Left}{2}$
	Left	h	Right	
		Down		

Upper-Left		Up		$h = \dfrac{Down + Right}{2}$
	Left	h	Right	
		Down		
Lower-Right		Up		$h = \dfrac{Up + Left}{2}$
	Left	h	Right	
		Down		
Lower-Left		Up		$h = \dfrac{Up + Right}{2}$
	Left	h	Right	
		Down		

The uncommon conditions are tabulated below:

Boundary condition	Graphical Depiction	Formula
Upper-Lower	*Up* / *Left* *h* *Right* / *Down*	$h = \dfrac{Right + Left}{2}$
Right-Left	*Up* / *Left* *h* *Right* / *Down*	$h = \dfrac{Up + Down}{4}$
Upper-Lower-Right	*Up* / *Left* *h* *Right* / *Down*	$h = Down$
Upper-Lower-Left	*Up* / *Left* *h* *Right* / *Down*	$h = Right$
Upper-Right-Left	*Up* / *Left* *h* *Right* / *Down*	$h = Left$
Lower-Right-Left	*Up* / *Left* *h* *Right* / *Down*	$h = Up$

Conversion						
	Up			$h_{i-1,j}$	
Left	*h*	*Right*	$h_{i,j-1}$	$h_{i,j}$	$h_{i,j+1}$
	Down			$h_{i+1,j}$	

	Up	
Left	*h*	*Right*
	Down	

A.4.7 Calculating the flow

Due to the high seepage occurring through the relief wells, it was assumed that saturated flow was occurring trough the pegmatite vein at the time of measurement. Furthermore, Darcy's law was assumed to apply, and as such, the flow velocity can be determined from Equation A.11.

$$v = K \frac{\Delta h}{0.1} \qquad\qquad (A.11.)$$

The value 0.1 is the cell width in meters and accounts for the distance over which the head difference dissipates. Due to the evenly spaced cells, the distance over which the head dissipates is constant. Since each cell has a hydraulic head and hydraulic conductivity already assigned, the velocity of flow can be determined. This velocity is then assumed to apply for all the water within the cell.

As such, the 'flow time' can be determined, which can be defined as the time it would take the water to flow across the full length of the cell (0.1 m). This time along with the 'step rate' (time between each step) and the water volume of the cell (V_w) can be used approximate the volume of flow through Equation A.12.

$$flow = V_w \frac{flow\ time}{step\ rate} \qquad\qquad (A.12.)$$

A smaller step rate reduces the volume of flow per step and therefore produces results of higher resolution. However, this can significantly increase the time required to run the function as the number of iterations required for the same volume of flow is inversely proportional to the step

rate. The step rate should never exceed the flow time, as this would result in a flow volume that exceeds the quantity of water in the cell. As such, a low step rate utilised and taken as: step rate $= 1 \times 10^{-7}$s accounting for the high hydraulic conductivity for the clean fracture.

The flow direction is determined from the distribution of hydraulic head values of the surrounding cells. The cell of lowest head is deemed the cell most likely to receive flow, and is thus the target cell. If the target cells head is less than that of the source cell, then the flow function is initiated. The quantity of flow is reduced from the water volume in the source cell, and added to that of the target cell.

Regions of high seepage can be identified by extracting the flow of each cell per step and averaging this value over a number of steps. This can then be represented graphically. Furthermore, the discharge into the relief wells can be determined by dividing the average flow volume per step (into the relief well cell) by the step time. These values can be subsequently correlated to the measured well discharge (Equation A.13.).

$$discharge_{(relief\ well)} = \frac{flow_{average}}{step\ time} \qquad (A.13.)$$

This process is looped for every cell within the plane for a predetermined number of iterations. The number of required iterations is just enough to obtain a representative average of the flow from each cell. Instantaneous results may be obtained by setting the number of iterations to 1 in order to determine the maximum possible flow rate.

A.4.8 Hydraulic head distribution

The fact that multiple planes were involved made calculating the hydraulic head complicated as a number of flow paths were possible for any one fluid particle. This was solved by determining a number of flow path scenarios, for a fluid particle, throughout the network. This required splitting Plane 1 into a number of segments namely

- 1a: Plane 1 start till intersection with 2a
- 1b: Intersection with 2a to intersection with 2b
- 1c: Intersection with 2b to intersection with 3
- 1d: Intersection with 3 to plane 1 end

The flow scenarios and their associated flow paths include:

- Scenario 1: 1a – 1b – 1c – 1d
- Scenario 2: 1a – 1b – 1c – 3
- Scenario 3: 1a – 1b – 2b
- Scenario 4: 2a – 1b – 1c – 1d
- Scenario 5: 2a – 1b – 1c – 3
- Scenario 6: 2a – 1b – 2b.

The planes were assumed clean, and as such, the hydraulic head was determined from the cubic law as for the clean fracture in the pegmatite vein. This resulted in hydraulic head values of:

- Plane 1: h = 9.34 m/s
- Plane 2a and 2b: h = 21.02 m/s
- Plane 3: h = 2.34 m/s.

The next issue was the heterogeneous conditions along the flow paths of scenarios 2 to 6, as the hydraulic conductivity along the length is not consistent. A larger amount of energy (thus head) is lost in lower permeable zones than higher permeable zones within a heterogeneous medium. The heterogeneous distribution was corrected for by using a scale transformation factor as used in anisotropic conditions (Equation A.14.)

$$F_H = \sqrt{\frac{K_{ref}}{K}} \qquad \text{(A.14.)}$$

Where the reference hydraulic conductivity (K_{ref}) is the hydraulic conductivity of one of the heterogeneous segments, and is taken as that of Plane 1 since it appears in each scenario. Initially the head is calculated as for a homogenous system (Equation A.10) and difference between the homogenous head and the current head is found. This difference is then multiplied with the scale transformation factor and then subsequently added the current head value obtaining a new heterogeneous hydraulic head. As such, the cells of higher hydraulic conductivity will yield a correction factor of less than 1 resulting in a smaller change in head and thus the heterogeneous head will differ to a lesser extent from those surrounding it. This results in a smaller hydraulic gradient existing in the more permeable regions. The opposite is apparent with lower permeable zones as the correction factor exceeds 1 and thus results in a higher hydraulic gradient. This process can be summarised into the following equation:

$$h_{het} = h_{cur} + F_H(h_{cur} - h_{\text{ho}}) \qquad \text{(A.15)}$$

Where:

- h_{het} is the hydraulic head calculated for a heterogeneous system
- h_{cur} is the current head prior to the calculation of the new head
- h_{ho} is the head calculate for a homogenous system

The hydraulic head distribution is calculated for all the scenarios with the boundary conditions fixed. The boundary conditions were allocated as:

- Upstream head of 50 m at y = 0 m
- Downstream head of 20 m at y = 20 m

This produced a total head loss of 30 m through the heterogeneous network.

Once the head for each scenario was determined, the minimum head for each cell of the intersections was taken over all the scenarios, and subsequently recorded to a reference sheet. The reasoning for taking the minimum head is that it is assumed that the head at any point in the network is a function of the easiest flow path to that point.

The head throughout the entire fracture network is subsequently re-evaluated; however with the minimum heads at the intersections included with the boundary conditions. The head distribution is thus calculated in a homogenous manner as the intersection boundaries separate the heterogeneous zones from one another and as such all the cells within the boundaries are homogenous.

A.4.9 Calculating the flow

The flow is calculated in the same manner as that for the pegmatite vein save for the addition of multidirectional flow. This feature is required for occasions where a water molecule has multiple options for flow, such as is the case for divergent intersections.

The net outflow from the final columns of Planes 1, 2b and 3 was recorded such that the cross sectional seepage out of the network could be determined. This allowed for comparison between ungrouted and grouted networks, along with the effectiveness of the different grouting scenarios.

A.4.10 Instantaneous seepage

From Darcy's equation, the seepage from a point is dependent on permeability and hydraulic gradient. For an established flow system, the flow can be assumed to be at steady state, and as such, the hydraulic gradient is constant. Furthermore the hydraulic conductivity at a point can be further assumed as constant. As such, the seepage from each cell can be considered constant with time. As a result, attaining the seepage for a single iteration at fully saturated conditions should sufficiently characterise the flow characteristics for the fracture with time, for a given steady-state condition.

A change in reservoir level will however result in the redistribution of the hydraulic head, and therefore change the hydraulic gradient, resulting in altered flow volumes. This may not be a concern as modelling for the largest possible hydraulic gradients, for maximum reservoir level, should account for the worst case seepage scenario.

A.4.11 Model assumptions

The general assumptions where:

- Darcy's law applies, thus saturated, steady state and laminar flow is assumed; and
- The hydraulic head distribution through rock fractures and fracture networks can be determined through a simple numerical flow net analysis.

Specific assumptions made of the pegmatite vein model included:

- Pegmatite vein geometry:
- The dip magnitude is constant with depth and varies linearly between surface measurements.
- The dip and strike of the plane is continuous in both the upstream and downstream directions where they were not mapped.
- The aperture remains constant throughout the plane.
- The hydraulic conductivity for each test is constant throughout the plane.
- The hydraulic conductivity assumptions as per §A.4.5.
- The upstream hydraulic head at the time of measurement can be approximated from the full supply elevation of the dam (914.5 meters above mean sea level) and the average foundation elevation at Block 108 and 110 (890 m). This results in a hydraulic head of 25 m with reference depth being the average foundation level.
- For the hydraulic head distribution, the pegmatite vein is assumed homogenous and isotropic.
- The seepage through the rock mass is predominantly dependent on the seepage of the pegmatite vein. As a result, the discharge measurements of the relief wells are representative of the discharge from the pegmatite vein.

Appendix B. VERTICAL CLEAN SMOOTH PARALLEL FRACTURE

B.1. Observations from the Vertical Inclination Tests at 1G

B.1.1 Continuous flow

Wetting

Immediately after water is introduced to the top of the fracture via the inlet pipe at 20 l/hr, a breach occurs into the fracture as a single droplet. This air-water meniscus advances vertically through the fracture, without the thread behind it snapping (Figure B-1a). Seventy (70) milliseconds after the water is introduced the thread widened in order to accommodate a higher volume of water, and the it becomes a rivulet which begins to oscillate (Figure B-1b). At the same time water spreads and ponds along the top of the fracture, which causes a breach of 2 new droplets on either side of the initial rivulet, with accompanying threads behind. These droplets and accompanying threads almost immediately become rivulets due to the large volumes of water flowing through them. They too oscillate, causing one of the rivulets to connect with the initial rivulet in the middle (Figure B-1c), 1 second after water was introduced. At 3 seconds after water was introduced the formation of new droplets, which turn into rivulets, continue to invade dry portions of the fracture. All rivulets continue to oscillate with some bubbles observed at the bottom of the fracture. At 4 seconds, another rivulet forms via the invasion of a droplet with a thread, into a dry portion of the fracture. At the same time the rivulet observed on the left ceases to flow, which leaves behind static droplets on the fracture (Figure B-1e). Episodic flow of droplets down a drying rivulet is observed at 10 seconds after water is introduced. Throughout the rest of the 20 l/hr wetting interval, flow regime continues in the same manner with the same observations seen throughout, and only approximately 10% of the fracture being saturated. Ultimately the final flow mechanism consists of a set number of separate individual oscillating rivulets occurring within the fracture.

Approximately 30 seconds into the first interval, a breach occurs at the left edge of the fracture, which causes a rivulet to make contact with the spacers which contain the fracture along its height. This causes a boundary error as water preferentially flows along this contact point down the fracture. At the start of the second interval (40 l/hr) flow remains through the present rivulets in the fracture (Figure B-2a). Rivulets are seen forming along rewetting paths, along static droplets (Figure B-2b), which eventually causes the same boundary error along the spacer containing the left of the fracture at 4 seconds into the 40 l/hr interval (Figure B-2c). Two minutes into the second interval, the diagonal rivulet running in the middle of the fracture begins flowing episodically, as the majority flux of water moves along the right boundary with the fracture (Figure B-2d).

Throughout the subsequent testing intervals, similar flow regimes are observed (Figure B-3). A major observation throughout the wetting stages is that of rivulet flow switching. As multiple rivulets are already established within the fracture, at multiple separate occasions, a single continuous rivulet would break leaving behind stationary droplets. A momentary pause occurs where the broken rivulet does not reconnect. A new entry point forms a new droplet that follows a separate new and non-wetted path. This new breached path results in the formation of a new rivulet that is adjacent to the broken rivulet, which remains broken.
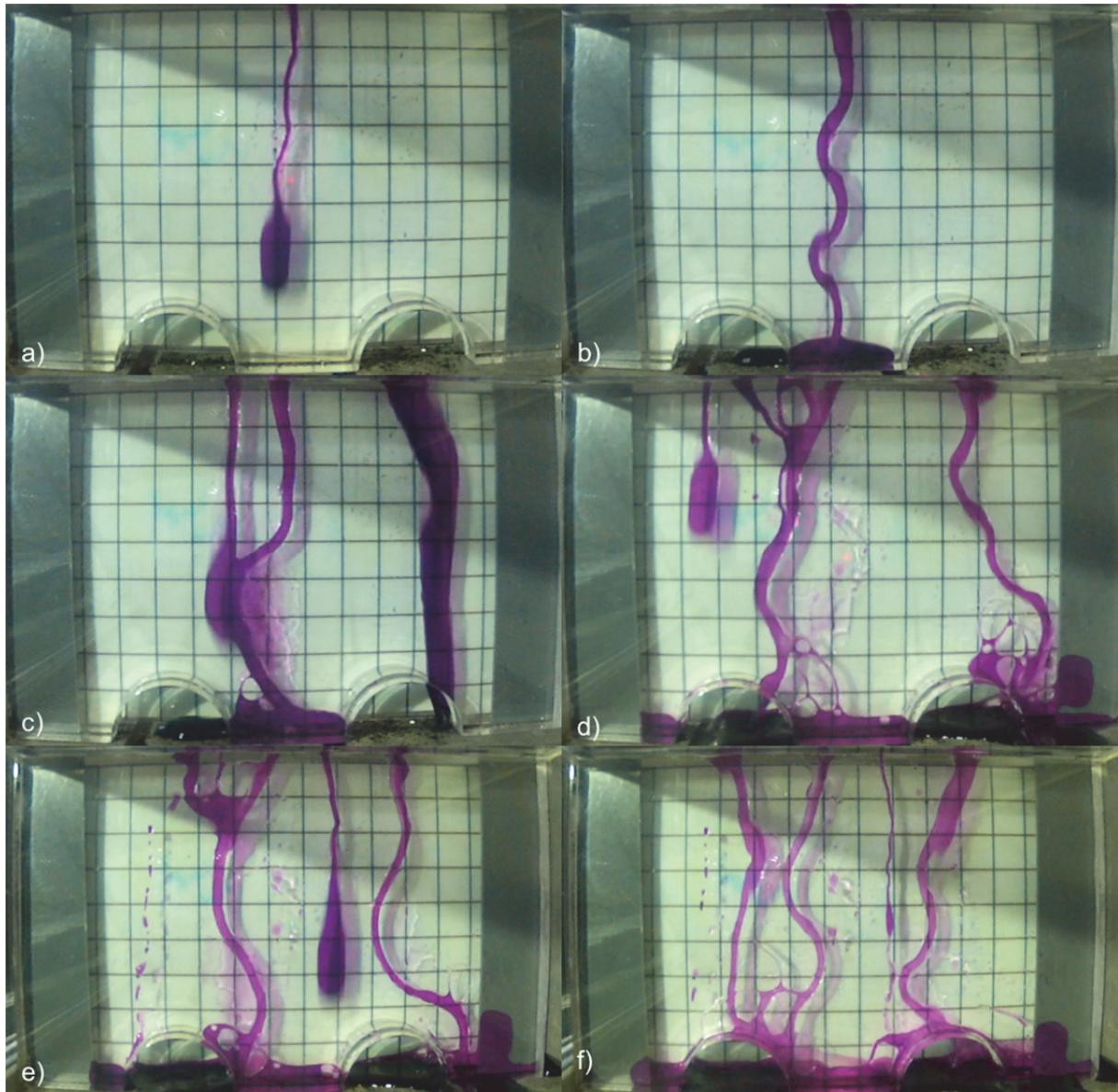
Figure B-1.   Flow regimes observed at a flow rate of 20 l/hr during the wetting stage.
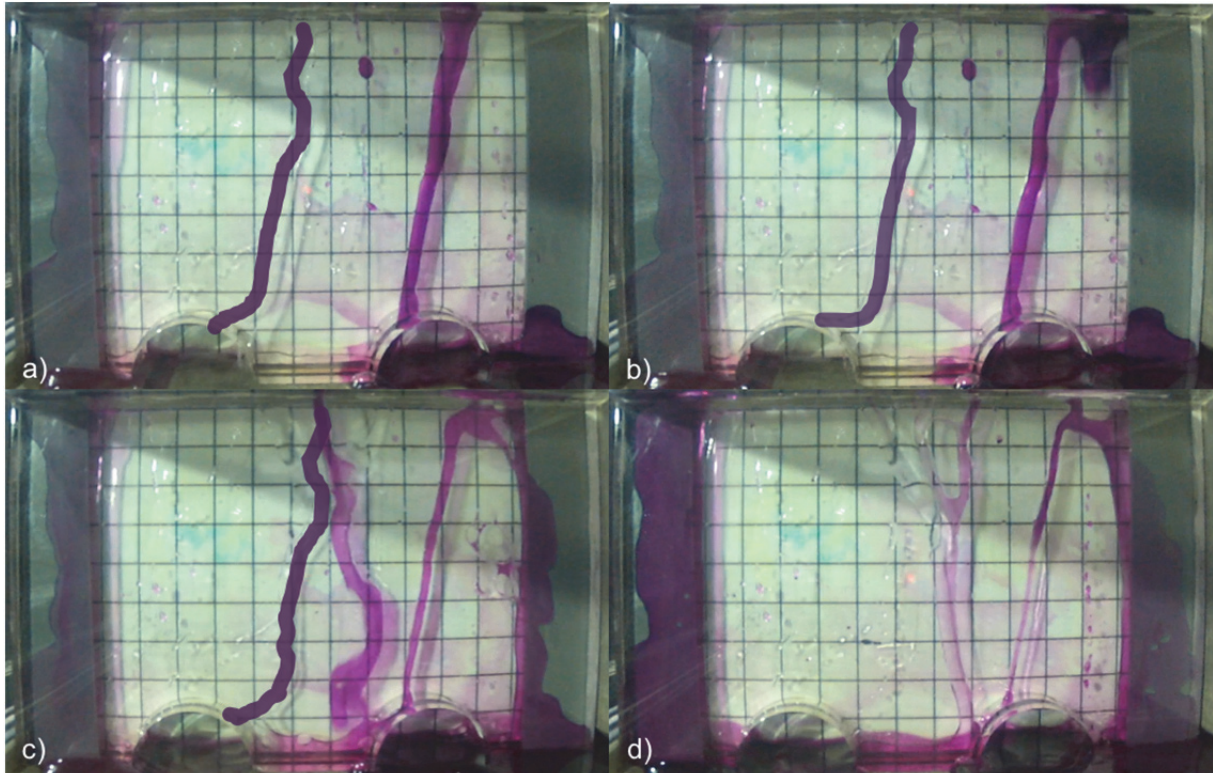
Figure B-2.   **Flow regimes observed at a flow rate of 40 l/hr during the wetting stage. Drawn-in lines help identify flow paths, which did not have sufficient potassium permanganate dissolved.**

Drying

When the water supply is stopped, the broken rivulets leave behind a line of separate static droplets following the path of the rivulet. Sporadic droplet flow occurs along the broken rivulet path (Figure B-4a). This drying scenario occurs for all the rivulets present within the fracture until all the rivulets break into static droplet paths and no further sporadic droplet flow occurs (Figure B-4b).
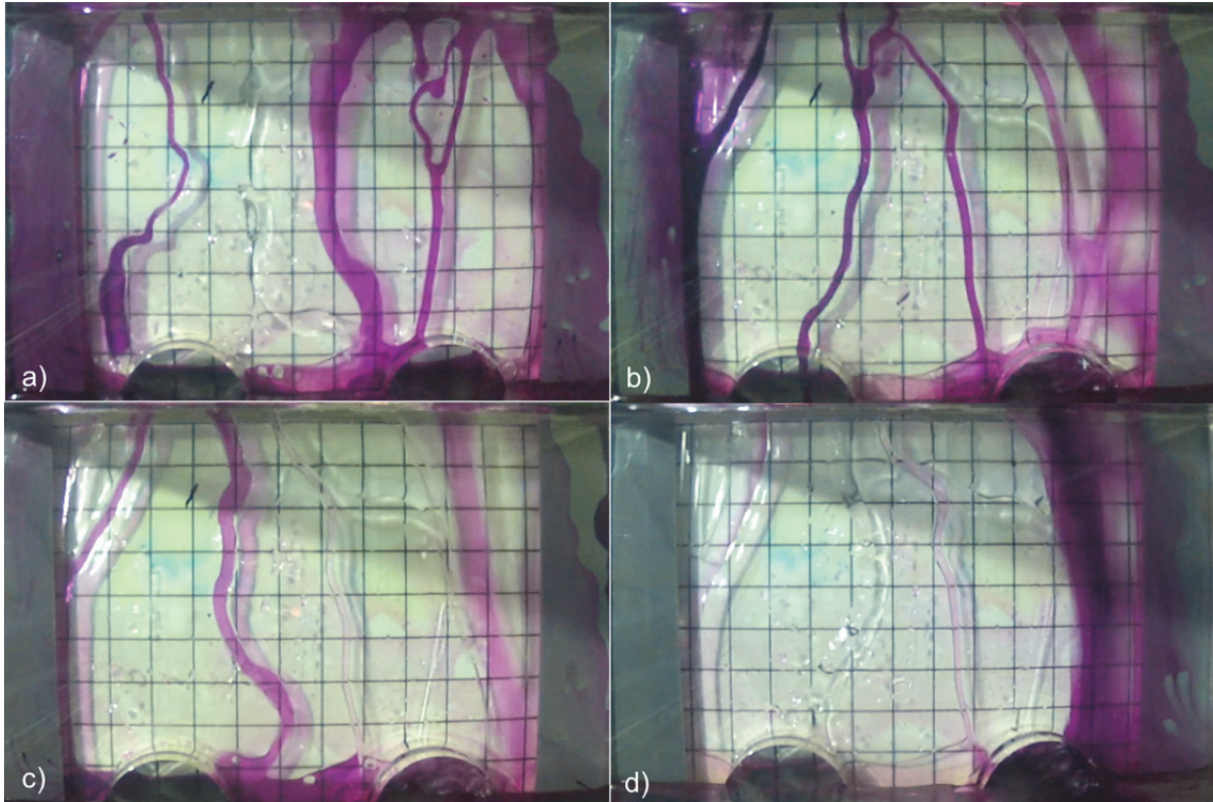
Figure B-3. Similar flow regimes observed at a flow rate of 60, 80, and 100 l/hr during the wetting stage.
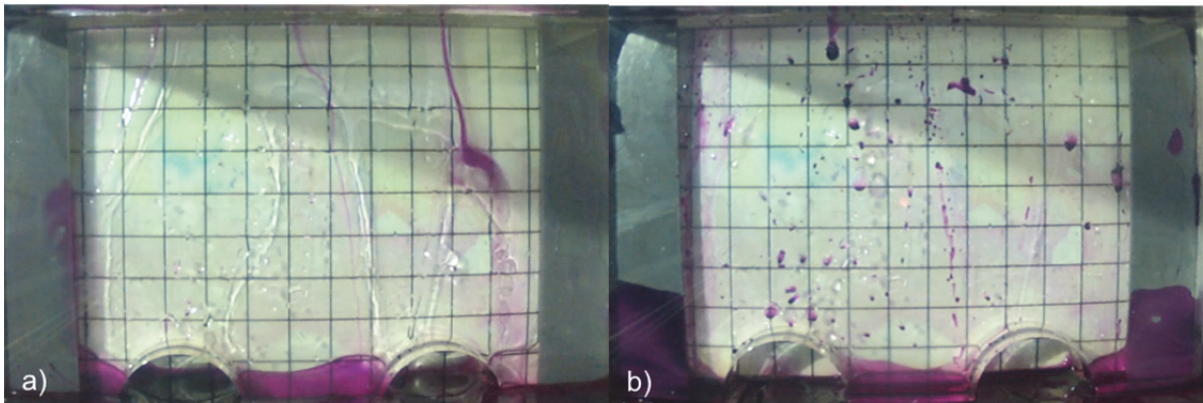
Figure B-4. Observations of drying when water supply is stopped.

Rewetting

Upon re-addition of water, droplets follow previous flow paths along static droplets throughout the fracture (Figure B-5). Each single droplet reconnects the stationary droplets into a new rivulet following the same path. This process repeats itself, reconnecting all the remaining remnant rivulet pathways, while forming no new flow pathways within the fracture during rewetting at all flow intervals in the rewetting cycle. The same observation is made during all

rewetting intervals, with rivulet oscillations and flow switching dominating the flow regime in the fracture.
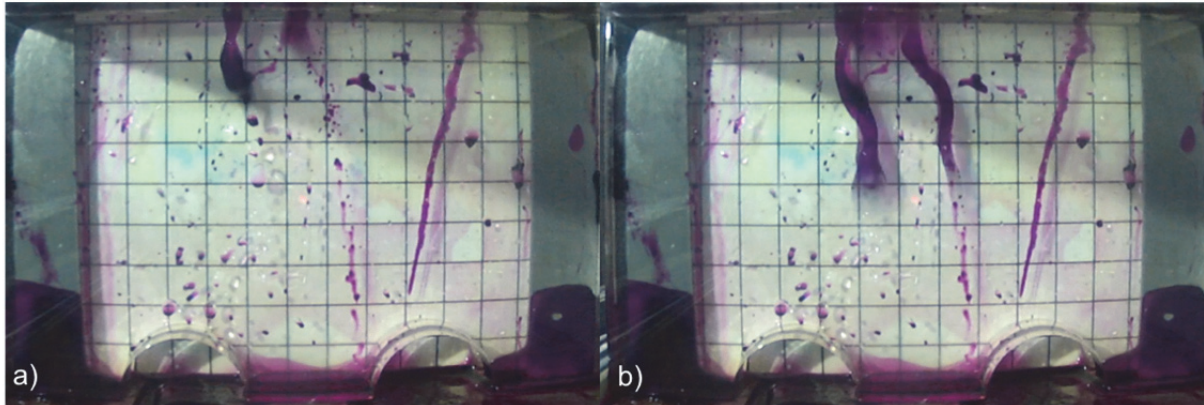
Figure B-5 . **Rewetting of the fracture at 20 l/hr, shows rivulets forming along previous flow paths along static droplets in the fracture.**

B.1.2 Seepage flow

At this low flow rate an air-water meniscus in the form of a droplet, enters the fracture. This droplet advances through the vertical fracture, and before it reaches the bottom the thread behind it snaps. The seepage experiment completely mimics the findings of Su et al. (1999), who observed the same flow mechanism at low flow rates below 8 mL/hr. This observed flow regime was similar to the phenomenon of the dripping faucet as stated by Su et al. (1999) and Glass and Nicholl (1996), whereby water breaks off from the liquid supply when the weight of the water is greater than the surface tension force. Once the thread snaps, it leaves behind static droplets along the fracture wall. When the following advancing droplet enters, its flow path is governed by these existing static droplets. Although not quantified, it is assumed that the same total volume of static droplets is present before and after each droplet has fallen vertically through the fracture.
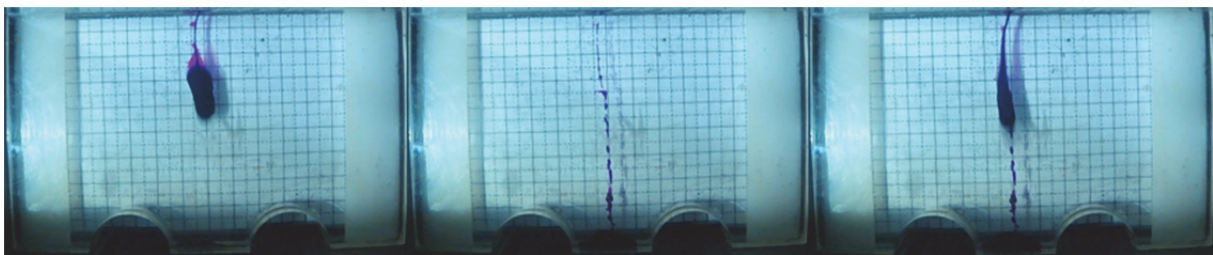
Figure B-6. **Screenshots of the intermittent (droplet) seepage experiment, under 1G conditions (5 mm x 5 mm grid).**

B.2. Observations from the Vertical Inclination Tests at 20G

B.2.1 Continuous flow

Wetting

The formation of rivulets is also evident in the 20G test, however the speed at which these rivulets formed too fast for the camera to record, and consequently the wetting from of the air-water meniscus was not observed. Within a single frame, rivulets had formed, which indicates that flow occurs from the top of the fracture to the bottom of the fracture in less than 16.7 msec. Figure B-7a shows the initial formation of 2 rivulets, which by the next frame had reached the bottom of the fracture. The formation of these rivulets within at least 16.7 msec relates to a prototype scaled time of at least 6.67 sec. By the next frame, 0.0334 msec after water begun invading the fracture an additional 3 rivulets had formed (Figure B-7c). Similar oscillation as well as the flow-switching of rivulets is observed within the first 283.9 msec of the 20 l/sec interval (Figure B-7d, e, and f). The notable difference in any flow regime of the 20G test was the movement of droplets, with short threads behind, down the fracture. Again only approximately 10% of the fracture is saturated and contributes to the flow of water through the vertical aperture.

At the subsequent intervals, higher flow rates seem to give rise to a sheet flow pattern, with less droplets scattered through the fracture. This sheet flow was observed firstly in the 40 l/hr interval (Figure B-8a) together with the thinner rivulets and droplets in the fracture. However, the sheet flow paths changed width and moved erratically, which lead less droplets being able to remain on the fracture walls. This sheet flow was observed throughout the 60 l/hr (Figure B-8b), 80 l/hr (Figure B-8c), and 100 l/hr (Figure B-8d) intervals.

Drying

During drying of the fracture broken rivulets leave behind a line of separate static droplets following the path of the rivulet. As in the 1G test some droplet flow occurs along the broken rivulet path (Figure B-9). Towards the end of the drying stage, this droplet flow decreases, and only static droplets remain in the fracture.
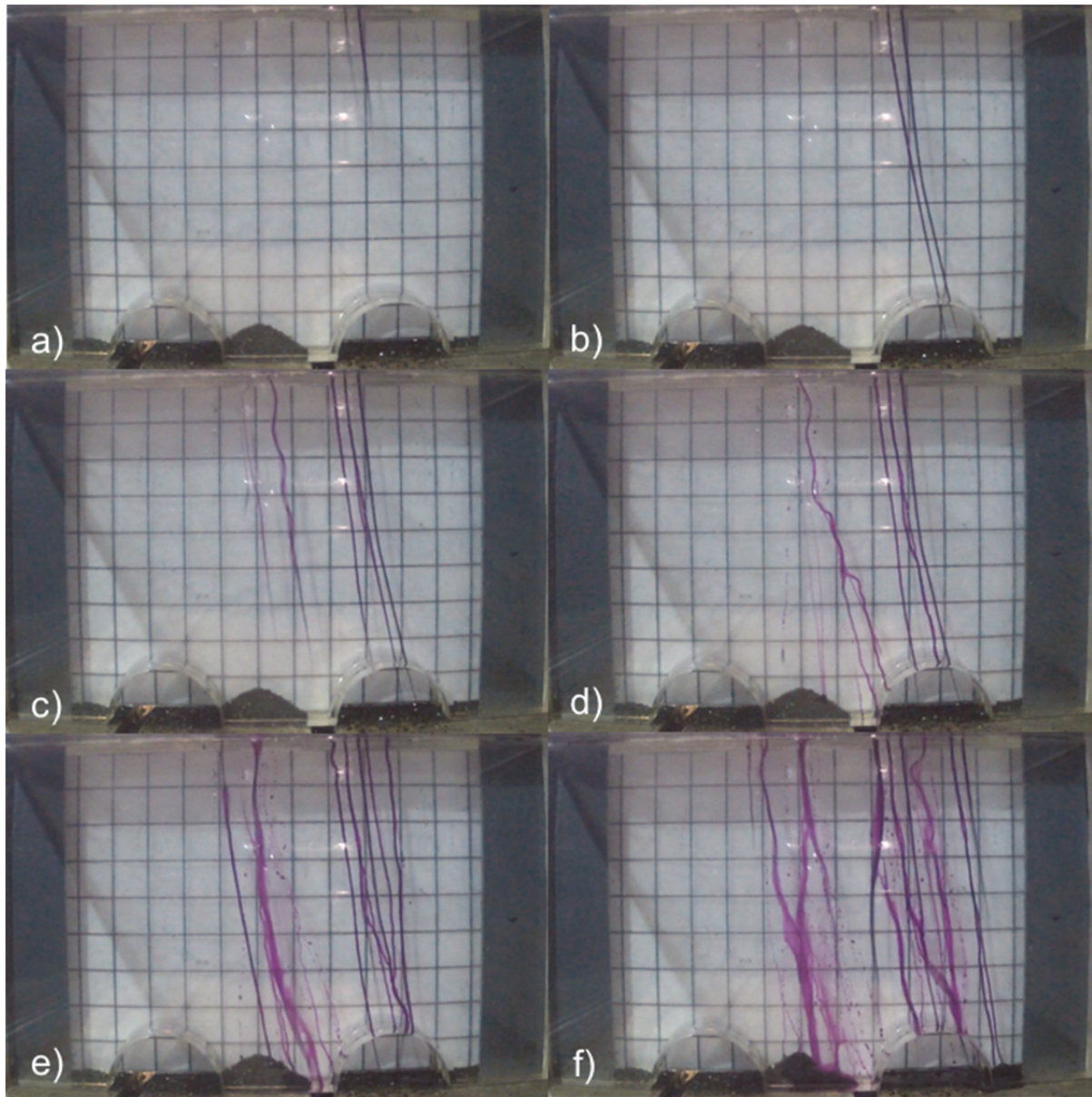
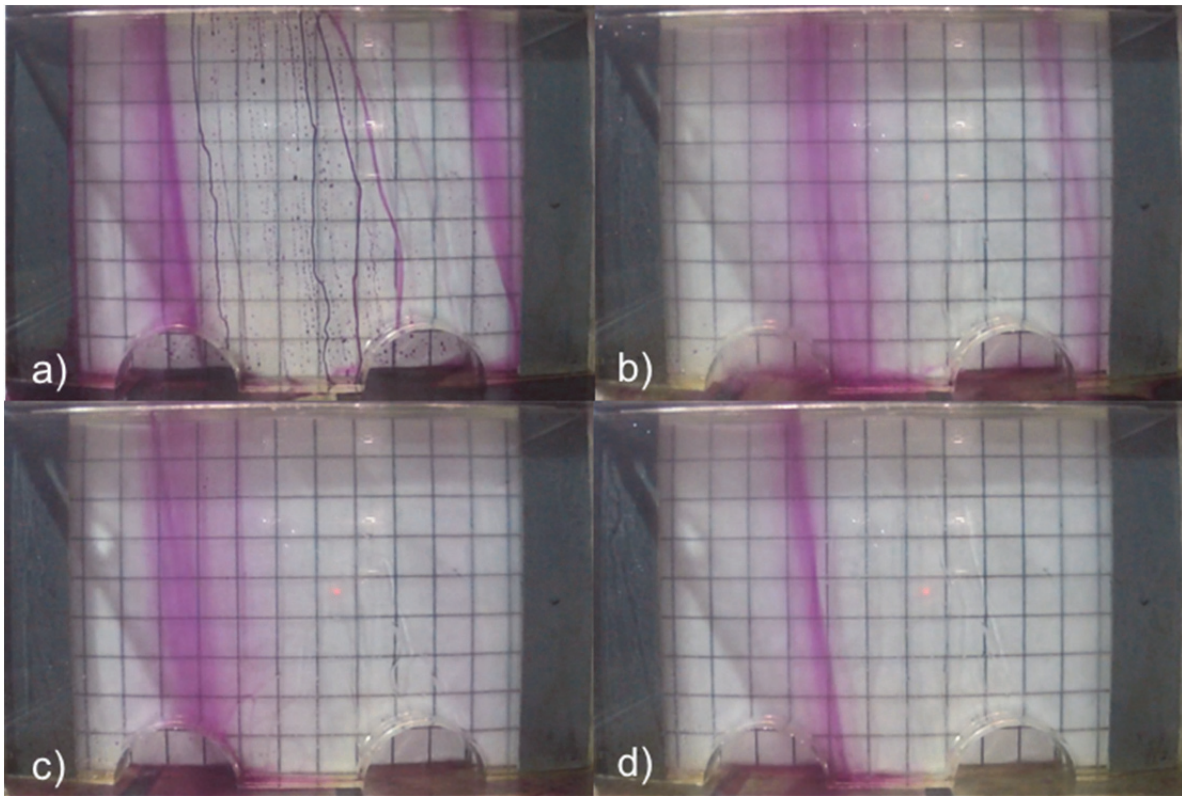**Figure B-7.** Flow regimes observed at a flow rate of 20 l/hr during the wetting stage at 20G.

Figure B-8. Flow regimes observed at flow rates of: a) 40 l/hr, b) 60 l/hr, c) 80 l/hr, and d) 100 l/hr at 20G.

Figure B-9. Drying of the vertically inclined fracture during the 20G test.

Rewetting

Rewetting of the fracture resulted in continued observation of film flow, from the 20 l/hr interval. This was unlike the initial wetting cycle where sheet flow was only observed at later intervals. However, at the 20 l/hr rewetting interval, rivulets are present which become less frequent at higher flow rate intervals, as observed in the wetting cycle.

B.2.2 Seepage flow

Unlike the 1G experiment, a continuous rivulet is seen forming within the first second of the 20G test. No significant droplet (air-water meniscus) is seen preceding the flow of this rivulet down the fracture, and the wetting front seems as wide as the rivulet which trails it. Throughout the test this rivulet does not snap nor break. This is similar to the regime observed by Su et al. (1999) at high flow rates above 12 mL/hr. When the flow rate of 0.7 l/hr is upscaled to prototype conditions, the equivalent flow rate is 14 mL/hr. Once again, this highlights that regimes observed in previous literature are observed for the same prototype flow rates in the centrifuge.

A second flow paths appears 58 seconds into the experiment. The flow regime observed in this flow path is unlike the initial rivulet, and is similar to that of the dripping faucet as stated by Su et al. (1999) and Glass and Nicholl (1996). Discrete droplets slightly wider than the rivulet adjacent break off from the supply when the weight of the water is greater than the surface tension force. Once the thread snaps, it leaves behind static droplets along the fracture wall, as observed in the 1G test. When the following advancing droplet enters, its flow path is governed by these existing static droplets. It is assumed that the water supply to this droplet flow path was much less than that which formed the continuous rivulet, and may have formed due to a lateral wetting of the fracture entrance. If indeed this regime is observed, with snapping droplets, then the water supply to this flow path must be below 8 mL/hr at prototype scale (0.4 mL/hr at model scale) as stated by Su et al. (1999).
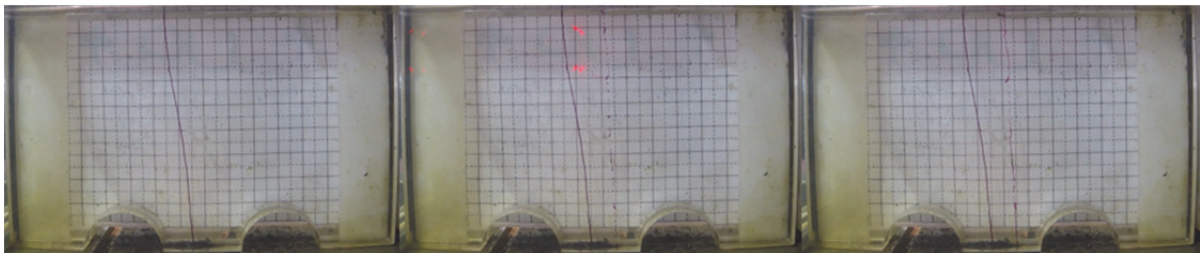

Figure B-10. Screenshots of the intermittent (droplet) seepage experiment, under 20G conditions (5 mm x 5 mm grid).

Appendix C.   HORIZONTAL CLEAN SMOOTH PARALLEL FRACTURE

C.1. Observations from the Horizontal Inclination Tests at 1G

C.1.1   Continuous flow

Wetting

Wetting front initially spreads elliptically (Figure C-1a and b) but changes to an irregular front at about 3 seconds (Figure C-1c). Flow paths are illustrated by the potassium permanganate lineaments along the fracture. Eventually the wetting front reaches the vertical unconfined wall (Figure C-1e) and rivulets form down the vertical wall. The horizontal fracture remains saturated immediately after the wetting front reaches this vertical exit wall.
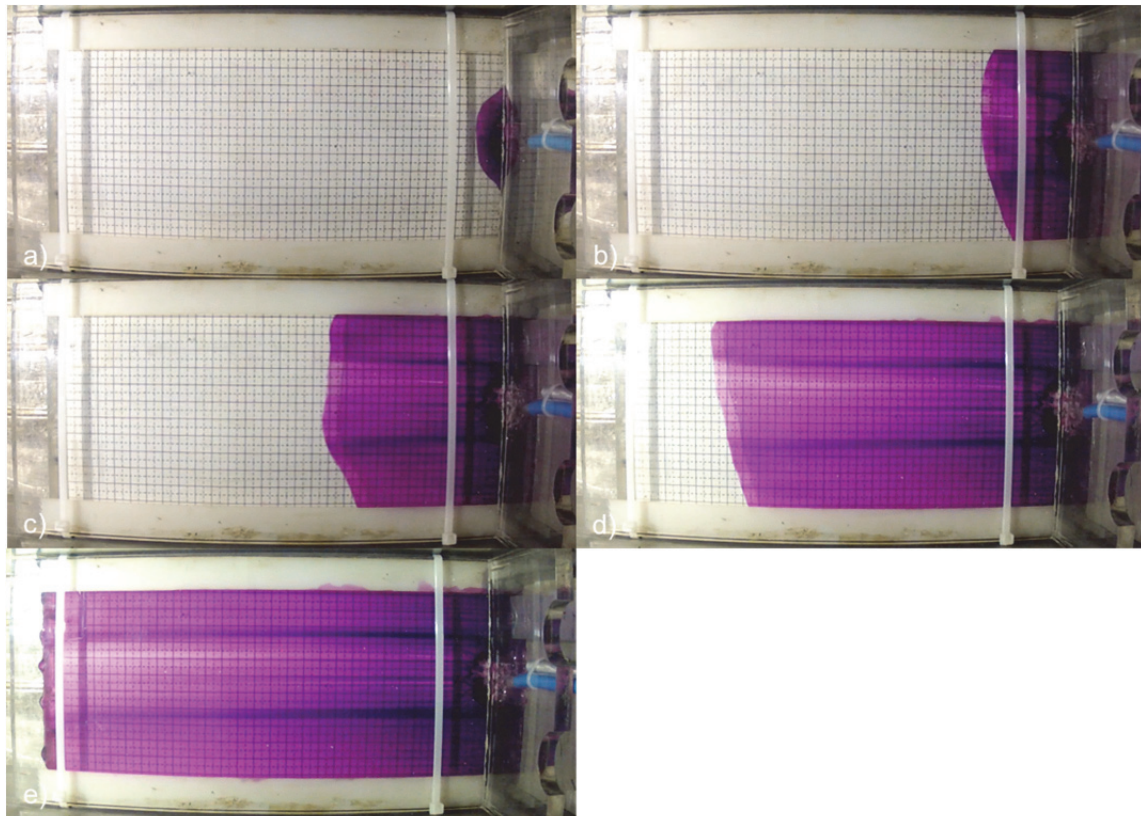
Figure C-1.   Wetting phase at 20 l/hr in horizontal fracture: a) 0.5 sec; b) 2 sec; c) 3 sec; d) 6 sec; e) 8 sec; 8.5 sec.

The flow regime appears not to change as the flux is stepped up. Figure C-2 highlights how the faster flow path in the centre of the fracture expands towards the spacers from 60 l/hr (Figure C-2b) and up to 100 l/hr. The darker purple towards the spacers indicate slower fluid movement as opposed to the lighter colour in the centre.
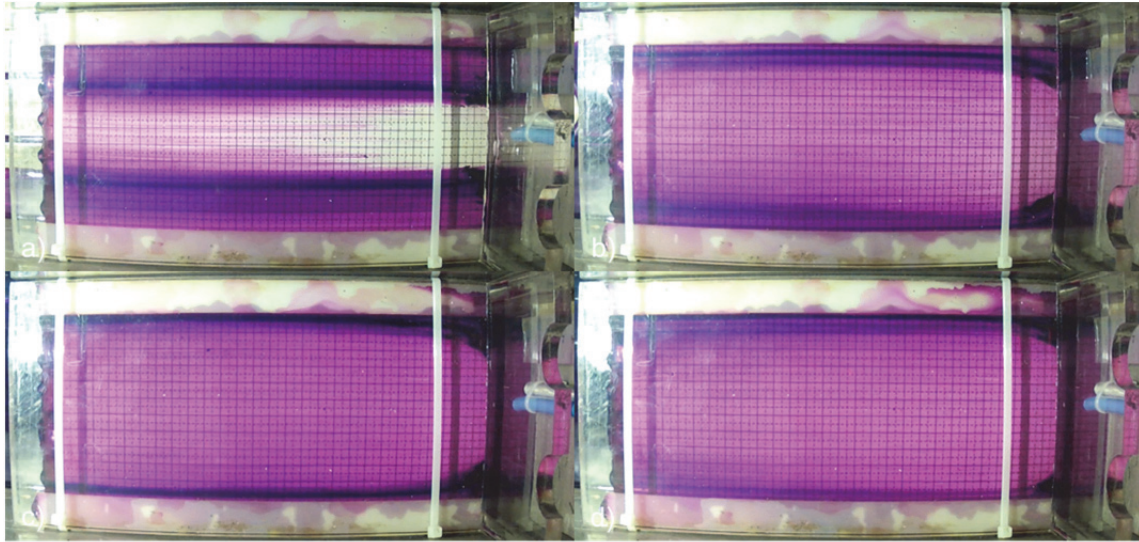
Figure C-2.   Wetting phase at: a) 40 l/hr; b) 60 l/hr; c) 80 l/hr, and; d) 100 l/hr.

Figure C-3 illustrates the exit regime of the fluid out of the horizontal fracture, and into the unconfined vertical wall. Initially once the horizontal fracture is saturated and the wetting front reaches the vertical wall, the first rivulet forms in the centre. Twenty-five seconds after the first rivulet appears, an additional 3 rivulets have formed across the vertical wall. Another 15 seconds later, and fifth rivulet begins flowing down the vertical wall. From that point onwards, the flow regime and amount of rivulets remains unchanged, until the 60 l/hr influx (Figure C-3d) whereby 2 of the central rivulets have an obvious increase in volume of water. Forty-seconds into the 80 l/hr interval these rivulets join and become a large rivulet exhibiting film flow. Throughout the testing some oscillating at the begging of the intervals but then stabilises.
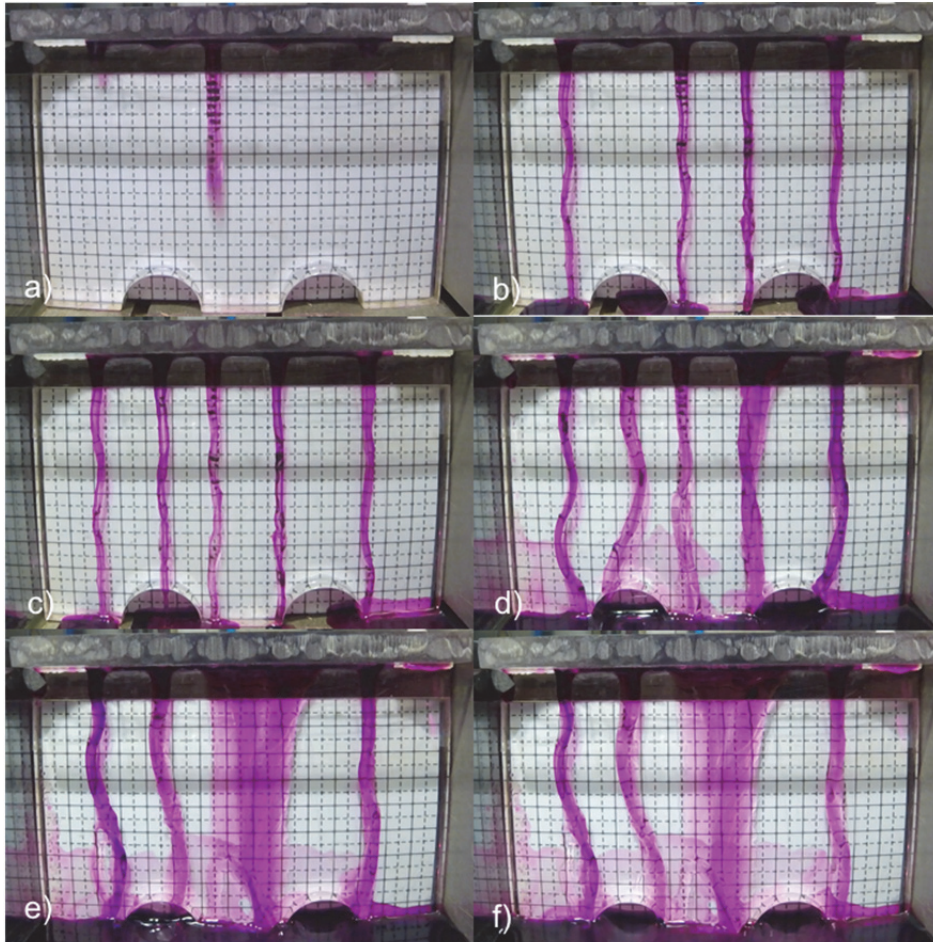
Figure C-3. **Flow regime of the fluid out of the horizontal fracture onto the unconfined vertical wall for: a) 20 l/hr at 5 sec; b) 20 l/hr at 30 sec; c) 20 l/hr at 45 sec; d) 60 l/hr; e) 80 l/hr, and; 100 l/hr.**

Drying

The drying stage is shown in Figure C-4. Air enters the fracture from the inlet container side (right hand side of figure) whilst a smaller one enters at the exit (on the left hand side of figure). The rivulets at the outlet vertical wall cease to flow almost immediately after the water is stopped from entering the inlet container, with the 2 outer rivulets being the last to disappear (Figure C-5a), however a few seconds after these rivulets stop transmitting water and also disappear, leaving behind some static droplets on the vertical exit wall (Figure C-5b).
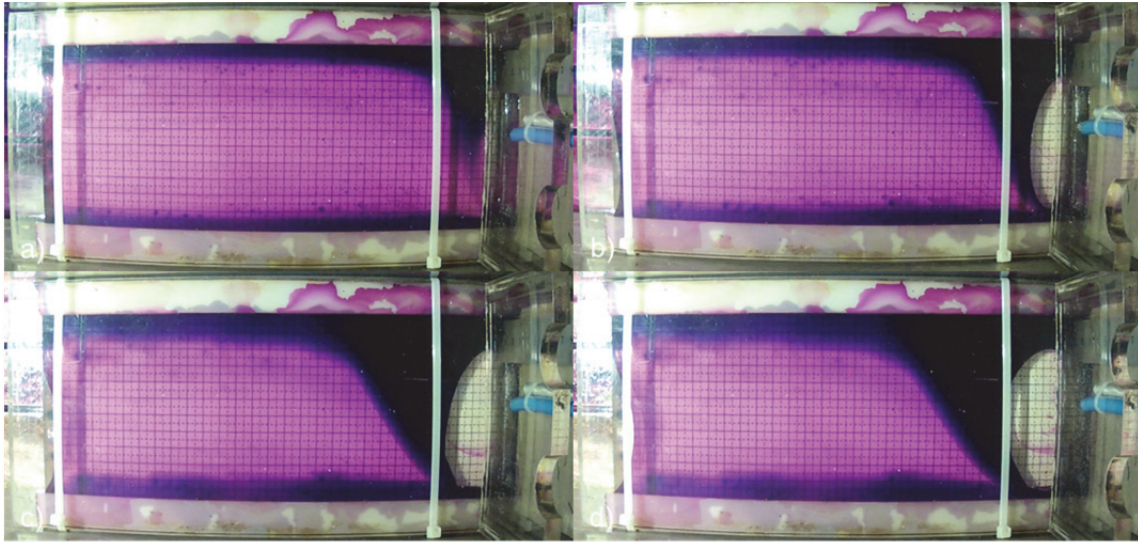
Figure C-4. **Drying interval at: a) 10 sec; b) 40 sec; c) 2 mins; and d) 2 mins 55 sec.**
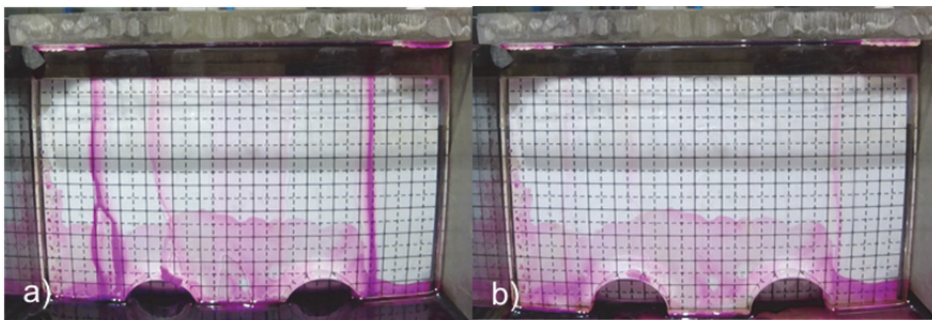
Figure C-5. **Drying of the system out of the horizontal fracture onto the unconfined vertical wall involves the drying out of rivulets, a) 2 second after water was stopped being introduced, and b) 5 seconds after.**

Rewetting:

Upon rewetting at 20 l/hr, a circular wetting front invades the capillary bubble at the inlet (Figure C-6a and b). This wetting front splits the capillary bubble and forms smaller capillary islands as the water moves through the horizontal fracture. Some static capillary islands remain in the fracture whilst other move laterally. A large capillary island can be seen in bottom right of Figure C-6c, which splits and begins to move laterally through the horizontal fracture (Figure C-6d). Some of the static capillary islands are only mobilized as the inlet volume is increased. This is seen in Figure C-7a and Figure C-7b in the 40 l/hr and 60 l/hr interval where it remains stationary, however when the inlet interval is increased to 80 l/hr, the capillary island is mobilized (Figure C-7c). Only a single capillary island in bottom left of fracture near the entrance remains stationary throughout the rewetting phase (Figure C-7d).
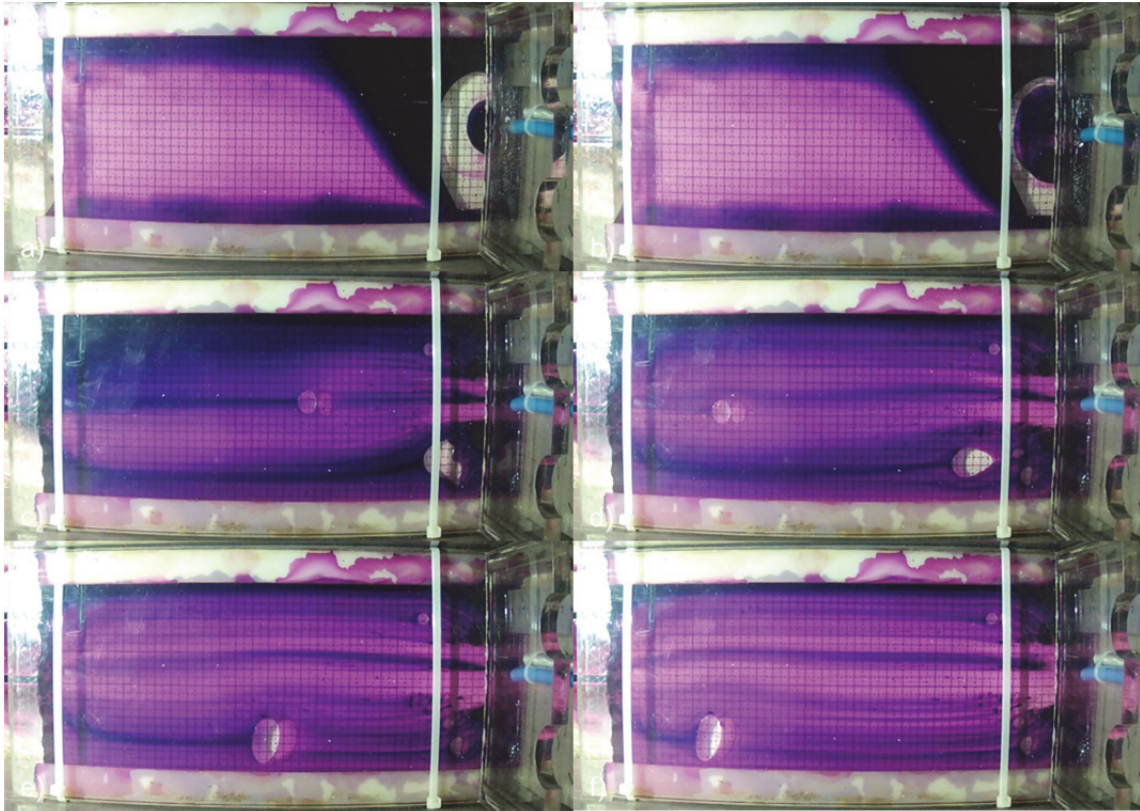
Figure C-6. Rewetting of the horizontal fracture in the 20 l/hr interval, at: a) 0.5 sec; b) 1 sec; c) 10 sec; d) 20 sec; e) 30 sec; and f) 40 sec.
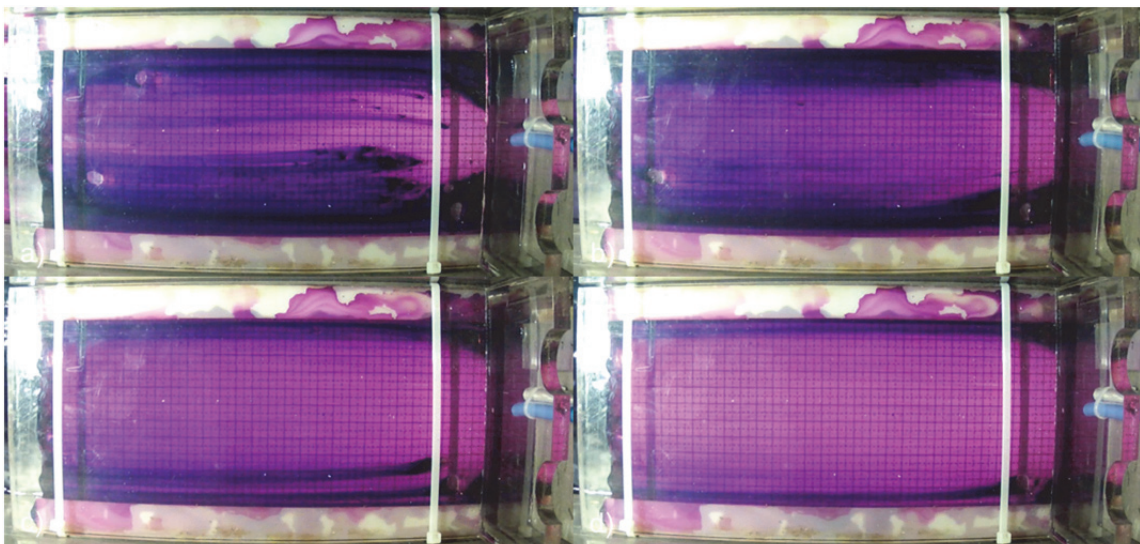

Figure C-7. Rewetting at: a) 20 sec into 40 l/hr interval, b) 20 sec into 60 l/hr interval, c) 20 sec into 80 l/hr interval, and d) 20 sec into 100 l/hr interval.

At the unconfined vertical wall, a single rivulet forms once the horizontal fracture has saturated. This initial rivulet mobilises at the same location that the thick central rivulet had formed in the previous wetting cycle, during the 20 l/hr wetting cycle (Figure C-8a and b). As observed through all initial mobilisation of rivulets, they begin oscillating during mobilisation and settle.

Twenty-seconds into the 20 l/hr rewetting interval, a second rivulet is observed (Figure C-8c), corresponding to the same rivulet formation at 40 l/hr in the wetting phase. A third rivulet forms 4 seconds into the 60 l/hr interval (Figure C-8d), whilst a fourth rivulet forms at 11 seconds. By the 100 l/hr interval (Figure C-8), the four rivulets that are present on the vertical face mirror the same flow regime as observed in the same interval during the wetting phase.
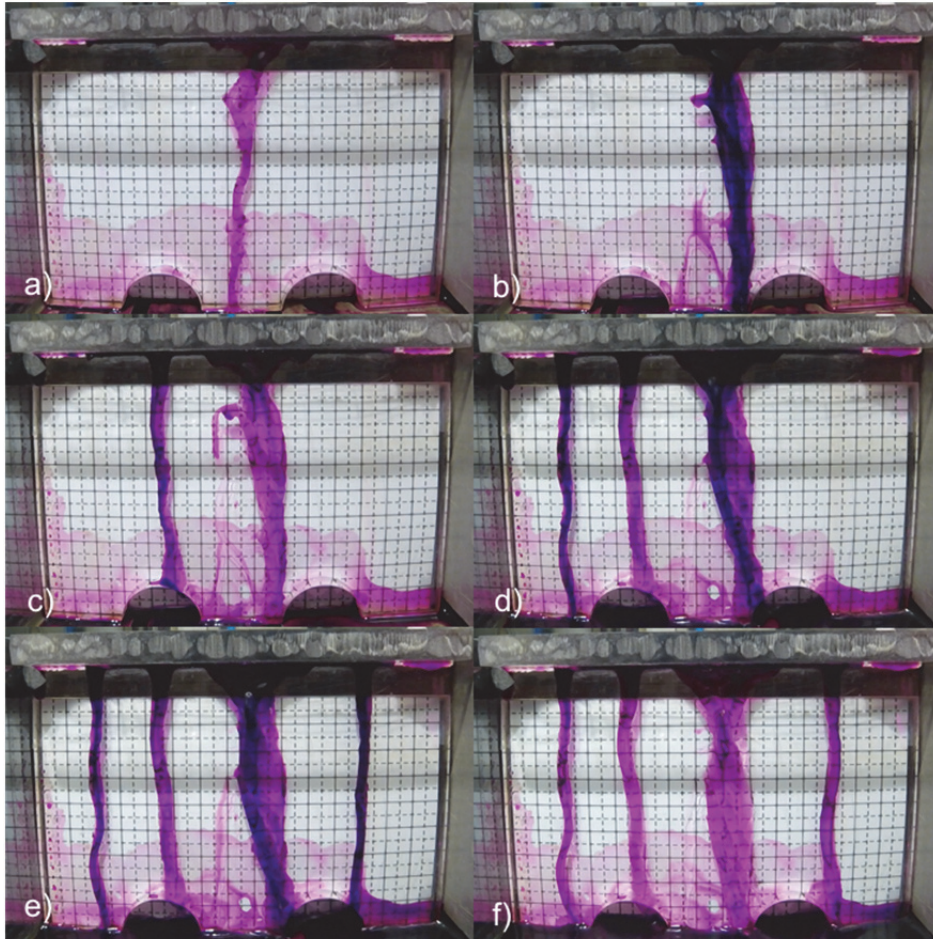
Figure C-8.   Flow regime of the fluid out of the horizontal fracture onto the unconfined vertical face for the rewetting intervals.

C.1.2   Seepage flow

Flow into the horizontal fracture was slightly slower, at approximately 0.4 l/hr, but water supply remained as intermittent droplets. The wetting front is seen invading the horizontal fracture as a circular wetting front in Figure C-9a. Three-minutes into the test although the wetting front is irregular, no capillary islands are left trapped within the horizontal fracture (Figure C-9b and c). The wetting front reaches the vertical outlet wall at 5 minutes 50 seconds into the test (Figure C-9e), but only breaches once the horizontal fracture is fully saturated 17 seconds thereafter (Figure C-9f). As observed in the continuous flow test, the outflow is only concentrated at a discrete point and exits as a single rivulet down the vertical wall. The flow

regime observed at this vertical wall is in agreement with Su et al. (1999) whereby flow greater than 12 mL/hr will consist of a rivulet (thread) that does not snap.
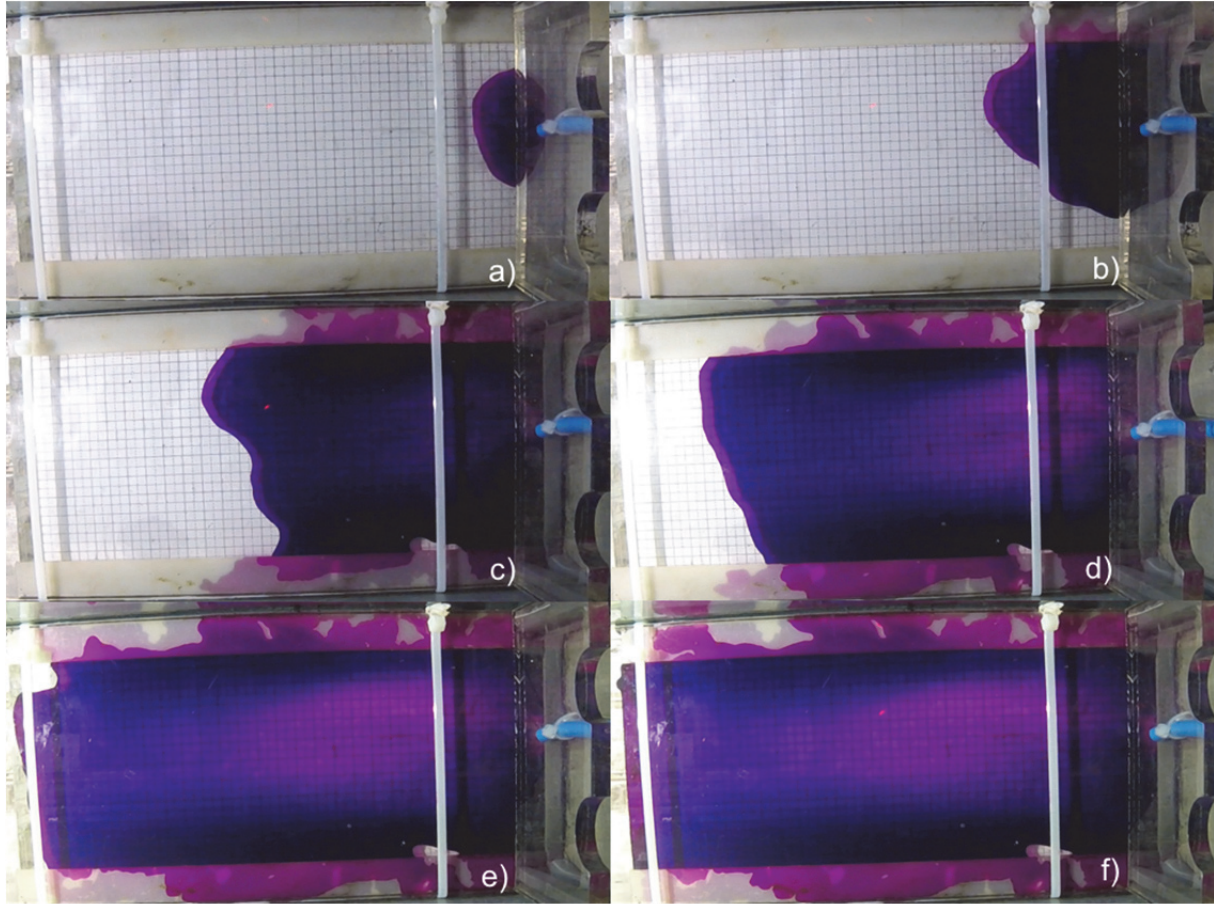

Figure C-9. Snapshots of the intermittent flow test: a) 10 sec; b) 1 min; c) 3 min; d) 5 min; e) 5 min 50 sec; f) 6 min 7 sec.
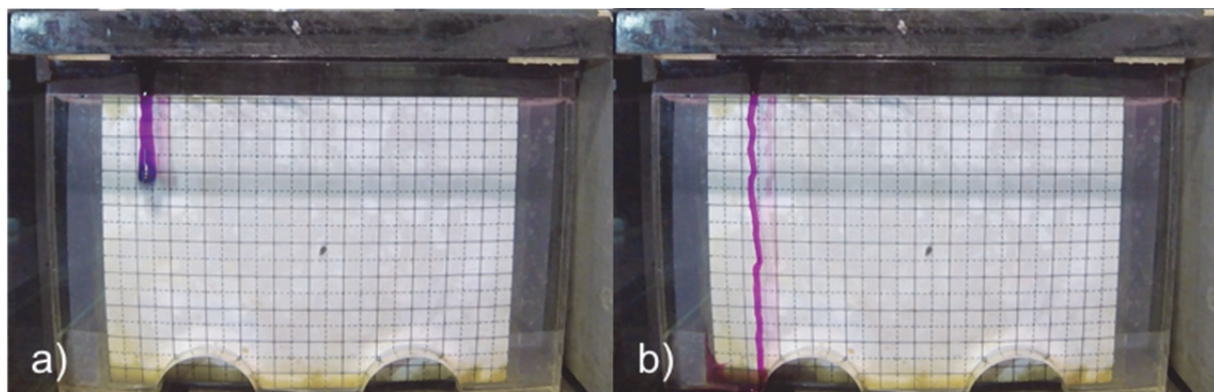

Figure C-10. Flow regime of the fluid out of the horizontal fracture onto the unconfined vertical wall for the intermittent test at 1G.

C.2. Observations from the Horizontal Inclination Tests at 20G

C.2.1   Continuous flow

Wetting

As in the 1G test the wetting front initially spreads elliptically (Figure C-11a), also changing to an irregular front (Figure C-11b and c). Saturation of the horizontal fracture takes 0.71 sec, which corresponds to a prototype time of approximately 4.7 minutes. Saturation of the horizontal fracture occurs immediately after the wetting front reaches this vertical exit wall.
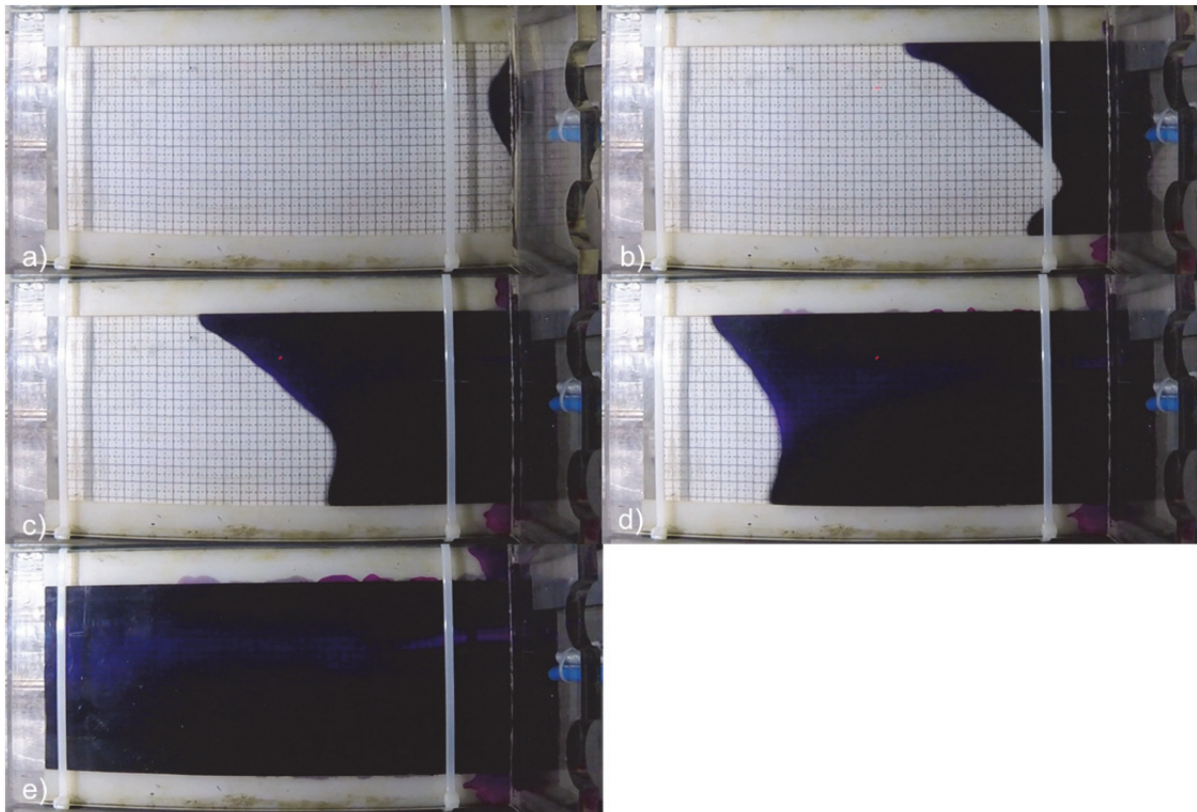
Figure C-11. Wetting phase at 20 l/hr in the horizontal fracture at 20G.

The flow regime appears not to change as the flux is stepped up. Figure C-12 illustrates how the flow paths in the fracture with some flow paths having an undulating character.
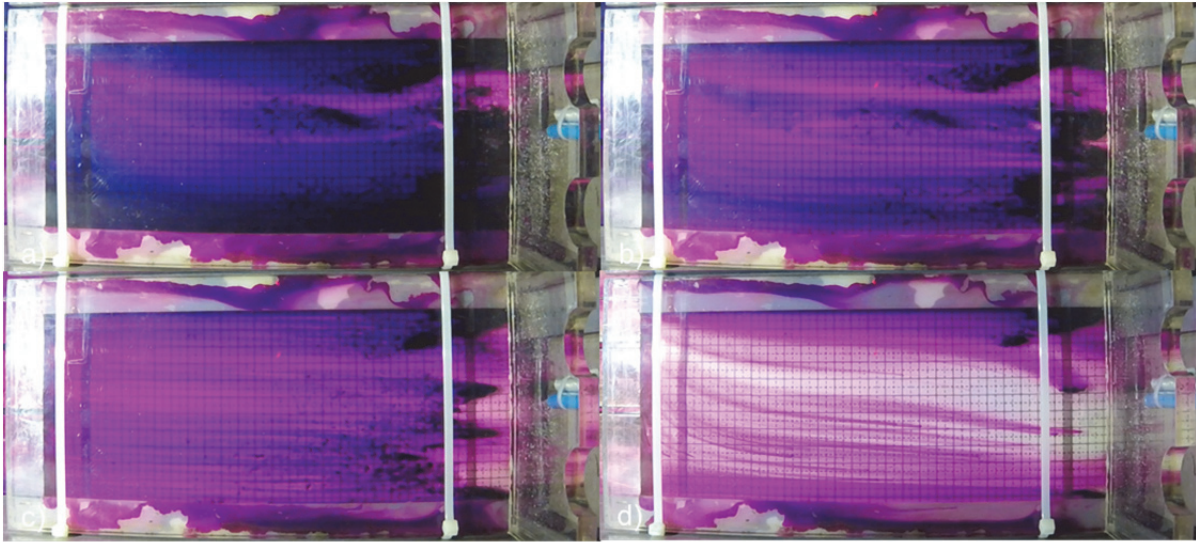
Figure C-12. Wetting phase at: a) 40 l/hr; b) 60 l/hr; c) 80 l/hr, and; d) 100 l/hr.

Figure C-13 depicts how cavitation occurred in the water supply system at 20G. This caused the water supply to be slightly intermittent, rather than a continuous flow as planned. The cavitation lead to moment whereby no flow occurred, followed by a large volume of water being expelled into the inlet container as the backpressure worked through the water supply system. Significantly bad cavitation problems are noticed in the wetting stage from 60 l/hr and upwards. Although this compromised the continuity of the experiment somewhat, observations could be made at the short moments that the correct flow rate was achieved, for any specific interval.

Figure C-14 illustrates the exit regime of the fluid out of the horizontal fracture, and into the unconfined vertical wall. At 20 l/hr a narrow sheet (approximately 10 mm in width) exits the horizontal fracture onto the vertical wall (Figure C-14a). During this interval a narrow oscillating rivulet is noticed on the opposite side of the vertical wall. At 40 l/hr interval the sheet widens to approximately 30 mm, and the rivulet on the left od the vertical wall also carries a large volume of water as it still oscillates. The sheet flow again widens at 60 l/hr to a width of approximately 50 mm, with 2 additional rivulets forming in the middle portion of the vertical wall. These 3 rivulets carry a large volume of water and oscillate aggressively. By 80 l/hr it is obvious that the sheet flow has widened considerably, and by the 100 l/hr interval, the sheet is a wide as the horizontal fracture, leading to a curtain flow.
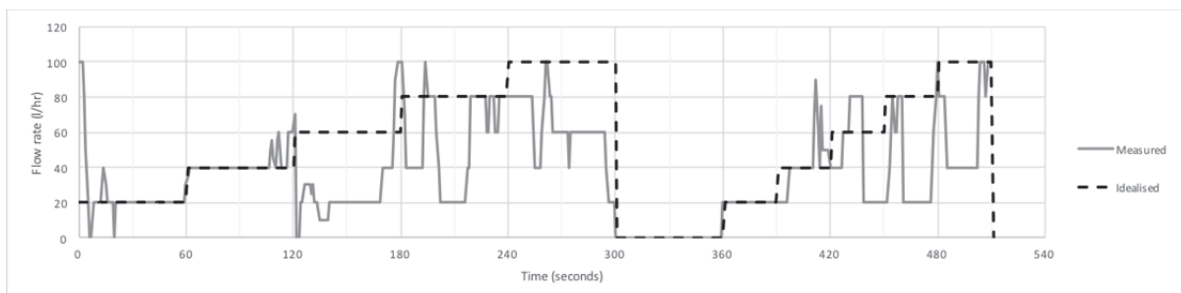
Figure C-13. **Measured flow rate against the planned interval flow rates at 20G.**
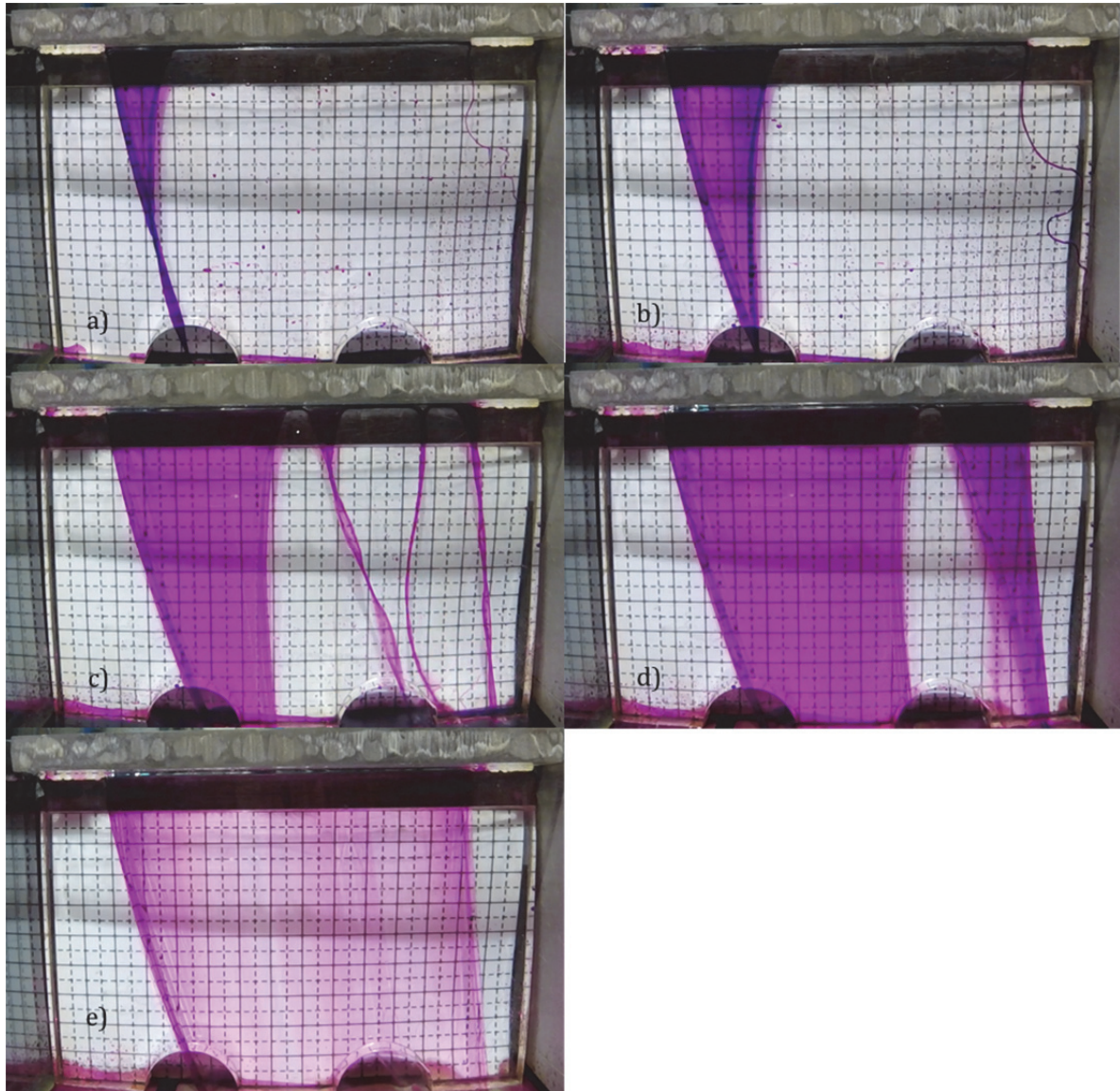

Figure C-14. Flow regime of the fluid out of the horizontal fracture onto the unconfined vertical face.

Drying

Air enters the fracture from the exit of the fracture (left hand side of Figure C-15a) during the drying interval of the test, whilst a no air enters at the inlet container (on the right hand side of figure). At the outlet vertical wall after the water is stopped, the sheet flow path disappears as well as all rivulets but one on the left hand side (Figure C-16a). Although the volume of water the rivulet transmits decrease, the rivulet never disappears, indicating that water is constantly flowing out of the horizontal fracture during the drying interval.
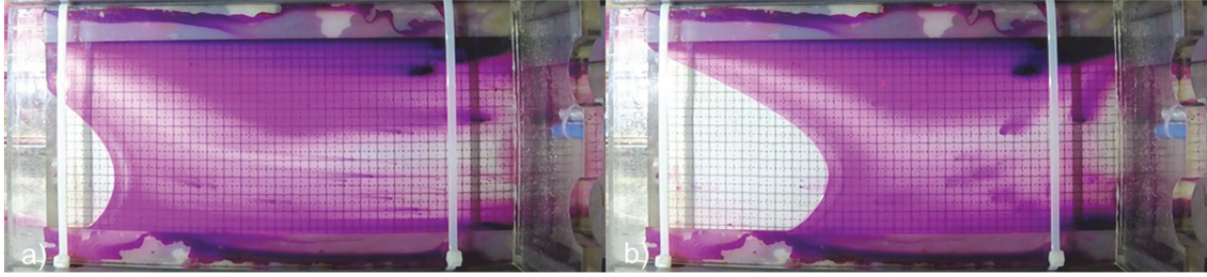
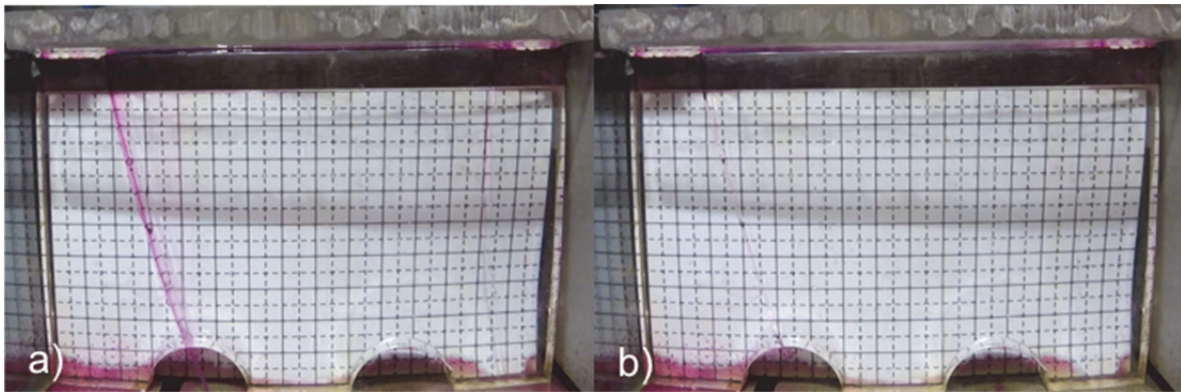**Figure C-15. Drying interval at: a) 10 sec; b) 40 sec; c) 2 mins; and d) 2 mins 55 sec.**

Figure C-16. Drying of the system out of the horizontal fracture onto the unconfined vertical face involves the drying out of rivulets.

Rewetting:

Upon rewetting at 20 l/hr, the capillary island which had invaded during the drying stage is quickly pushed out during the re-addition of water at 20 l/hr. There is a small capillary island which remains during the 20 l/hr interval, as seen at the edge of the exit of the horizontal fracture (Figure C-17a). During this interval water is exiting only at a discrete point along the single narrow sheet which flows out at the vertical wall. At higher influx intervals when cavitation occurs, this capillary island again invades from the exit of the horizontal fracture. However, momentarily when the correct flow rate is reached for that specific interval, the horizontal fracture is fully saturated.

At the unconfined vertical face, the same flow regime is observed as in the wetting phase. Initially, a narrow single sheet flow that remained during the drying stage transmits an increasingly larger volume of water (Figure C-18a) and widens along the vertical face during the subsequent intervals (Figure 3.25b, c, d, e, and f).
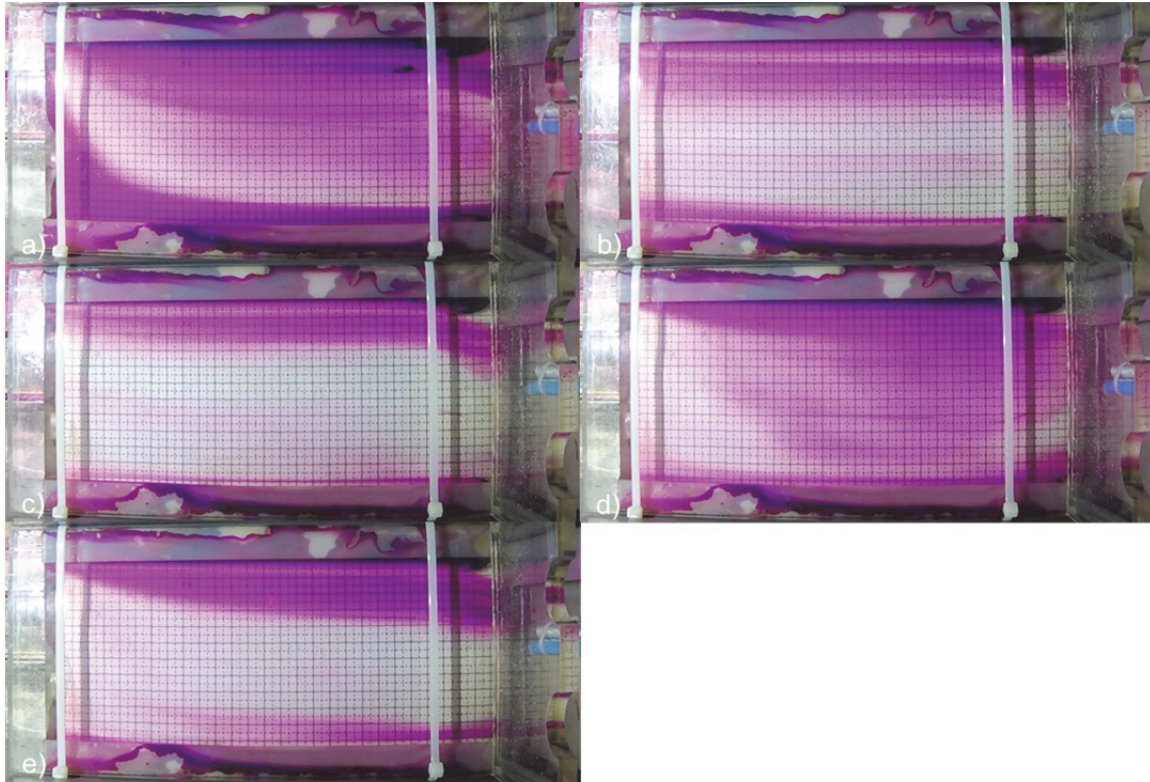
Figure C-17. Rewetting at: a) 20 l/hr interval, b) 40 l/hr interval, c) 60 l/hr interval, and d) 80 l/hr, and e) 100 l/hr interval.

C.2.2 Seepage flow

The wetting front is seen initially invading the horizontal fracture as a circular wetting front in Figure C-19a (1 second into the test – at model scale). This wetting front then makes contact with the spacer, which subsequently seems to act as a preferential flow path for the wetting front. Throughout the test, the horizontal fracture never saturates, and partial saturation of approximately 50% of the fracture occurs. Figure C-19f shows an overview of the horizontal fracture when the first droplet is noticed on the vertical wall (Figure C-20a). As observed in the continuous flow test, the outflow is only concentrated at a discrete point and exits as a single droplets down the vertical wall. The flow regime observed at this vertical wall seems to be in agreement with Su et al. (1999) for flow less than 8 mL/hr, consisting of individual droplets breaking off from the supply (horizontal fracture) when the weight of the water is greater than the surface tension.
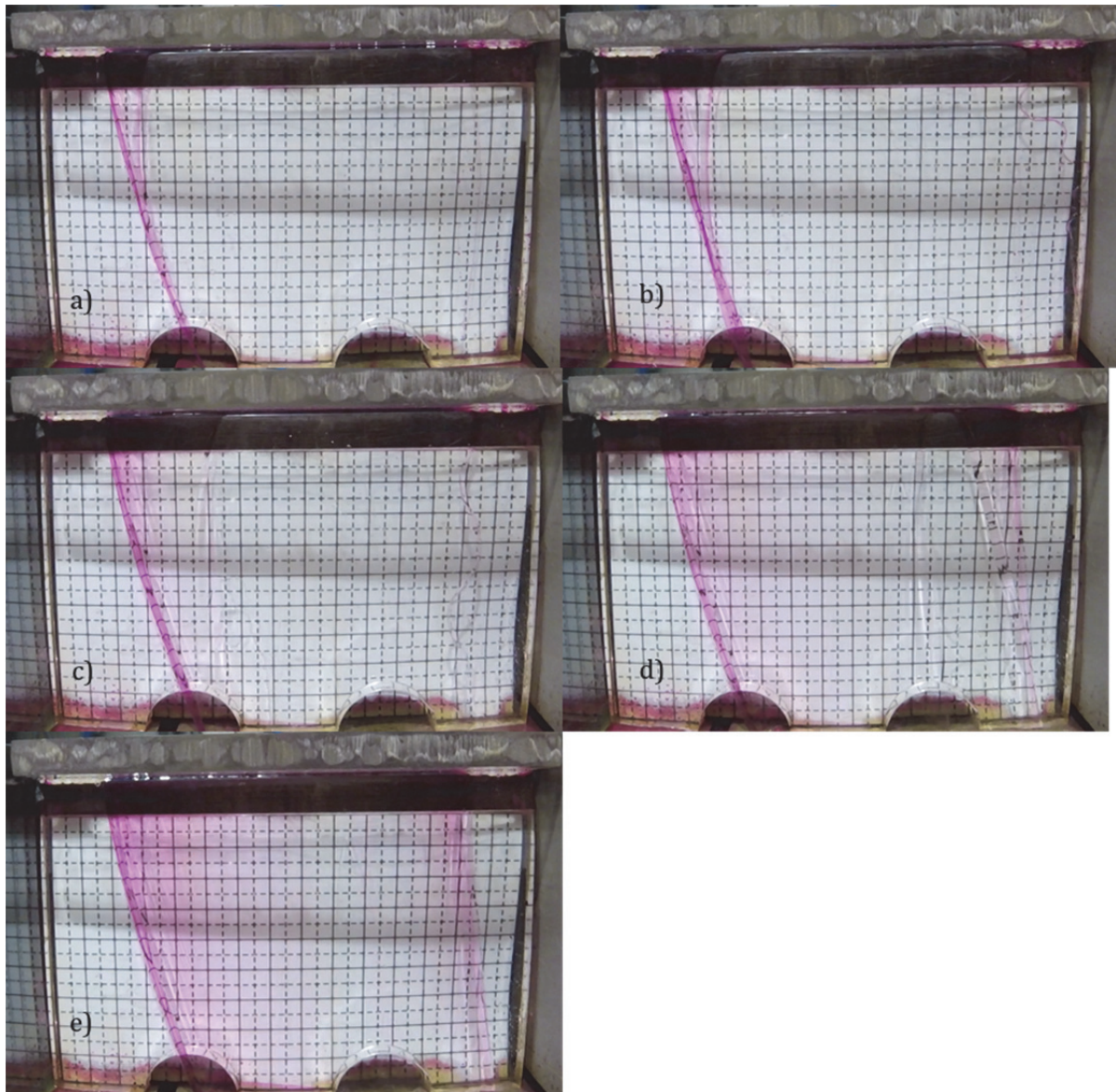
Figure C-18. Flow regime out of the horizontal fracture onto the unconfined vertical face for the rewetting intervals.
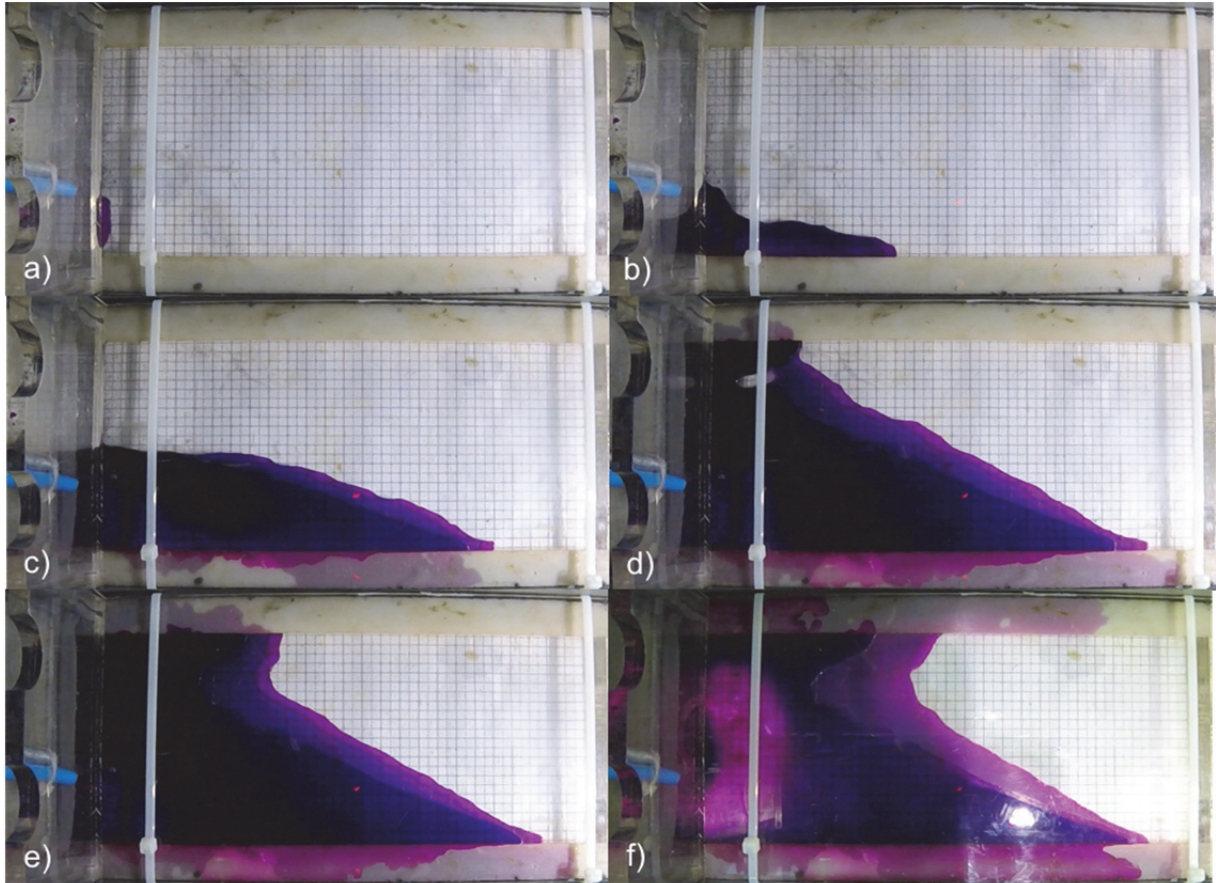
Figure C-19. Snapshots of the 20G intermittent flow test: a) 1 sec; b) 2 sec; c) 6 sec; d) 18 sec; e) 24 sec; f) 2 min 42 sec.
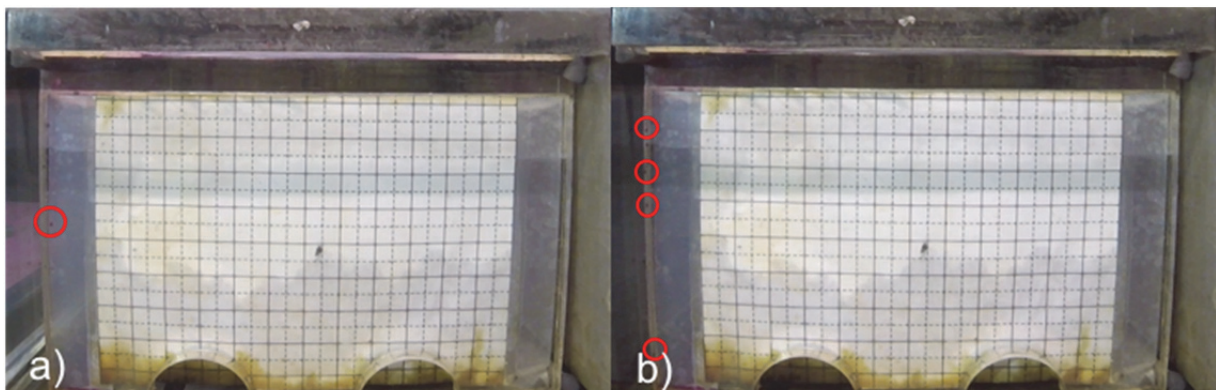

Figure C-20. Flow regime of the fluid out of the horizontal fracture onto the unconfined vertical wall for the intermittent test at 20G. Red circles indicate droplets.